University of Cape Town

Non-Destructive Testing Laboratory

DEPARTMENT OF MECHANICAL ENGINEERING

Comparative study of non-destructive testing methods for defect detection on aircraft

BY

Vincent Musonda

MSNVIN002

Bachelor of Engineering (Mechanical Engineering)

August 2007

A Dissertation submitted to the Faculty of Engineering in partial fulfillment of the Degree of Master of Science in Engineering

DECLARATION

1. I know that plagiarism is wrong. Plagiarism is to use another's work and pretend that it is one's own.

2. I have used the "American Society of Mechanical Engineers (ASME) Guidelines and Information to writing a technical paper" convention for citation and referencing. Each contribution to, and quotation in, this thesis from the work(s) of other people has been attributed, and has been cited and referenced.

3. This thesis is my own work.

4. I have not allowed, and will not allow, anyone to copy my work with the intention of passing it off as his or her own work.

Signature Signed by candidate

Vincent Musonda

August 2007

ACKNOWLEDGEMENTS

My sincere gratitude goes to my supervisor, Professor J Gryzagoridis for his guidance and support during my thesis. I am also grateful to Mr. D Findeis for being available whenever I needed his assistance.

I also wish to extend my thanks to the workshop staff and in particular Mr. Hubert Tomlison, Mr. Glen Newins, Mr. Peter Jacobs and many others for being available to help in various situations.

Special thanks also go to my sponsors, and in particular the Air force command for giving me the opportunity to pursue this program.

To my wife Barbara and our children to whom this thesis is dedicated, thank you for your patience during this hectic time. You persevered during my absence from home and for sure this was not easy for both of us.

DEDICATION

Dedicated to my wife Barbara

And our children, Tijuana, Chileshe, Glory

Louise and Vincent (JR)

Thanks for all your love and patience

SYNOPSIS

There is currently an increase in the usage of composite materials both in civilian and military aircraft because of their mechanical resistance, high toughness, reduced weight and immunity to corrosion. Any damage in the fibers of these composites requires an evaluation in order to ensure the integrity of aircraft structures. Composite materials are subject to various degrees of damage during their service life and therefore maintenance of these light-weight structures is a new challenge for non-destructive testing (NDT) which requires techniques that respond with a high probability of detection of defects on such high-specific strength materials.

In this thesis, Digital shearography and Infrared Thermography (IRT) techniques are employed to test aircraft composite materials. Background information on the techniques has been presented and the literature survey has confirmed the use of these techniques on aircraft structures. Much of the inspection work reviewed in the literature has focused on qualitative evaluation of the defects rather than quantitative. There is however, need to quantify the defects if the threshold rejection criterion of whether the component inspected is fit for service has to be established. In this thesis, therefore, quantitative analysis of the defects on helicopter main rotor blades and Unmanned Aerospace Vehicle (UAV) composite material is presented. The fringe patterns exhibited by Digital shearography were used to quantify the defects by relating the number of fringes created to the depth of the defect or flaw. Qualitative evaluation of defects with IRT was achieved through a hot spot temperature indication above the flaw on the surface of the material. In this part of the present work, however, the shearographic technique proved to be more sensitive than the IRT technique.

It should be mentioned that there is "no set standard procedure" tailored for testing of composites. Each composite material tested is more likely to respond differently to defect detection and this depends generally on the component geometry and a suitable selection of the loading system to suit a particular test. The experimental work that has been covered in this thesis can however, be used as a basis for designing a testing procedure for a particular composite material component or structure.

NOTATION

α	Thermal diffusivity
K	Thermal conductivity
ρ	Density
C	Specific heat capacity
T	Temperature
t	Time (seconds)
δ_x	Magnitude of the shear
θ_x	Function of object beam
P_1 and P_2	Source points of light waves
$\Delta\phi$	Phase difference between the light waves
$\frac{\partial d}{\partial x}$	Rate of surface displacement
$\frac{\partial w}{\partial x}$	Deformation in x-axis
$\frac{\partial w}{\partial y}$	Deformation in y-axis
λ	Wavelength for laser light
n	Number of fringes
$I_i(x,y)$	Measured intensity of the interferogram
$I_B(x,y)$	Background intensity
$I_m(x,y)$	Modulation intensity
$\phi(x,y)$	Phase difference between the object and reference beam

$\phi_b(x, y)$	Phase before deformation
$\phi_a(x, y)$	Phase after deformation
$\Delta\varphi$ (x, y)	Phase difference between the phases of the interfering speckle patterns
I_1 (x, y)	Intensity distribution before loading
I_2 (x, y)	Intensity distribution after loading

ACRONYM

CCD	Charge -Coupled Devices
PT	Pulsed Thermography
CFRP	Carbon Fiber Reinforced Plastic
IRT	Infrared Thermography
NDE	Non destructive Evaluation
NDT	Non destructive testing
DSSI	Digital Shearography Speckle Interferometry
PZT	Piezoelectric Transducer
PC	Personal Computer.
UAV	Unmanned Aerospace Vehicle
IFWIT	Instrumented falling weight impact testing
MIA	Mechanical Impedance Analysis
BVID	Barely Visible Impact Damage

TABLE OF CONTENTS

LIST OF FIGURES

LIST OF TABLES

CHAPTER 1

1. Introduction

1.1 Overview of Nondestructive testing techniques

"Nondestructive testing (NDT) is a very broad, interdisciplinary field that plays a critical role in assuring that structural components and systems perform their function in a reliable and cost effective fashion." [1] It involves all aspects of uniformity, quality and serviceability of materials and structures. Essentially, NDT refers to all the methods which allow testing or inspection of a system without impairing its future usefulness even without taking it out of service. "NDT engineers and technicians define and apply tests that locate and describe material conditions and flaws that might otherwise cause airplanes to crash, reactors to fail, trains to derail, pipelines to burst, and a range of less visible, but equally troubling events" [1]

In general, the use of NDT will fall into one of the following categories: determination of material properties; detection, characterization, location and sizing of discontinuities or defects; determining quality of manufacture or fabrication of a component or structure; and checking for deterioration after a period of service for a component or structure [2]. "Because it permits inspection without interfering with a product's final use, NDT provides a tremendous balance between quality control and cost- effectiveness" [1]. Technology that is used in NDT in some instances is similar to those used in the medical industry; yet, obviously on inanimate objects. Some of the benefits derived from NDT are increased productivity, improved serviceability and safety

1.2 Background

Non-destructive testing and evaluation (NDT&E) techniques are widely used in the manufacturing, power, petrochemical and Aircraft industries, both as tool to certify the

integrity of manufactured components and for routine maintenance inspections. For example in aircraft maintenance programs, it is necessary to check the mechanical damage and evaluate the scope of the repair work. However, in scheduled maintenance it is not easy to find the defects quickly, as the maintenance of aircraft must be completed within scheduled time normally aimed at returning the aircraft very quickly back to operation.

Khan, A.U [3] reveals that, during aircraft maintenance, NDT is the most economical way of performing inspection and perhaps the only way of discovering defects. It can simply be said that NDT can detect cracks or any other abnormalities in the airframe structure and engine components which apparently are not visible to the naked eye. Khan further highlights the fact that "Structures and assemblies of aircraft are made from various materials, such as aluminum alloy, steel, titanium and composite materials. To dismantle the aircraft in pieces and then examine each component would take a long time, so the NDT method and equipment selection must be fast and effective".

There are many NDT methods available and in order to maintain the aircraft defects free and ensure a high degree of reliability, as part of the inspection program, many of the following methods may be applied: liquid penetrant, magnetic particle, eddy current, ultrasonic, radiography, infrared thermography, visual and optical interference inspection techniques only to mention but a few. This work focuses on the capabilities of selected inspection techniques in the detection of flaws or defects on some aircraft components.
There are different materials used on the aircraft such as metals, composites adhesively bonded and including welded regions, and hence no single NDT is capable of inspecting the aircraft as a whole. Many other complementary NDT techniques are to be used in a particular routine inspection [4]. The task therefore of this work is to identify and evaluate new and advanced NDT techniques whose capabilities are to meet the most recent range of inspection problem areas which has arisen as a result of the increasing usage of relatively newly developed composite material. For instance, "the Airbus A380 has led the way with about 25 percent of aircraft using composite material, and the Boeing 787 will be having up to 50 percent composites, including the entire fuselage"

[5]. From his study, Nyman, T [6] observed that: "a modern combat aircraft today contains high percentages of advanced composite material in flight critical primary structures such as those found in B-2 Stealth bomber, the F-22 advanced tactical fighter, the F-117A Stealth fighter, and the V-22 tilt-rotor." In addition the author noted that, the new Swedish fighter JAS39 Gripen, for example, uses about 20% by weight, carbon fiber/epoxy composite laminates in the primary structure and the weight distribution is illustrated in Figure 1.1 below. Maintenance of these light-weight structures therefore is a new challenge for NDT which requires methods that respond with a high probability of detection (POD) to such high-specific strength materials and their defects.

Figure 1.1: The extent of composite materials in JAS39 Gripen [6]

Some conventional NDT methods such as x-ray inspection or ultrasound which were designed for the needs of metal structures cannot meet the challenges which composite materials can offer. Some defects are due to errors inherent in the manufacturing process; others are due to in-use damage. Therefore one needs robust methods which respond and

provide consistent results in an industrial environment within short time. This suggests that contacting point-by-point methods are too time-consuming for most large-scale inspections.

In this work, Infrared Thermography and Digital Shearography techniques were used in the testing of some aircraft composite component structures and an overview of these techniques are presented in sections, 1.3 and 1.4, respectively. Chapter 2 deals with background theories of the techniques in detail as well as previous detection work done using the same techniques.

1.3 Infrared Thermography

Infrared thermography (IRT) is a nondestructive evaluation (NDE) method used for the localization and characterization of thermally resistive defects. The method is based on the principle that heat flow in a material is altered by the presence of some types of anomalies [3]. These changes in heat flow cause localized temperature differences or thermal patterns in the material. The heating of the material can be done with quartz lamps or hot air from a dryer. Active heating (with lamps or forced air) of the material under investigation can also be used to expose severe subsurface defects and the surface temperature can be viewed accordingly. For many applications however, "flash lamps provide the fastest most compact way to heat the surface uniformly, although alternative sources may be used for particular applications." [7]

IRT is a non contact, non-intrusive optical technique which makes it possible for us to see thermal energy. The technique uses an Infrared camera which transforms the energy radiated from objects in the infrared band of the electromagnetic spectrum into an electronic video signal and eventually into a detectable image; and each energy level may be characterized by a colour, or a grey level [8]. In other words, images on the video or film record the temperature variations of the surface ranging from white for warm regions to black for cooler areas with black and white cameras. Color cameras produce the image in reds and blues. The resulting images help determine whether differences in

temperatures are present. The terms 'infrared' and 'thermal' are used interchangeably in some context. Thermal refers to the physical phenomenon of heat, and this involves the movement of molecules. Infrared (below the colour red) designate radiation between the visible and microwave regions of the electromagnetic spectrum.

IRT basically includes a camera, equipped with a series of changeable optics, and a computer. Figure 1.2[2], shows a typical setup of an IRT system.

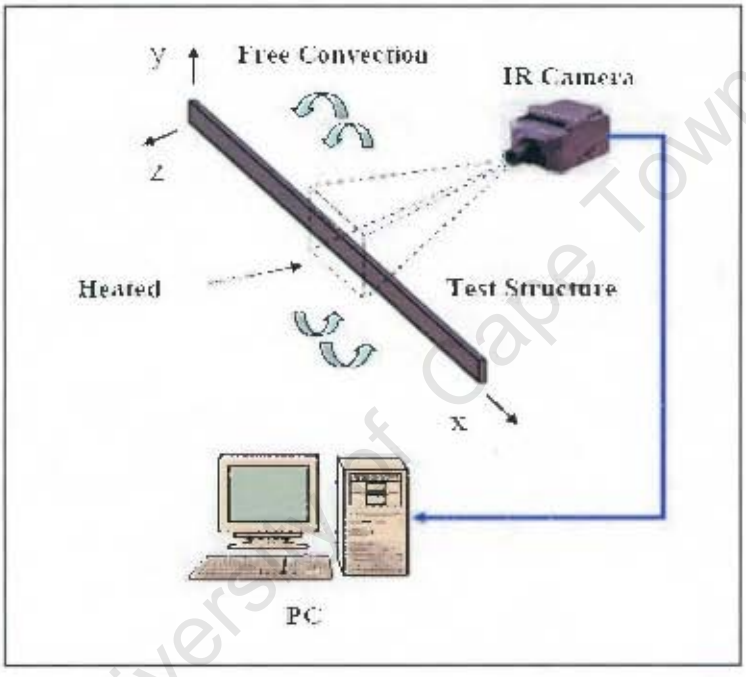

Figure 1.2: Infrared thermography testing setup

The core of the camera is the infrared detector, which absorbs the infrared energy emitted by the object (whose surface temperature is to be measured) and converts it into electrical voltage or current.

Wong, B.S., *et al* [9] testified that IRT is one of the many other NDT techniques which can be used for the detection of flaws in aircraft materials such as composites. The authors further pointed out that IRT can be potentially useful in the aerospace industry, because it is fast, real time and is able to inspect a relatively large area in one inspection procedure.

Gryzagoridis and Findeis [10] have affirmed that , IRT systems have been used for the detection of impact damage in aerospace structures made from honeycomb and composites and that these systems, operate in real time producing pictures known as thermograms through optics that are sensitive to infrared radiation. Khan, A.U [3] equally observed that "infrared thermography has been chosen for quick operational use and reliable in detecting 'liquid contamination' in the composite sandwich as compared to x-ray method". The method is also capable of detecting thermal overheating in electrical and hydraulic systems.

There are specific areas which can be inspected on aircraft structures using IRT and these include: composite laminate parts for delamination, debonding or damage due to foreign objects, composite sandwich parts for debonding and liquid contamination, metallic bonded parts-for debonding of corrosion. Proof of the location of problems can be visualized in the detailed report through photos. Figure 1.3, shows two thermal wave images of a composite spoiler structure of an aircraft, whose Nomex honeycomb had extensive fluid intrusion [11]. The fluid shows as dark regions, because of its heat-sinking influence at the skin. The image in Figure1.3 (a) was taken from above and shows wicking of the fluid up to the skin. When the spoiler was turned over and imaged from below, the fluid collected at the skin, and this is represented in Figure 1.3 (b)

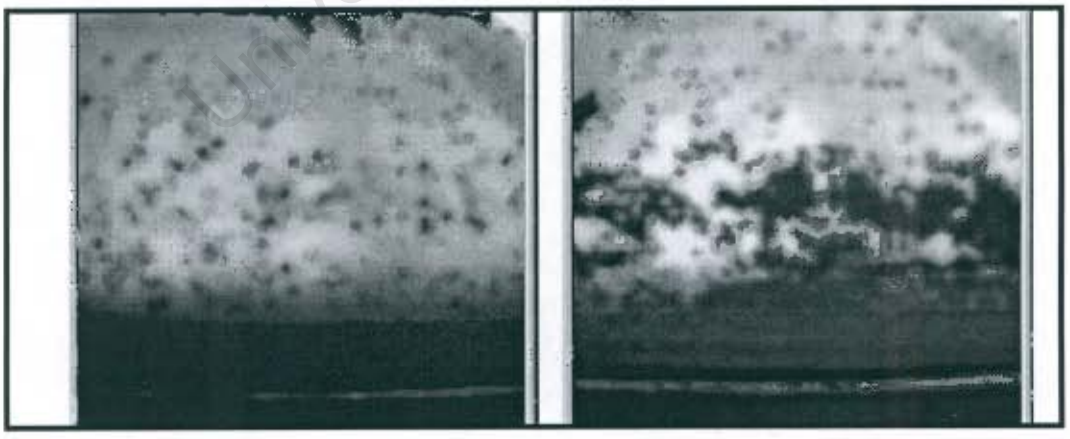

(a) (b)

Figure 1.3: Thermal wave images with extensive fluid intrusion

Fluid/water ingress can also be detected when it takes place in aluminum honeycomb composite structure, such as is used in the construction of the F-15 aircraft rudder. Figure 1.4, shows this type of defect.

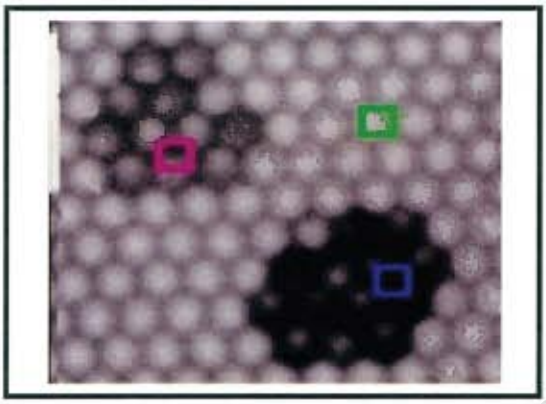

Figure 1.4: Fluid ingress in F-15 rudder detected by IRT [11]

In Figure 1.4, the upper left region (dark grey) contains hydraulic fluid in the cell, whereas the lower right (black) contains water. The three squares were placed on the image by the thermal wave imaging software, and indicate regions for which temperature-time curves can be plotted.

1.4 Digital Shearography

Digital Shearography is an emerging technique very well suited for the inspection of components in the aerospace industry. It is a laser based speckle interferometric optical technique, originally developed for strain measurement. The technique is highly sensitive to surface displacement gradients, resulting from subsurface flaws associated with internal de-bonds, delaminations and cracks [12]. It uses a special shearing device and hence it measures a gradient of displacement, and not the displacement itself

Shearography detects both surface and hidden defects by sensing abnormal strains induced by areas of weakness in the structure without physically contacting the test surface. It allows full-field measurement of strains for rapid inspection of composites, bonded structures and other advanced materials [13]. Strains are functions of

displacement gradients; thus, shearography yields strain information directly. Because defects in objects usually induce strain concentration, it is easier to reveal defects with strain anomalies than with displacement anomalies. Moreover, a rigid-body motion does not produce strain; thus shearography is insensitive to such motion. This is an important advantage of shearography, which signify the usefulness of shearography in typical industry operation.

Although Digital Shearography has several advantages, its successful application for NDT in industries still depends on depth and type of defects, the type of materials, the shearing amount and direction, the manner of load and laser illumination, and so on.

1.4.1 Instrumentation

Digital Shearography consists of three parts: a digital camera, a shearing unit and a laser device for illumination. The object to be evaluated is illuminated by the laser, and imaged by a video Charge-Coupled-Device (CCD) camera consisting of imaging shearing device. The shearing device splits one object point into two in the image plane. Consequently, a pair of laterally-sheared image is received by the image sensor, and thus the technique is named as shearogarphy [14]. The shearing unit is a key component of shearography. Basically, any device which is able to bring light scattered from two points on object surface through the lens of digital camera at one point of the image plane can be used as a shearing device.

Different researchers have used different shearing devices such as optical glass wedge, a bi-angle prism, a doubly-refractive prism, a modified Michelson Interferometer and so on[12,14]. In digital shearography, the phase-shifting technique (discussed later) is applied. Hence, one important issue to select a shearing device is whether a phase-shifting can easily be introduced in the shearing device. Among the shearing devices which have been used, the modified Michelson Interferometer is the best method which can easily change the shearing amount and the direction by changing the tilting angle and

direction from one of two mirrors and also can easily introduce a phase-shift by moving the other mirror. A simplified setup of digital shearography is shown in Figure 1.5[15].

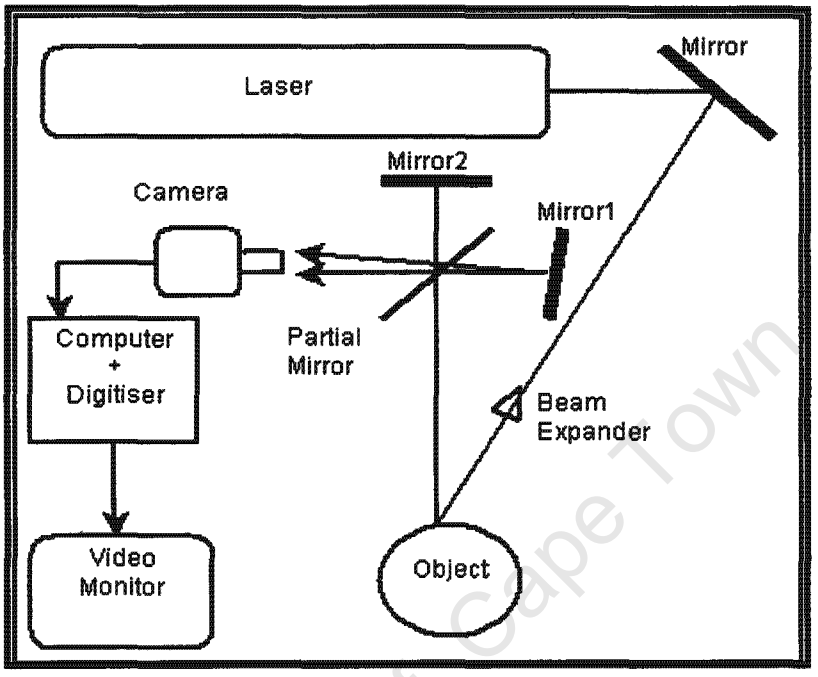

Figure 1.5: Simplified setup of digital shearography [15]

Theoretically, the 90, 180, and 270-degree phase shifts can be obtained by moving the mirror through small displacements $\lambda/8$, $\lambda/4$, and $3\lambda/8$, respectively. However, a control for the accurate movements is difficult practically. Therefore a calibration method of phase shift is required.

1.4.2 Methods of stressing the object

The identification of flaws in materials is critical and unless a proper loading system is used, the whole inspection process is bound to be unsatisfactory. Therefore it is important to choose a loading method which will facilitate the manifestation of flaws as localized surface deformations which would otherwise not be present in the structure in the absence of flaws. Sridhar krishnaswamy [16] describes the three most common methods of loading the test structure as: acoustic loading where the structure is made to vibrate at

various frequencies; pressure loading where the structure is deformed by application of external pressure (or evacuation); and thermal loading where the structure is heated. The author further describes these methods as follows:

Acoustic loading

This loading is useful for the detection of subsurface disbonds and delaminations in the structure. The excitation of the structure is achieved by using electromechanical appliances such as piezoelectric transducers or indeed speakers. Single frequency, swept frequency, or broadband excitation can be used to stimulate resonances in the test structure. For modal analysis, the resonant response itself is of inherent interest. For the detection of flaws in adhesively-bonded structures which have debonded regions, these regions can be expected to reveal different resonant modes than the adjacent well-bonded structure.

With vibration excitation, an area which is perfectly bonded for example appears as dark, and if there is any departure from "perfect darkness" then it means there is a weak bond which in this case will manifest itself as a bright region (unbonded area). Figure 1.6 and Figure 1.7, are typical examples of fringe patterns of debonds at 3, 6, 9 and 12 mm respectively [13]. It should be noted that the one closest to the surface has the highest fringe density and vice versa.

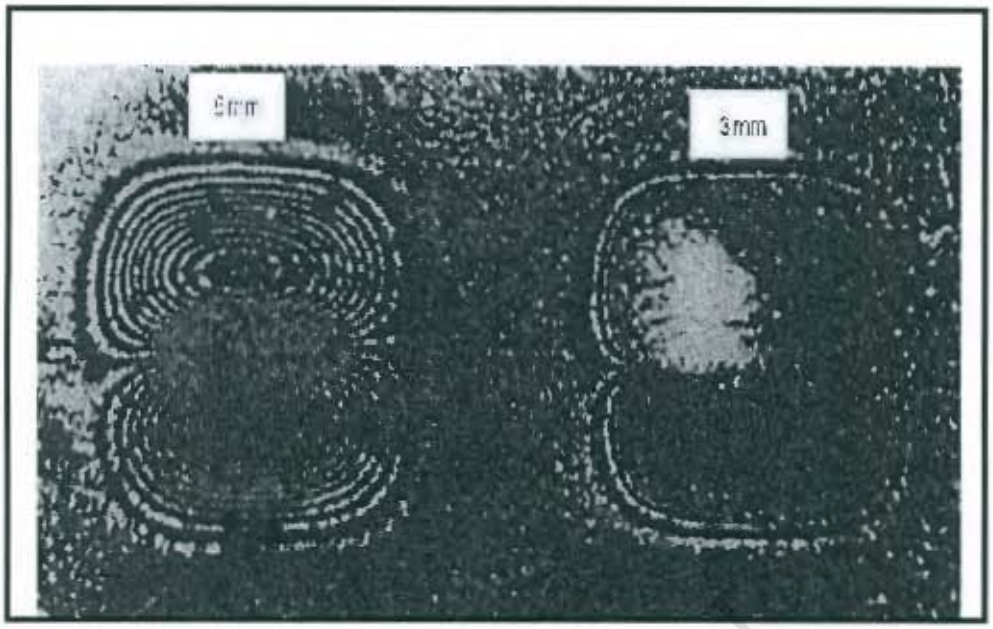

Figure 1.6: Fringe patterns of debonds for 3 mm and 6 mm [13]

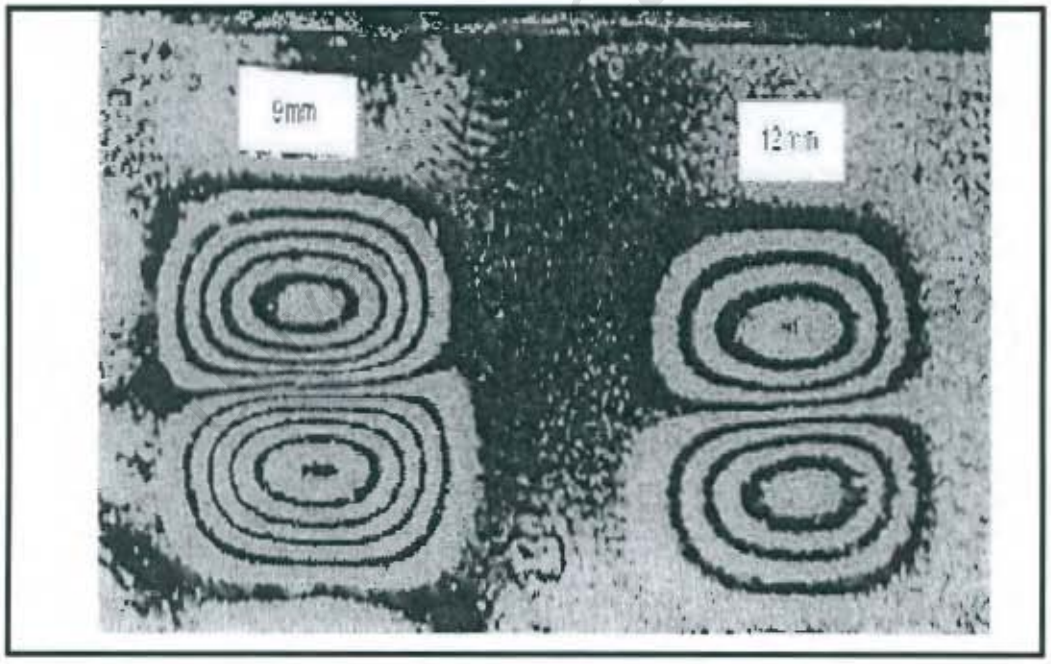

Figure 1.7: Fringe patterns of debonds at different depths (9 and 12mm) [13]

Pressure loading

Pressure loading is in essence a slow mechanical loading method that has proven useful in the testing of pressure vessels, tyres, and honeycomb structures. The loading system has also been useful in the testing of composite laminates especially for debonds that are deep inside the structure. Pressure loading operates by acquiring one image of the test object when it is under normal operating pressure, and then to evacuate or pressurize the structure in order to induce a mechanical deformation of the test object. This mode of loading is suitable for objects that are naturally pressurizable such as tyres and pressure vessels. However, structures which are not usually subject to pressure loading during their operation cycle need to be enclosed in a pressure chamber either wholly or in part. Delaminations in composite material such as a honeycomb panel of a helicopter can be detected by shearography and since the skin of the panel is graphite epoxy, the means of stressing is partial vacuum.

Thermal loading

Thermal loading is a simple non-contact method that is useful particularly for materials that have low thermal diffusivity, such as polymer based composites. The structure under investigation is heated up and the resulting deformation in the structure is observed during the heating up and cooling down process. Usually, flash lamps or lasers are used to heat the structure. The technique is useful for the detection of delaminations. Again a continuous sequence of deformed states is available for optical comparison when an object is subject to thermal stressing.

1.5 Research Objectives

- To assess suitability of each inspection technique when testing or inspecting various aircraft components.

- To assess if any of these techniques are vulnerable to environmental conditions.

- To assess the quality of defects' detection.

1.6 Procedure used to gather Information

The information on which this thesis is based was gathered by means of:

- Books
- Articles
- Journals
- Internet searches
- Meetings with my supervisor

1.7 Road map

This thesis is organized into six main chapters and one appendix. Chapter 1 began with an introduction of NDT in general, and an overview of NDT techniques to be used in the testing of some aircraft composite component structures.

Chapter two establishes the literature survey of the inspection techniques and the defect detection work done by other researchers. Infrared thermography lays the emphasis on reliable detection and interpretation of thermal signatures of the defects. Digital Shearography is discussed with regard to displacement gradient measurement and fringe pattern formation and interpretation.

Chapter three is a link between chapter two and chapter four. Impact behavior of composite materials in aircraft is discussed in this chapter.
Chapter four explains the experimental procedure for the inspection of defects.

Chapter five lays out the results of the experimental investigation, and finally the thesis is concluded.

CHAPTER 2

2. Literature Review

This section focuses on the application of IRT and Digital Shearographic techniques in relation to composite materials in some aircraft component structures. Pulse Thermography (PT) will be discussed as one of the IRT systems used on aircraft composites. Other research work done by the users of the same techniques is also evaluated.

2.1 Pulse Thermography

PT is a thermal stimulation technique where the surface under investigation is pulse heated using one or more pulse heating sources such as xenon flash tubes, scanning lasers, or hot air jet. The duration of heating depends on the material being investigated. Composites are low conductive materials, and hence require only a few seconds of heating. Metals on the other hand are high conductive materials and hence require a few milliseconds of heating. The resulting thermal transient at the surface is then observed using a thermal camera [17].

2.1.1 Analysis with PT

Two modes of heat transmission can be used to analyze the temperature patterns in PT, and these are: transmission and reflection modes respectively. In the transmission mode, the infrared camera views the rear face of object i.e. opposite to the heating or cooling source. In real applications, however, the opposite side is often not accessible and so the reflection mode must be applied with both the infrared camera and stimulating source on the same side [8].

In his study, Clemente, C.I[18] observed that, "reflection is used when inspecting defects closer to the heated surface, whilst transmission is preferred for detecting defects closer to the non-heated surface (i.e. deeper defects)". The author further noted that generally, resolution is higher in reflection and it was easier to set up given that both sides of the specimen do not need to be available. Other observations made are that, as much as deeper defects could be detected in transmission, depth information is lost because thermal waves will travel the same distance regardless of the reduction in strength due to the presence of a defect or not, and this implied that depth quantification is not possible in transmission[18,19].

Figure 2.1 shows a typical experimental configuration in active thermography in reflection and transmission.

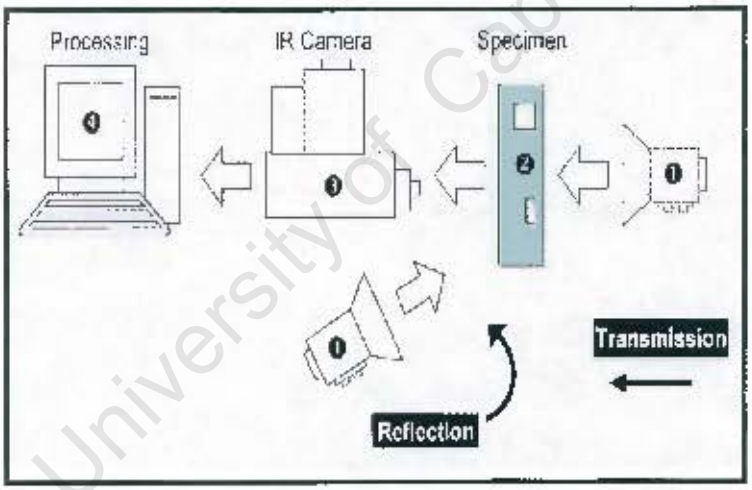

Figure 2.1: Configuration in active thermography in reflection and transmission (1) Heat source, (2) specimen, (3) IR camera, and (4) PC for data display, recording and processing [18]

In PT, the qualitative thermal images can be translated into quantitative results by analyzing the time and spatial dependency of the surface temperature. Thus, information concerning the size of a detected defect can be achieved. However, PT is an inherently near surface technique whose effectiveness decreases with defect depth and it is also dependent on the thermal properties of the investigated material [20].

2.1.2 Some applications of PT

Common applications of active PT scheme are in quantitative subsurface defect assessment (cracks, delaminations, impact damages, disbondings, moisture), thermophysical property evaluation; in all kinds of industries (aerospace, metal, buildings etc). In aerospace industry, PT is a widely used approach for investigating aircraft materials and structures [17]. It is a rapid, large area technique with the additional advantages of being single-sided and non-contact. These attributes make this technique particularly suitable for surveying impact damage either on carbon fiber-reinforced plastics (CFRP) single panels or on sandwich structures.

Takeda, S., [21] conducted durability tests of a composite wing structure of an aircraft in order to verify its health monitoring capabilities for long-term use. The durability tests included drop-weight impact tests and two periodic fatigue tests based on the design service life of the aircraft. Barely Visible Impact Damage(BVID) was also introduced in the wing structure .The damage evolutions in the test panel were evaluated by using Pulsed Thermography, Acoustic Emission (AE), and ultrasonic C-scan NDT techniques. A commercial PT system (Echo Therm, Thermal imaging) was used every 1/10 of the design life during the fatigue tests for the evaluation of the increased impact damaged areas, and high-power xenon flash lamps of 4800J were used in this case. The authors concluded that all the techniques were able to detect the fatigue and BVID. Pulsed Thermography, however, only took 20 seconds from the flash of the lamps to the end of the data collection period. Figure 2.2, shows the photographs of the BVID after the fatigue tests.

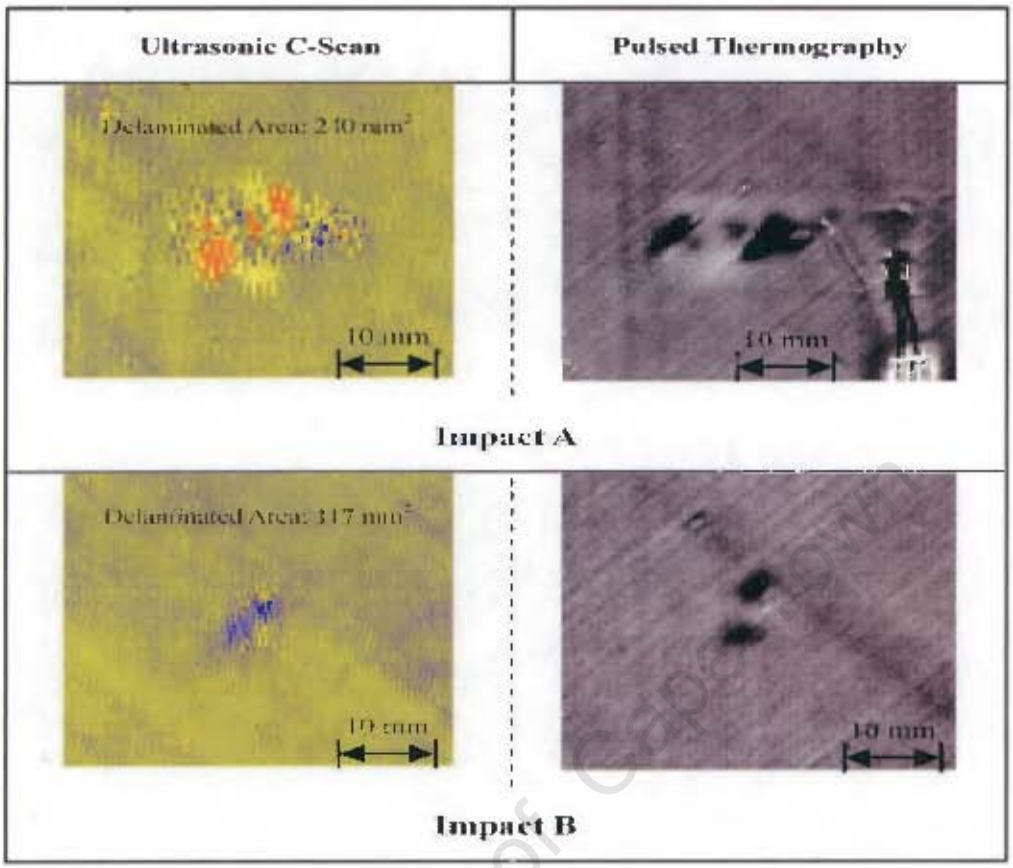

Figure 2.2: Photography of BVID after fatigue tests [21]

Avdelidis and Almond [22] did a study to establish the ability of Pulsed Thermography to locate anchoring points beneath the outer skin of aircraft structures, to facilitate automated drilling and fixing during the assembly operation. Typical test structures, comprising of 1.6 mm thick aluminium skins and both 2 mm and 4 mm thick CFRP composite skins over both aluminium and composite struts respectively were used in the experiment. The ability of the technique to detect subsurface fixing and to offer information about its location was investigated. The authors concluded that the technique demonstrated to work well for CFRP and aluminium alloy skins, and that, the results indicated that PT can be used effectively for the detection of subsurface features located beneath composite and aluminium alloy skins. It was further observed that, the technique showed great potential as far as locating the centre of a fixing accurately.

Xiaoyan, Favro and Thomas [23] presented examples of disbonds, delaminations and corrosion inspections in metal aircraft and composite structures respectively, using thermal (IR) imaging technique. The metal structure which was inspected for the presence of disbonds, in a B 747 aircraft was an internal doubler. Composite structures inspections included sound-deadening structures used in engine cowlings for commercial aircrafts and composite spoiler structure, whose core is aluminum honeycomb. Figure 2.3, shows a photograph of the pulse echo thermal wave imaging system in operation to inspect a B747 aircraft for the presence of disbonded internal doubler structure. The inspection can be confirmed by the authors operating the system from an extendable lift platform, from which they were using the hand- held thermal imager.

Figure 2.3: Inspection of the B747 internal doubler for the presence of disbonds [23]

In addition, the authors also presented inspected composite structures on C-130, C-141, and F-15 aircrafts by United States Air Force (USAF) personnel. Figure 2.4, shows an image of an F-15 test specimen, depicting a region of machined core.

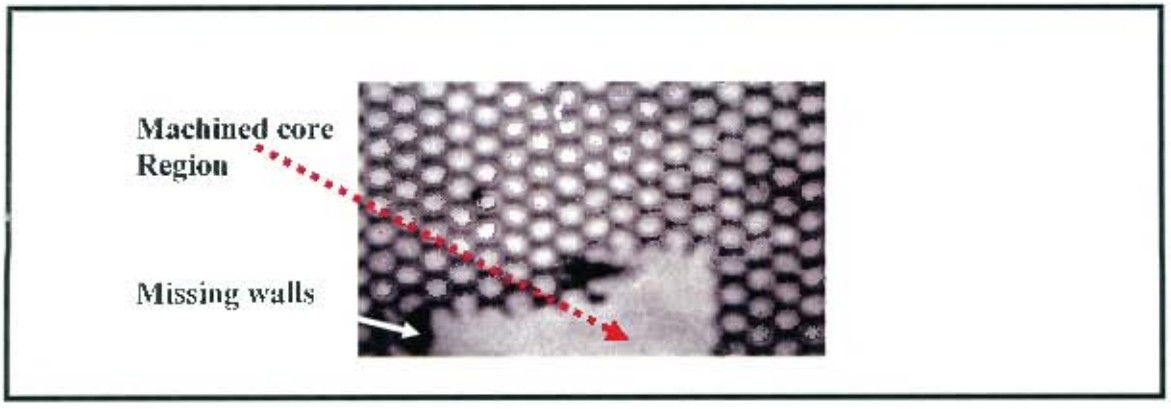

Figure 2.4: Thermal image of an F-15 test specimen

The technique showed the capability to image aluminium honeycomb structures beneath the five plies of boron-fiber-reinforced composite skin in a region. Figure 2.4 also shows a machined core defect (simulated skin-to-core disbond), which is obvious from the missing walls of the aluminum honeycomb (dark) in that region of the image.

Capriotti, *et al* [24] did a comparative evaluation of different NDT techniques for the investigation of defects caused by low-energy impacts on specimens made of CFRP. The same techniques were also used on the inspection of structures of military aircraft such as the main landing gear (MLG) secondary door, in order to evaluate the capability to discover damages that could happen during the in-service life of the aircraft. The NDT methods which were used, include, Ultrasonic, X-Ray Radiography, Visual Inspection, IR Thermography and Mechanical Impedance Analysis (MIA). During the IRT testing, a surface of about 400 cm^2 of the main landing gear door (MLG) was heated by flush tubes for 10 ms duration and the cooling process was observed for 65 seconds by an infrared camera. The authors concluded that, all the methodologies used were able to detect the damages inside the part. The PT results, showed the capability of finding the defects with a qualitative indication about their depths. The same indications were found by using Ultrasonic method as well. It was observed, however, that, the MIA, if applied only on a single surface, was not able to find all the defects inside the part.

2.1.3 Heat diffusion model in a material

In order to understand the heat distribution through a material with a subsurface defect and the resultant temperature evolution, a Fourier diffusion equation is presented as:

$$\nabla^2 T - \frac{1}{\alpha}\frac{\partial T}{\partial t} = 0 \qquad \text{Eq (2.1)}$$

Where α is the thermal diffusivity (m^2s^{-1}), which is equal to $k/\rho C$ with k the thermal conductivity ($Wm^{-1}K^{-1}$), ρ the density (kgm^{-3}) and C the specific heat capacity ($Jkg^{-1}K^{-1}$) of the material, T is the temperature and t is the time. For uniform heating and in the case of a homogeneous material, the surface temperature distribution would be uniform. The distribution of heat, however, is not uniform in the presence of a defect and this results in a localized temperature difference [8], [25].

2.1.4 Defect detection

The sensitivity of thermographic inspection has its limitations when it comes to type and size of a defect to be inspected. Because different materials possess different values of thermal conductivity, regions such as disbonds or air inclusions tend to build up heat, thus indicating the location and size of the flaw. The thermal pattern within the composite material for example is altered once a disbond, delamination or other anomaly has been introduced in it [26].

Figure 2.5 shows a comparison between thermal patterns in steel and composite materials. If equal magnitude and duration of the heat imposed onto both samples were assumed, the composite sample will conduct heat at a slower rate, i.e. thermal energy does not spread as rapidly throughout the part as it would in the case of a steel sample of comparable dimensions. Also, as may be seen, heat propagation will occur more rapidly along the fiber direction.

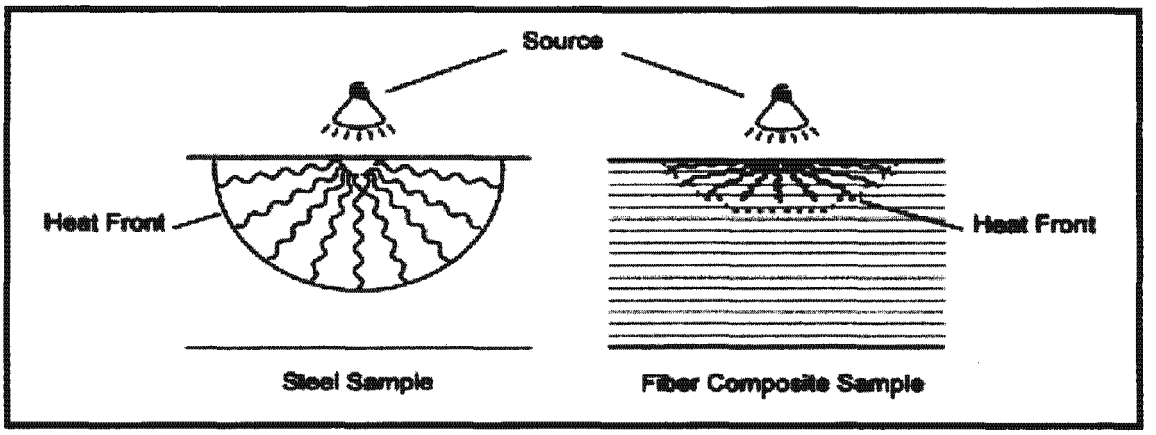

Figure 2.5: Thermal conduction in (a) steel and (b) composite samples [26]

The significantly higher conductivity of carbon facilitates quick and more heat propagation compared to the transverse direction. Non uniform heating is also an important parameter worth considering. This is discussed briefly in the next section.

2.1.5 Non-uniform surface heating

It is natural to experience variations in the surface temperatures during the heating up of a material particularly for a non perfect flat surface in active thermography. However, there are still several factors to take into consideration during the inspection of any material, and a flat surface material is no exception. Therefore issues such as the position of the heating source, serviceability of the equipment in use, external heating or cooling sources, and irregularities in optical properties of the surface being inspected, will stimulate non-uniformities[18]. Primarily, defect detection principle is based on temperature differences; it therefore implies that the presence of non-uniform heating may create uncertainty in the results especially for defect quantification. The temperature should thus be the same at the first instance for an evenly heated object.

2.1.6 Summary of IRT techniques

IRT is an NDT&E technique used for localizing and characterizing defects that are thermally resistive. It is based on the principle that heat flow in a material is changed by the existence of some types of abnormalities [3]. For many applications flash lamps are used to heat the surface of the material uniformly and these have been considered to provide the fastest most compact way of heating, although other sources may be used for particular applications [7].

IRT uses an Infrared camera which converts the energy radiated from objects in the infrared band of the electromagnetic spectrum into an electronic video signal and finally into a detectable image [8]. Color cameras produce the images in reds and blues. The resulting images assists in establishing whether a disparity in temperature exists.

Non-uniformities of heating, emissivity variations, and surface geometry can have a large impact on thermal data.

The key, to using an IRT system is to combine skilled operation of the imaging system with a good understanding of how Infrared radiation interacts with the object(s) being imaged. In view of this, the principles of Infrared radiation are vital to the understanding of the subject.

2.2 Principles of Digital Shearography

2.2.1 Background theory

Digital Shearography, also referred to as Digital Speckle pattern Shearing Interferometry (DSSI), is described as a robust measuring technique due to its simple optical setup and relative insensitivity against ambient noise [27]. It is an emerging technique very well suited for the inspection of components in many applications, including the aerospace industry [12, 13]. It is a laser based speckle interferometric optical technique, originally

developed for strain measurement. The technique is highly sensitive to surface displacement gradients, resulting from subsurface flaws associated with internal de-bonds, de-laminations and cracks.

DSSI measures derivatives of surface displacements, thus eliminating the need to numerically differentiate displacement data to yield strains. Strains are functions of displacement derivatives, thus shearography yields directly the strain information and it is suited well for NDT [28, 29]. Steinchen, W., *et al* [29], however, observes that, "the application of shearography for strain measurement has not been widely adopted in industry, because the shearogram usually contains both the out-of-plane component and the in-plane strain component". The authors further noted that, "Although the out-of-plane component can be separated out of the shearogram by manipulating the illuminating and viewing direction normal to the tested surface, the pure in-plane strain component can never be determined exactly by adjusting the illumination angle."

There is however, an approach which permits pure in-plane strain to be determined and this is the adoption of two linearly independent directions of illumination [13, 29]. In this case the shearograms for each illuminating direction is calculated by using the phase shifting technique (discussed later).The phase maps of the two shearograms are subtracted and this results into a new fringe pattern which represents the pure in-plane strain component. When the phase maps are added the fringe pattern formed correspond to the pure out-of plane component. Therefore, the in-plane strain component can be determined directly without differentiating displacement data numerically [29]. It can therefore be said that, by using the phase shift technique, digital shearography allows the shearogram to be evaluated automatically and numerically. This offers new possibilities for applications of shearography in industry. Although the theory for digital and photographic shearography is the same optically, digital shearography is technically a computerized process which does not use the film wet processing and reconstruction. This therefore makes it possible to quickly increase the testing speed so that the shearogram can be observed more or less in real time.

Speckle interferometry and laser theories are essential to the understanding of Digital shearography, and the following three sections describe these concepts briefly.

2.2.2 The Speckle interferometric theory

Speckle interferometric techniques rely on the very basic phenomenon of light interference namely that objects illuminated with laser light have a granular appearance. Speckle is observed when an object is illuminated with coherent laser light. Figure 2.6[13], shows a magnified speckle pattern of a shearographic image.

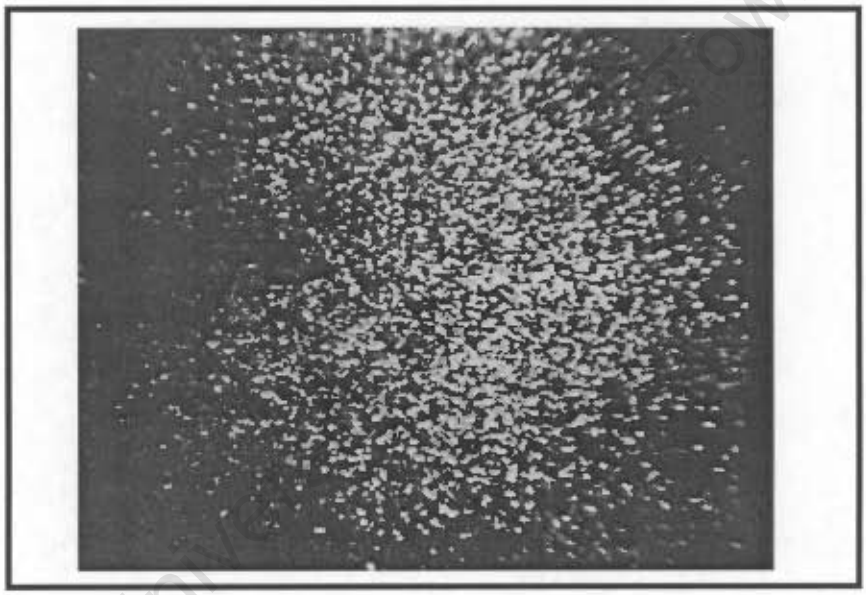

Figure 2.6: Magnified Speckle pattern of a shearographic image [13]

Most objects are optically rough even if they are rough only at a microscopic level. However, a speckle field can only be created if the height variation of a surface is of the order of or greater than the optical wavelength of the illuminating light.

2.2.3 Laser

Laser stands for light amplification by stimulated emission of radiation and it is an optical oscillator consisting of a light amplifying medium.Kim, H.J, *et al* [30], observed that: "Lasers produce unique light which is coherent, collimated and monochromatic. The other feature of a laser is the fact that it is possible to concentrate energy and to produce pulses of light which have short wave length. Because of these characteristics, lasers are used for measurements, manufacturing and communications."

The laser does not emit a simple form of light but it has variables that are quite constant with time and can be measured with high precision. This implies that lasers offer brightness, high degree of coherence and are monochromatic, which makes them the ideal light source for interferometry. However, a laser beam is only monochromatic over a certain distance and will approximate a sine wave of fixed frequency for a certain distance, known as the coherence length [31].
There are different types of lasers available with varying power, wavelength and coherence length that can be used for interferometry. The most commonly used laser is the Helium Neon (HeNe) laser, which is relatively inexpensive and easily available. The wavelength of the HeNe laser is 632.8nm, with power varying from 0.1 to 50 mw and the coherence length varying from 5 to 30 cm.

2.2.4 Principle of measurement with Digital shearography

Digital Shearography was developed using either a Michelson shearing interferometer or a birefringent crystal [32] as the image-shearing device. It has also been observed that, the key of shearography is the 'shearing" of the image [33].

A typical layout for digital shearography using a modified Michelson Interferometer as a shearing device is shown in Figure 2.7[34].

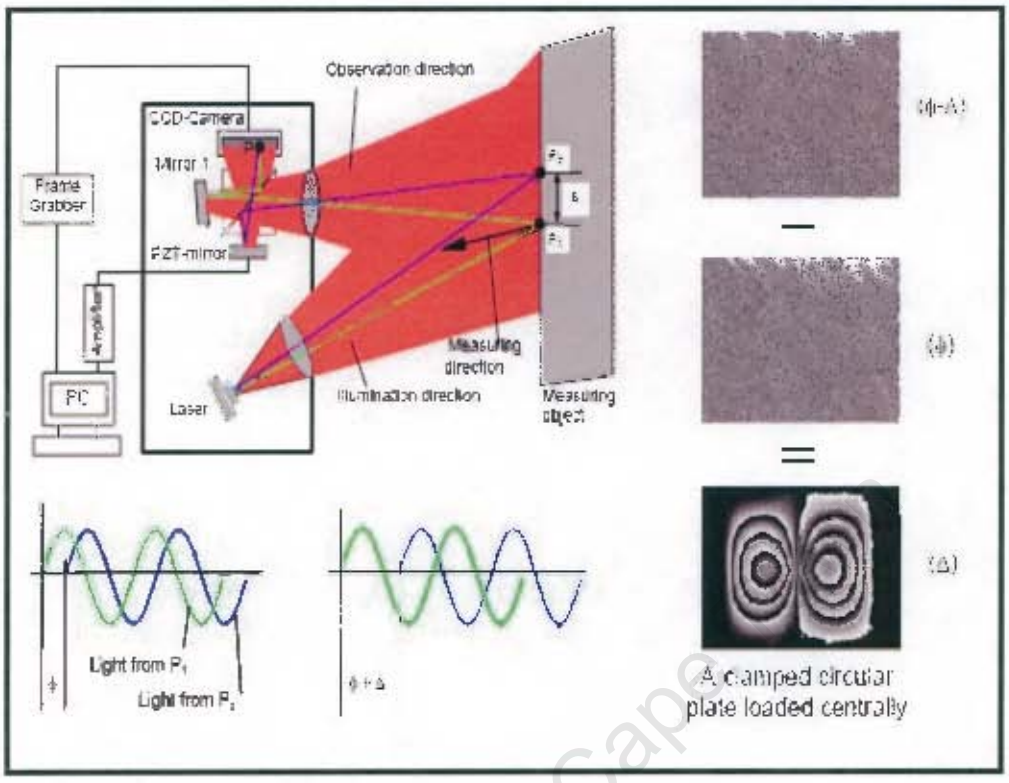

Figure 2.7: Typical Digital Shearography setup [34]

Obtaining a speckle interference pattern or image of the unstressed object is the very first thing you do in Digital Shearography. The image captured is then digitized and stored as a reference image. The Michelson interferometer brings the light waves from two points: P_1 and P_2, on the object surface into one point: P, on the image plane by tilting the mirror 1 a very small angle (Figure 2.7). The intensity of the interferogram is then registered by a CCD camera and saved in the computer through a frame grabber board.

As an illustration, a circular plate with fully clamped boundary subjected to central point load increment between two exposures with the use of small image shearing, shows the familiar double bulls eye that depict loci of constant displacement-gradients (shearography fringes). On the other hand, when large image shearing is used, concentric circular fringes that represent loci of constant out-of-plane displacements (holographic or ESPI fringes) are displayed [35]. This thesis, however, has not discussed holographic and ESPI techniques. Reference to the techniques has only been made due to the fact that,

shearography is an off spring of the two techniques, and hence it suffices to mention the other techniques with reference to fringe pattern formation if any distinction has to be made. Figure 2.8(a) and Figure 2.8 (b) demonstrate the type of fringes obtained.

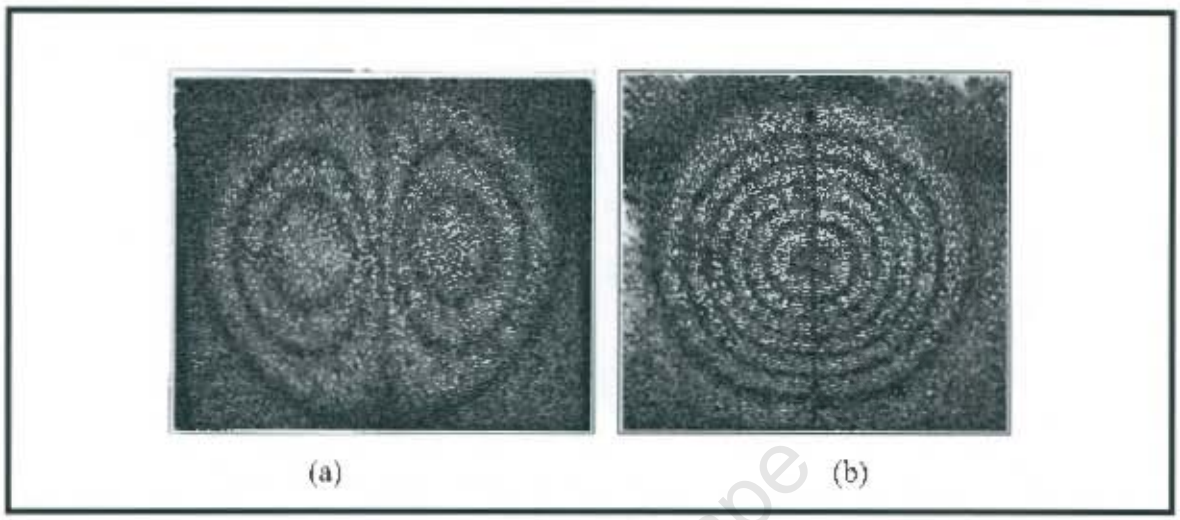

Figure 2. 8: (a) and (b) Fringe patterns for a centrally point-loaded circular plate (a) Formation of shearographic fringes due to small image shearing. (b) Formation of concentric circular ESPI or holographic fringes due to large image-shearing [35]

The intensity of any point on the speckle interference pattern, of the unstressed object, can be described mathematically by the following equation [36]:

$$I_o = 2A^2 (1+\cos (\theta x + \delta x - \theta x)) \qquad \text{Eq (2.2)}$$

Where A is complex amplitude of the combined wave fronts and is a function of the object illumination, δx is the magnitude of the shear and θx is a function of object beam and object surface orientation. The object is then stressed by either mechanical, pressure or thermal methods. Stressing of the object causes the relative displacement between two points on the surface of the object to change, which in turn causes the laser path length to change. This change of path length then alters the density distribution of the speckle pattern and the intensity can be expressed by the following equation as:

$$I_b = 2A^2 (1+\cos ((\theta x + \delta x - \theta x) + \Delta\phi)) \qquad \text{Eq (2.3)}$$

The variable $\Delta\phi$ in equation (2.3) represents the phase difference between the light waves from the two points P_1 and P_2, or derivative of object deflection, occurring due to the object being stressed. The speckle interference pattern, of the stressed object, is then digitized and stored. The phase difference $\Delta\phi$ can be extracted by either adding or subtracting the reference image from the stressed object image, described by equations (2.2) and (2.3) respectively. The subtraction process is achieved through the computer software, and this result in an interferogram with an intensity distribution as:

$$I_r = I_a - I_b = 4A^2 \sin\left((\theta x + \delta x - \theta x) + \frac{\Delta\phi}{2}\right)\sin\frac{\Delta\phi}{2} \qquad \text{Eq (2.4)}$$

The interferogram produced by equation (2.4) above maps the phase contours, which consists of black and white fringe patterns. This is due to areas of pixel intensity correlating or decorrelating, when the two images are subtracted, to form the interferogram. Correlation will take place when the phase difference is as follows [37]:

$$\Delta\phi = 2n\pi \text{ where } n = 0, 1, 2 \ldots \qquad \text{Eq (2.5)}$$

This condition corresponds to the dark fringes on the interferogram. In contrast decorrelation will take place when the phase difference is as follows:

$$\Delta\phi = (2n+1)\,\pi \qquad \text{where } n = 0, 1, 2\ldots \qquad \text{Eq (2.6)}$$

This condition corresponds to the bright fringes on the interferogram. The fringes can be modeled by the following mathematical equation [37]:

$$\Delta\phi = \frac{4\pi}{\lambda}\left(\frac{\partial d}{\partial x}\right)S \qquad \text{Eq (2.7)}$$

Where $\Delta\phi$ is the correlation phase, $\frac{\partial d}{\partial x}$ is the rate of surface displacement, S is the magnitude of shear (distance between common point that are sheared) and λ is the

wavelength for laser light. The above equation shows that the correlation fringes represent lines of constant displacement rates, where $\Delta\phi$ is constant. The sensitivity of the interferometer can be varied by increasing or decreasing the angle of shear and thereby varying the magnitude of shear S. Therefore it can be seen from equation (2.7) that the greater the magnitude of shear the larger the phase difference $\Delta\phi$, this therefore increases the sensitivity of the interferometer.

If the phase difference in equation (2.7) is replaced by equation (2.5) then the spacing between adjacent fringes as function of the displacement gradient can be obtained and is described by equation (2.8):

$$\frac{\partial d}{\partial x} = \frac{n\lambda}{2S} \quad \text{Where } n = \text{number of fringes} \qquad \text{Eq (2.8)}$$

Equation (2.8) confirms that for a given surface area, an increase in displacement gradient will produce a corresponding increase in the number of fringes. Furthermore the number of fringes around a defect area indicates the amplitude of the localized displacement induced, which is influenced by the size of the defect and its depth.

Figure 2.9 shows the image, where the dark fringes represent the case of $n = 0,1,2,3,...$ as mentioned above.

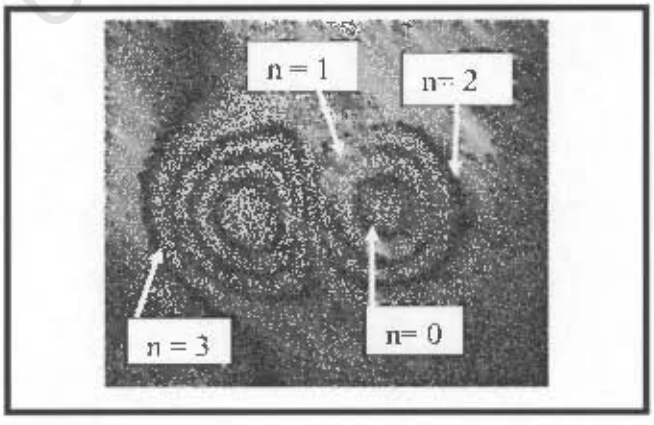

Figure 2.9: Fringe patterns with dark fringes

2.2.5 Interpretation of fringes in shearography

Shearography measures surface deformation and therefore yields derivatives of the surface displacements. The fringe pattern of shearography is a double concentric fringe pattern, and a plot of the deflection derivative of a clamped circular plate loaded centrally will appear as shown in Figure 2.10 below [38].

Figure 2.10, also shows that, there are two lobes in the displacement derivative plot which explain why a double bull's eyes fringe pattern is formed in shearography.The size of the defect in shearography is thus determined by measuring peak to peak the line profile, where the length between two peaks is varied according to the change of the effective factors [39].

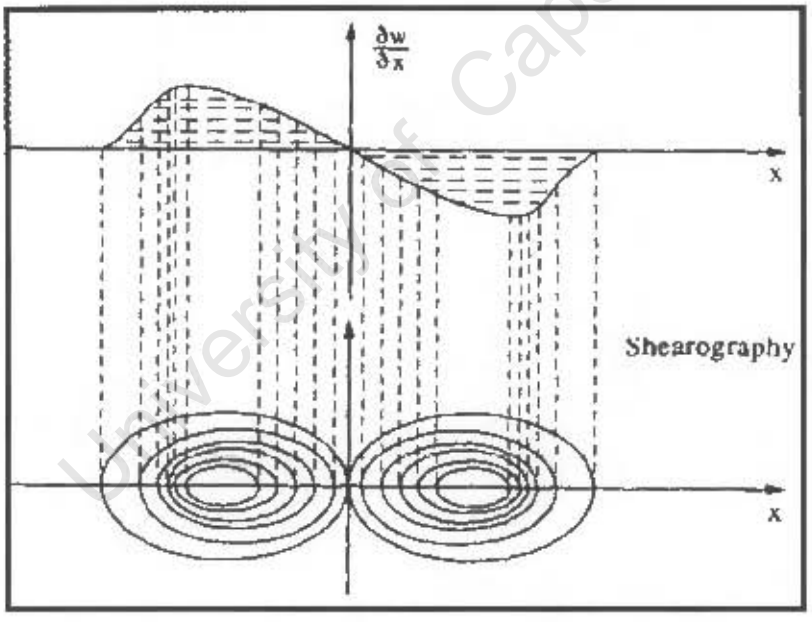

Figure 2.10: Double bull's eye in Shearography and peak to peak line profile [38]

If a material or specimen has a defect and is adequately loaded by vacuum, thermal or mechanical loading, it will experience a "buckling effect" on the surface which will facilitate the detection of the flaw by shearography. In other words shearography will

detect the flaw by looking for strain induced by the defect. Figure2.11 below illustrates the concept of flaw detection and fringe pattern formation.

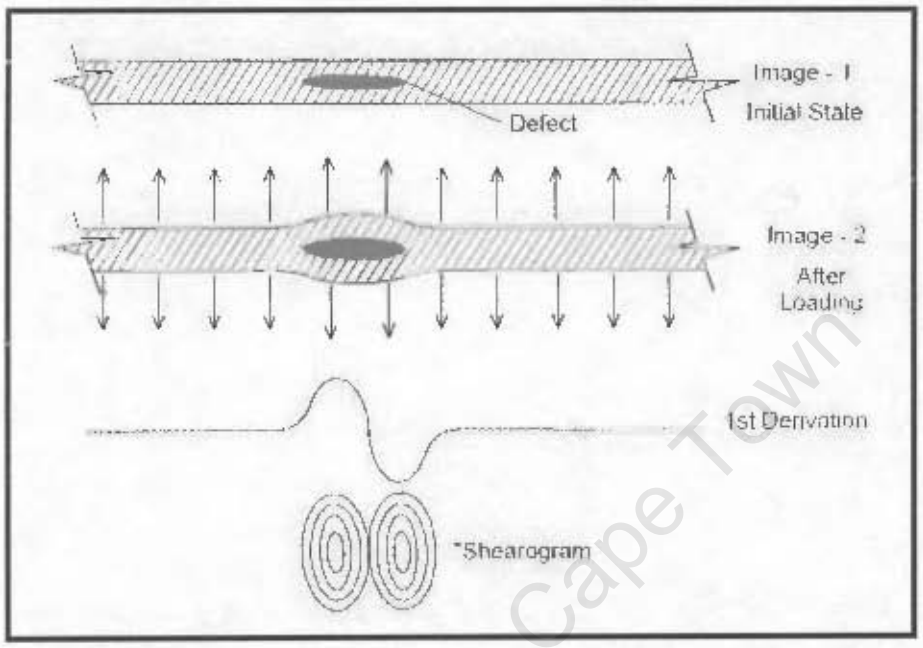

Figure 2.11: Process of fringe pattern formation (shearogram) [34]

Fringes can appear either vertically or horizontally due to deformations in the sensitivity direction (either x-axis or y-axis). Therefore vertical fringes appear along the x-axis and horizontal fringes appear in the y-axis. Each fringe represents a line where all points along it undergo the same amount of deformation. This implies that, the fringes are contour lines of constant displacement in the particular direction or axis. The closer the fringes are to each other, the bigger change in deformation has occurred. This means that, there is a higher strain in that area [40].

Fringes will also appear differently, depending on whether deformation is linear or it varies. Figure 2.12(a) shows how the fringe pattern will appear as equal distant fringes when the strain is constant. This suggests that, the deformation is linear. If the strain varies as 1/x, the fringes will appear closer together where the strain rate is high, as can be seen in Figure 2.12(b).

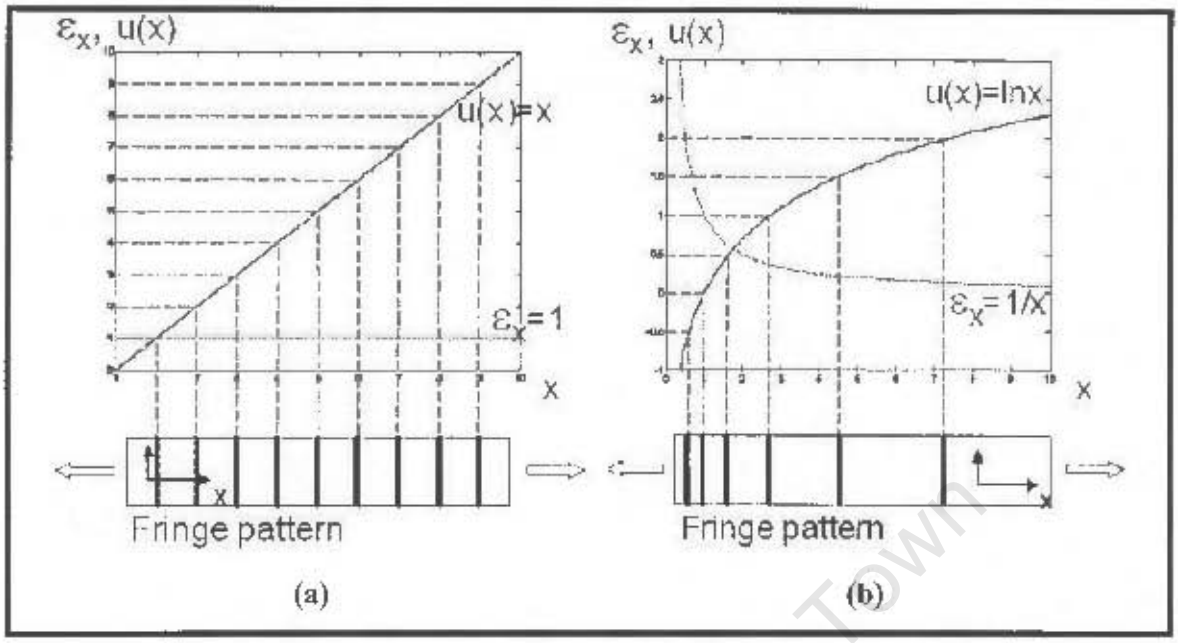

Figure 2.12: (a) Constant strain, i.e. linearly increasing deformation gives rise to equally spaced fringes; (b) High strain rate will give fringes that are closer together [40]

To illustrate how the phase maps (fringes) appear when there is deformation in x- and y-axis respectively $(\frac{\partial w}{\partial x};\frac{\partial w}{\partial y})$; fringes of a rectangular plate clamped along its boundaries and subjected to uniform pressure can be used as an example. These are shown in Figure 2.13.

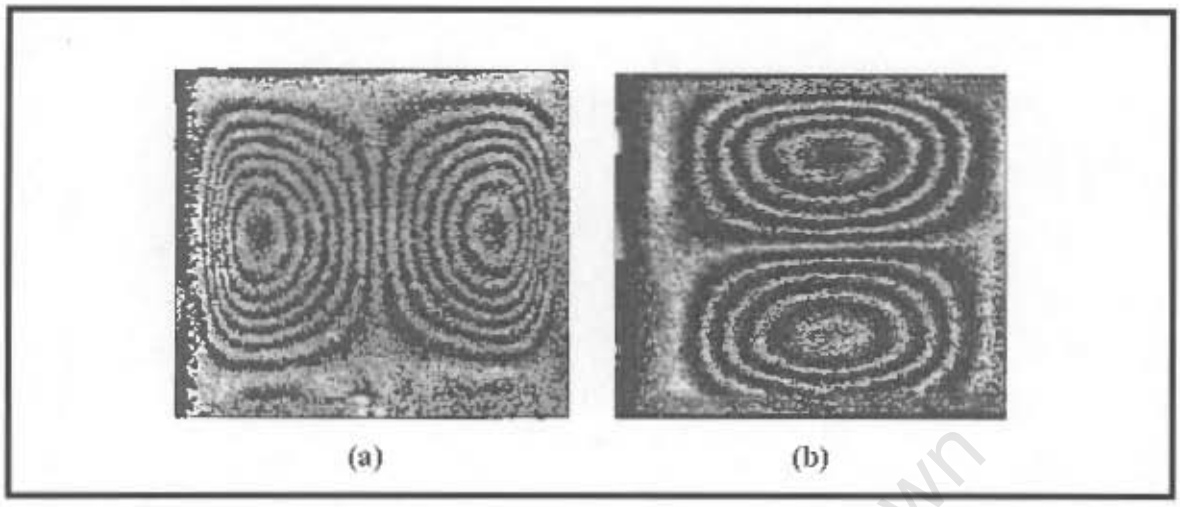

Figure 2.13: Fringe patterns depicting the deflection derivatives of a rectangular plate clamped along its boundaries and subjected to uniform pressure: (a) $\frac{\partial w}{\partial x}$; (b) $\frac{\partial w}{\partial y}$. [13, 41]

The corresponding three-dimensional plot of the phase distribution in fringe patterns of Figure 2.13(a) produced by phase determination technique is shown in Figure 2.14 below.

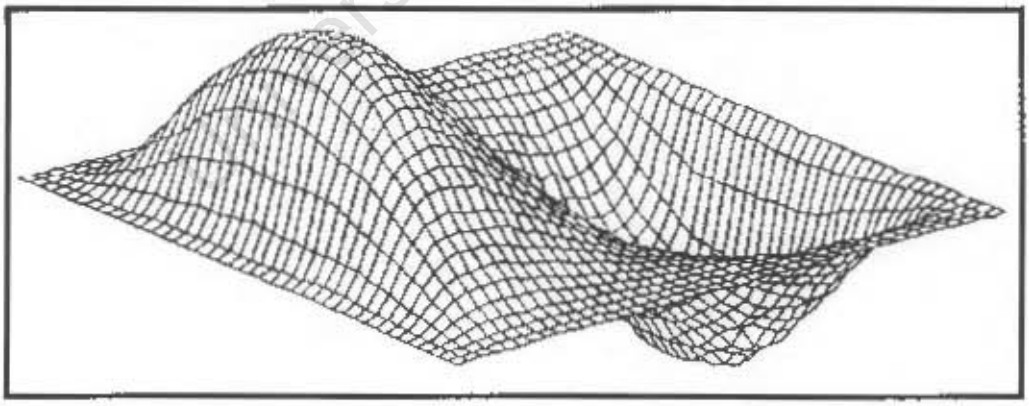

Figure 2.14: Three-dimensional (3D) plot of the phase distribution determined by the phase shift technique [42]

2.2.6 Phased-Stepped Shearography

Digital Shearography, as described above, produces intensity based fringe patterns, which do not provide any information regarding the direction of object displacement. In order to quantify the object's rate of displacement, the modulation of the laser phase due to the applied stress needs to be determined as well[43]. This can be achieved using a technique called phase stepping. This technique eliminates the need of human interpretation of the fringe pattern [44]. The following sections describe the analysis of speckle patterns and the resulting phase map that is manifested when using phase-stepped shearographic NDE. Filtering is discussed as means of substantially improving the phase image quality.

2.2.6.1 Phase- Stepping

Phase-stepping is a quantitative method of data measurement and is derived from the intensity integration method [45]. This technique requires a minimum of three measurements (i.e. interferograms) to solve for three unknowns at each point in a fringe pattern; however, four measurements or interferograms are more commonly used. Phase measurement is based on superimposing a uniform phase on the original fringe pattern, thus producing a phase shift in the fringe pattern. Digitizing three fringe patterns with different amounts of phase shift provides three equations for the solution of three unknowns, and the phase distribution is thus determined.

Phase steps are produced by micro displacements of a piezo-electrically driven mirror, which is calibrated before testing can commence. Each micro displacement of the calibrated piezo-electrically driven mirror initiates phase steps of $\pi/2$ increments, which is equivalent to changing the path length of the beam by a quarter of a wavelength.

The piezo-electrically driven mirror can be attached to either arm of the Michelson Interferometer. After each phase-step an interferogram, is grabbed by the image

processing system. The measured intensity $I_i(x,y)$ of the interferogram, at any given co-ordinate (x,y), can be described by the following equation [46]:

$$I_i(x,y) = I_B(x,y) + I_m(x,y)\cos(\phi(x,y) + i\alpha) \qquad i = 1, 2 \ldots N \qquad \text{Eq (2.9)}$$

where, $I_B(x,y)$, is the background intensity, $I_m(x,y)$, is the modulation intensity, $\phi(x,y)$, is the phase difference between the object and reference beam and α, is the relative phase (i.e. $\pi/2$). When four images are grabbed (i.e. when i goes from 1 to 4), the process is known as the 4-bucket system [47].

$$Since \cos\left(\theta + \frac{\pi}{2}\right) = -\sin\theta \text{ and } \cos(\theta + \pi) = -\cos\theta \qquad \text{Eq (2.10)}$$

$$I_1(x,y) = I_B(x,y) - I_m(x,y)\sin(\phi(x,y)) \qquad \text{Eq (2.11)}$$

$$I_2(x,y) = I_B(x,y) - I_m(x,y)\cos(\phi(x,y)) \qquad \text{Eq (2.12)}$$

$$I_3(x,y) = I_B(x,y) + I_m(x,y)\sin(\phi(x,y)) \qquad \text{Eq (2.13)}$$

$$I_4(x,y) = I_B(x,y) + I_m(x,y)\cos(\phi(x,y)) \qquad \text{Eq (2.14)}$$

It can be seen that equation (2.10) produces four trigonometric equations as described by equations (2.11)-(2.14), which can be solved to eliminate the unknown background intensity $I_B(x,y)$. The phase difference can only be calculated after the background intensity $I_B(x,y)$ is eliminated as discussed in the next section.

2.2.6.2 Phase Change Distribution-Calculation

The technique described above provides a wrapped phase distribution, $\phi(x,y)$, which still contains the spatially random phase distribution described by the background intensity $I_B(x,y)$. The background intensity $I_B(x,y)$ is removed by subtracting equation (2.12)

from (2.14) and equation (2.11) from equation (2.13) which yields equation (2.15) and (2.16) respectively.

$$I_4 - I_2 = 2I_{mp}(x,y)\cos(\phi(x,y)) \qquad \text{Eq (2.15)}$$

$$I_3 - I_1 = 2I_{mp}(x,y)\sin(\phi(x,y)) \qquad \text{Eq (2.16)}$$

The phase can be described as a function of the four intensities by the following equation [48]

$$\phi(x,y) = \tan^{-1}\left(\frac{I_3(x,y) - I_1(x,y)}{I_4(x,y) - I_2(x,y)}\right) \qquad \text{Eq (2.17)}$$

The phase difference $\psi(x,y)$ can then be calculated by using the following equation:

$$\psi(x,y) = \phi_b(x,y) - \phi_a(x,y) \qquad \text{Eq (2.18)}$$

where, $\phi_b(x,y)$ and $\phi_a(x,y)$ represent the phase before and after deformation respectively. The inverse tangent in equation (2.17) ranges between $-\pi/2$ to $\pi/2$ but does not provide the true phase since values after $\pi/2$ till $3\pi/2$ are not within the limits. If the sign of the sine and cosine were taken into consideration then this solves the problem. If the cosine is negative, then it will be in the second and third quadrant and π is added to the arctangent value to get the correct phase. The phase difference $\psi(x,y)$ is then calculated using equation (2.18) and is limited to the range of -2π to 2π and thus contains 4π discontinuities. This range is then shortened so that the limit is from 0 to 2π since a wave repeats itself after every 2π. Taking the absolute of the phase difference is one method of shortening the range but this method produces noise, a second and better method is to add 2π to the negative result of the subtraction of the two waves.

Upon calculating the true phase difference through, the image processing software, a phase map consisting of fringes ranging from black to white and suddenly changing back to black will be produced. This "saw tooth Pattern" continues throughout the image. This

drastic change occurs due to phase difference increasing towards 2π and then jumping back to zero when the limit of 2π is reached. This means that in the final image black represents the smallest phase difference and white the largest. The regions where these discontinuities occur are called 2π discontinuities and they are the main characteristics of phase stepping in helping to determine the relative direction in which deformation takes place.

2.2.6.3 Filtering of Phase fringe patterns

After calculating the phase difference for the individual pixels in an image and a phase map is produced, a common way to improve visibility of the fringes is to filter it. Speckle noise and 2π discontinuities in phase fringe patterns are characterized by high spatial frequencies. Hence, by applying a low-pass filter not only reduces the noise, but also smears out the discontinuities[49].This problem is solved by calculating the sine and cosine of the wrapped fringe patterns , which leads to continuous fringe patterns. These sine and cosine fringe patterns are then filtered separately using an average filter, which considers the average value of a group of neighbouring $n \times n$ pixels for each pixel in the image, where n is an odd integer number. From the filtered sine and cosine fringe pattern the phase fringe pattern is calculated by the four-quadrant inverse tangent of the sine and cosine patterns. This process of filtering can be repeated two or three times. Figure 2.15(a) shows an unfiltered phase-stepped image and Figure 2.15(b) shows a filtered phase map.

(a) (b)

Figure 2.15: (a) Phase fringe pattern affected by noise (b) Phase fringe pattern excellently filtered

It can be seen from Figure 2.15(b), that an average filter applied say 30 times with intermediate phase recalculation yields an excellently filtered image. The noise is effectively suppressed and all fringes are perfectly preserved.

In his study, Hung,Y.Y [13], observed that, shearography had already received wide industrial acceptance for NDT and that, currently the rubber industry routinely uses shearography for evaluating tyres, and aerospace industry has adopted it for NDT of aircraft structures, in particular, composite structures. Figure 2.16 is a shearography fringe pattern revealing separation along the steel belt-edge of a truck tyre.

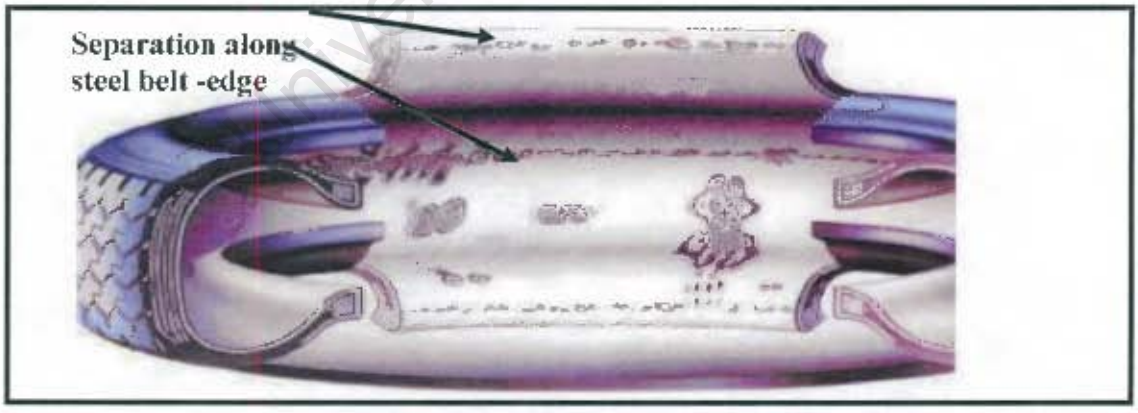

Figure 2.16: Shearography fringe pattern revealing separation along the steel belt-edge of a truck tyre [13]

Hung Y.Y. [38], further did an in-depth comparative study of Digital Shearography and ESPI and observed that: "Shearography requires a simpler optical setup, thus eliminating the optical alignment problems; Shearography provides a wider and more controllable range of sensitivity, thus allowing large deformations to be inspected which is not the case in ESPI(ESPI is too sensitive for many practical NDE applications); rigid body motion does not influence the resulting fringe patterns, since Shearographic NDE uses a "common path" optical arrangement and finally the coherent length requirement is greatly reduced".

Mayer,T [50] also confirms that shearogarphy allows large component areas to be measured in a short time and thus it is the optimal technique for fault detection. The author, further affirms that the shearography system is already used in tyre testing machines for quality control in industrial conditions and that the technique is ideal especially for the aircraft manufacturing and maintenance, in which large component surfaces can be tested in short time. Other applications of shearography include measurement of strains, material properties, residual stresses, 3D shapes, as well as vibration studies. All these advantages have rendered shearography a practical measurement tool.

Gryzagoridis and Findeis [51] carried out an experiment to compare the capabilities of portable shearography and portable ESPI in the detection of composite aircraft components. In order to compare the performance of each prototype, suitable test samples with known defects had to be manufactured. The authors used a 500 mm length of the rotor blade and five defects were introduced into this sample. The inspections were conducted outside the laboratory environment. It was concluded that, both systems performed well outside the laboratory environment without any special additional vibration isolation requirements, and that both techniques were also able to detect the presence of the internal delaminations. However, when considering the implementation of the two techniques, the authors observed that, ESPI produced the best results only during the cooling process. It was further noted that, Shearography generated good results

by either viewing the effect of applying heat to the test piece or by viewing the cooling down process.

Pezzoni [52] investigated the capability of shearography in the testing of large area composite helicopter structures. Initially a composite structural element panel of a tail unit of a helicopter as shown in Figure 2.17 was investigated. This part is a typical structure with a nomex honeycomb core and two external skins in graphite/epoxy uni-directional cross-ply. The thickness of the honeycomb was about 13 mm, and each of the external surfaces measured about 1 mm in thickness. This sample was specially prepared with several typical delamination faults, synthetically introduced using Teflon inserts. For inspection, this panel was thermally loaded with a set of up to four IR lamps. The results in Figure 2.18, showed an image of an unloaded and thermally induced deformed panel exhibiting very low contrast and strong noise. Additionally the image revealed some impact damages which can easily be seen on the outer surface. After image improvement operation using an appropriate combination of filtering and contrast operations the fringe visibility was significantly improved although the defect visibility was relatively poor.

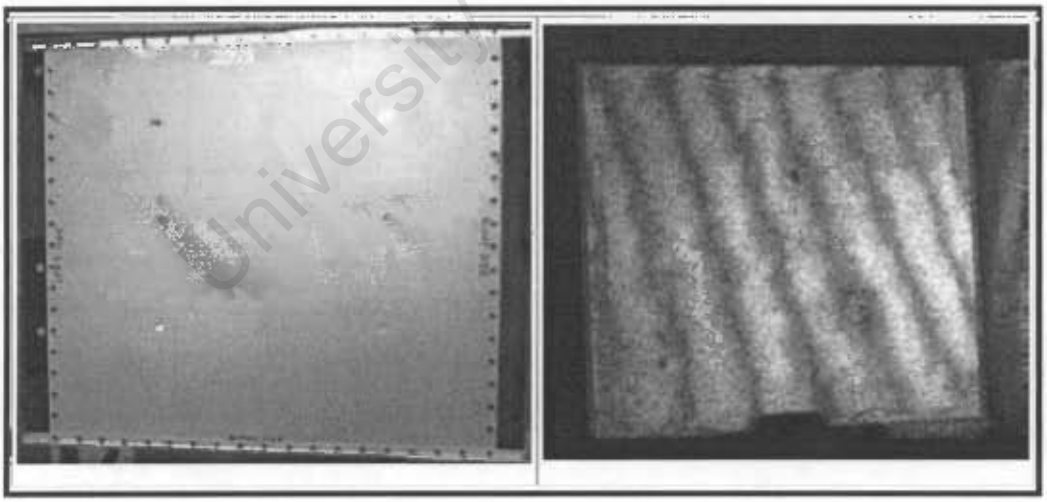

Figure 2.17: Composite helicopter panel ***(above left)***

Figure 2.18: Improved D-image ***(above right)***

Phase shifting technique and filtering were applied to the images and the results are shown in Figure 2.19 and Figure 2.20. The phase shift could easily be introduced by moving one of the two mirrors of the shearing element.

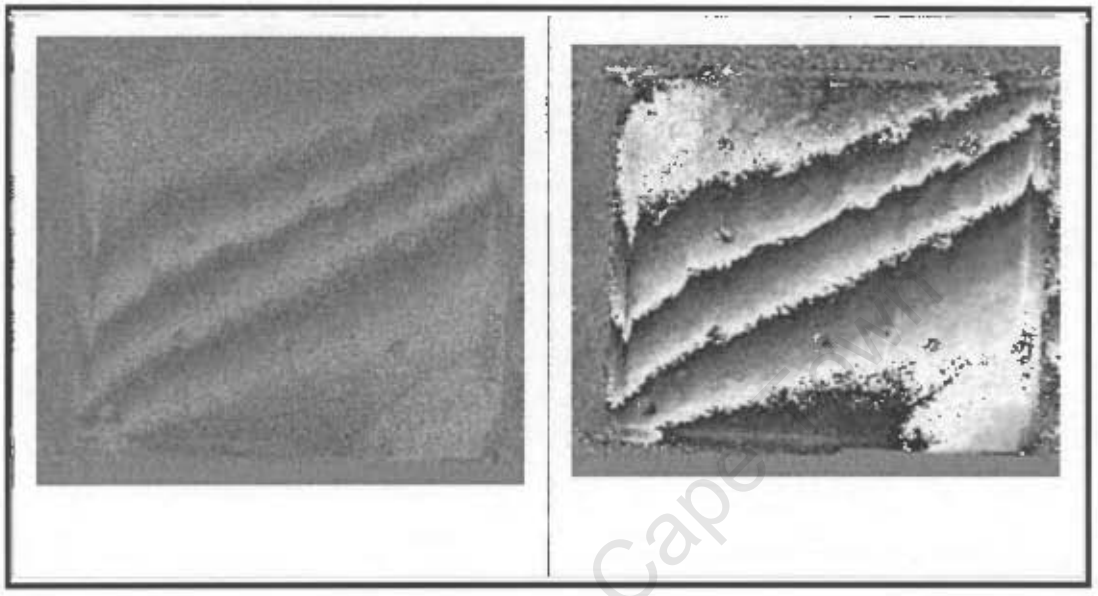

Figure 2.19: Phase image (*above left*)

Figure 2.20: Filtered phase image (*above right*)

Pezzoni, increased the size of the sample to be tested significantly by taking an original full tail unit of a helicopter. This unit measured about 3.5 m in height and 3.5 m in width. On the lower right part, a disbond was introduced between the honeycomb core and the outer skin. The defect was round shaped and measured about 70 mm in size. Besides the defect detection the other interest was in structural features of the sample. Figure 2.21 shows an image of a full helicopter tail unit. The corresponding phase map is shown in Figure 2.22. The author concluded that shearography, allows the real-time non-contact and non-destructive detection of defects and structural properties of composites and other lightweight structures. It was further, observed, that the use of pulsed laser for illumination shows significant benefits due to large inspection area (up to 10 m^2) and suppression of environmental influences, which makes the system also useful for "in-situ" applications outside a laboratory.

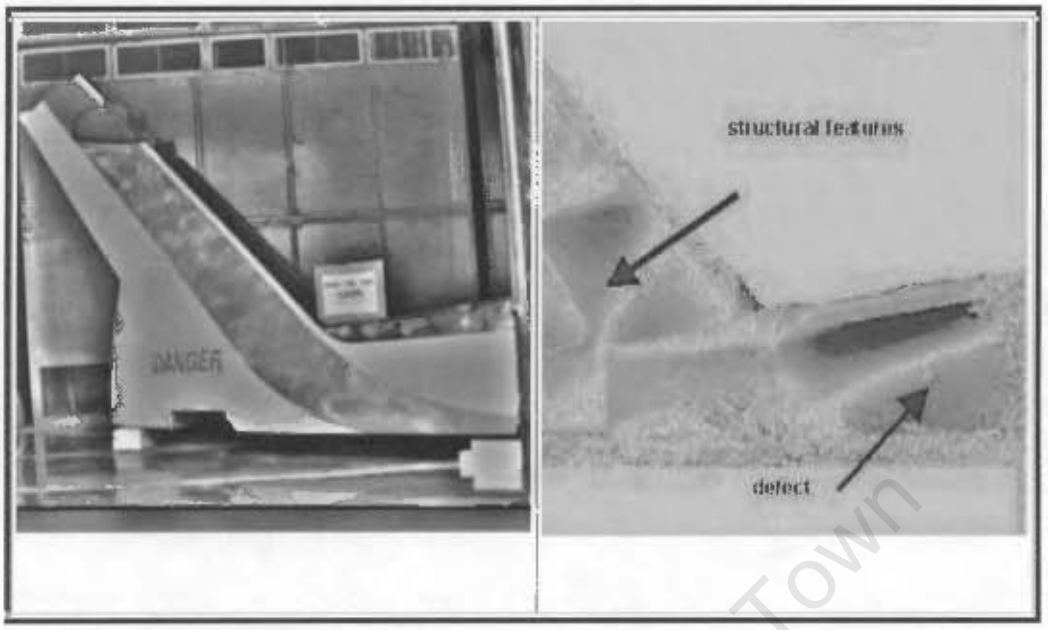

Figure 2.21: Full helicopter tail unit *(above left)*

Figure 2. 22: Wrapped phase map of 3m x 3m area of the tail unit (thermal loading) *(above right)*

It was therefore, deduced that, the technique is capable of detecting defects in wide scale structures, strongly reducing the inspection time, and hence it was validated as very promising in the field of aerospace (composites, lightweight structures) particularly for the production-NDT of aircraft components, fatigue testing monitoring and maintenance inspections.

Kalms and Juepter [53] in collaboration with Airbus Germany (NDT-Group Bremen) and EADC Military Aircrafts carried out shearographic investigations on airplane components. An aircraft wing and an aluminium body of the aircraft were investigated for defects under thermal loading. The aluminium honeycomb structure from the aircraft was a metal-metal bonded aluminium type with pocket damages through the honeycomb structure. The size of the smallest defect was 10 x 10 mm. Figure 2.23 shows the mobile shearographic equipment setup used for the inspection of an aircraft wing. The inspection was done in a real maintenance environment.

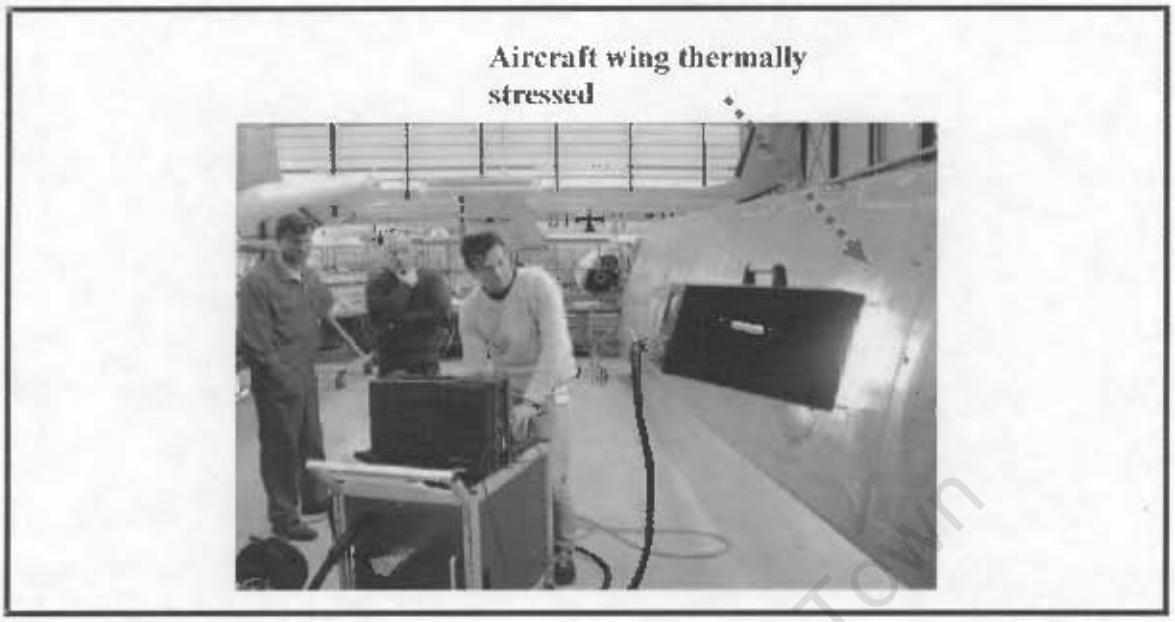

Figure 2.23: Mobile Shearographic equipment applied on an aircraft wing [53]

Figure 2.24 below shows an inspection of aircraft fuselage, metal-metal bonded aluminium with pocket damages through the honeycomb, in progress. The authors did other tests on honeycomb sandwich structure such as the rudder in which the component was inspected for water ingress. Other aircraft components investigated were skin damage over the stringer, stringer debondings, and damages of the airbrake located at the wings of the airplanes.

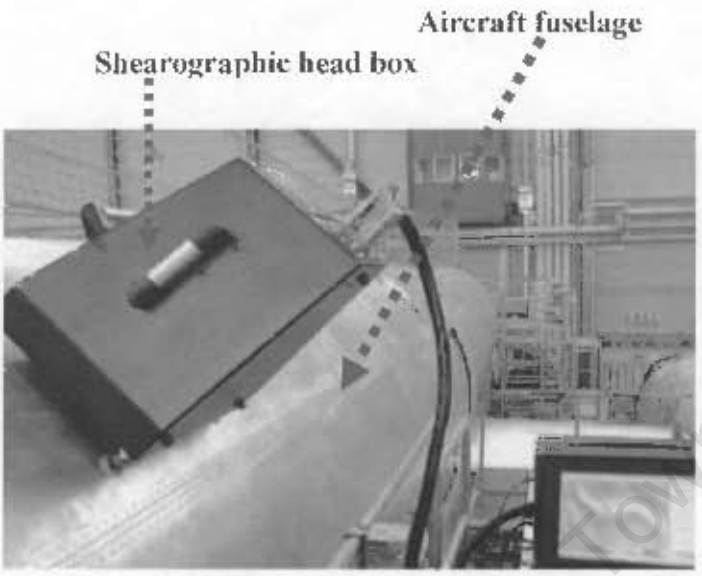

Figure 2.24: Shearographic head box applied on an aircraft fuselage [53]

In all the inspections done, it was reported that, all damages were clearly visible, and that shearography was even able to locate the unknown damage which was equally detected by radiographic investigation (white marked area in Figure 2.25). Figure 2.25 and Figure 2.26 shows the successful X-ray and shearographic measurement results respectively.

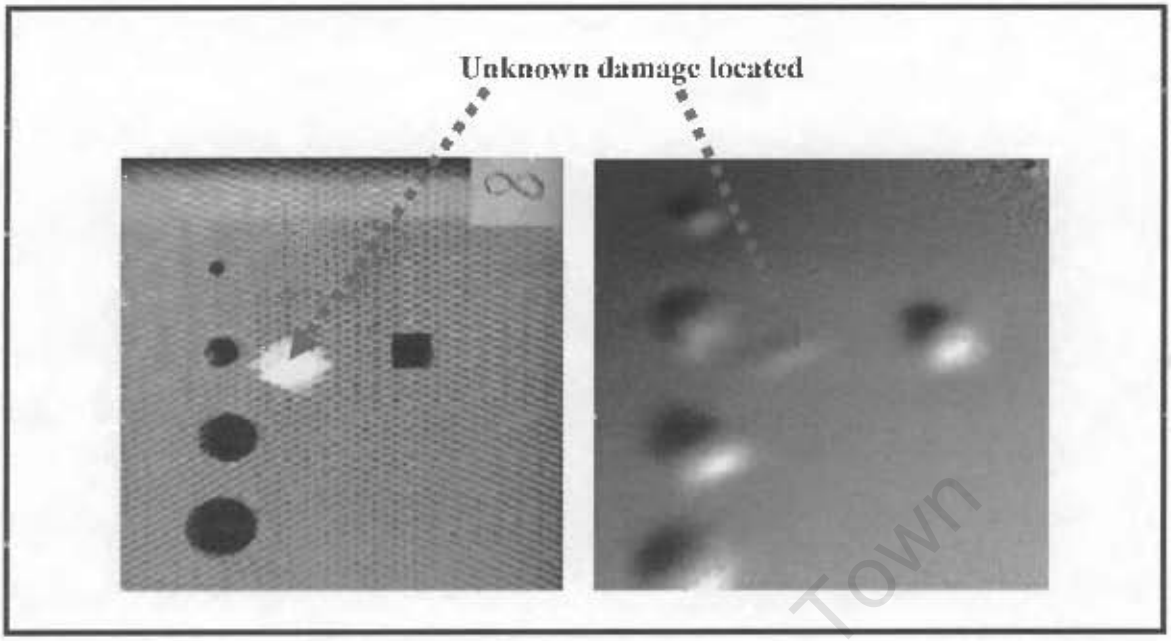

Figure 2.25: X-ray result image *(above left)*

Figure 2.26: Shearographic result image *(above right)*

The authors finally confirmed that shearography was a successful and comprehensive testing device for the inspection of aircraft structures.

Hung, Y.Y. [54] did a comparative study of digital shearography with a C-scan ultrasonic technique in the test of a graphite sandwich panel. Two flaws in the inspection were revealed by both techniques. However, digital shearography revealed the flaws as soon as the stress was applied, whereas the ultrasonic technique required point-by-point scanning of the part. Moreover, fluid coupling of the transducer to the test object was needed in the ultrasonic testing, thus making the technique cumbersome and too slow for production inspection, and shearography did not require any contact. It was observed that the time taken to reveal the flaws (unbonds and edge pullout) by shearography was 8 seconds while C-scan ultrasonic took 10 minutes to scan the part.

Siew-Lok Toh and Fook-Siong Chau [55] used digital shearography to test a composite plate with suspected debonds using vacuum stressing. The simulated glass-reinforced polyester (GRP) flat plate of about 270 x 250 millimeters was used in the investigation.

The GRP plate was placed in a specially constructed vacuum chamber and double-exposure shearography was performed; one exposure before and one after a vacuum pressure were applied. It was oberseved that, vacuum stressing is an effective method for the detection of delaminations or debonds in composites and that the technique has the advantage of being non-contacting, yielding a fast response, and covering the full field.

Honlet, Ettemeyer and Walz [56] used an automated inspection system which uses laser shearography and vacuum chamber for the inspection of helicopter rotor blade for defects. The rotor blade was positioned in the vacuum chamber and loaded with slight pressure changes of less than 50 mbar. The pressure change in the vacuum chamber was intended to produce slight deformations on the surface of the rotor blade so that shearography could observe these deformations, and automatically indicate defects such as delaminations, debondings, etc., which would show up by typical deformation patterns. The authors concluded that the automatic inspection system significantly reduced the elapsed time for a complete inspection cycle of large, main rotor blades in comparison to the manual inspection. Figure 2.27 shows the inspection results on both sides of 800x600mm^2 field on the rotor blade with defects, manifesting as local delaminations.

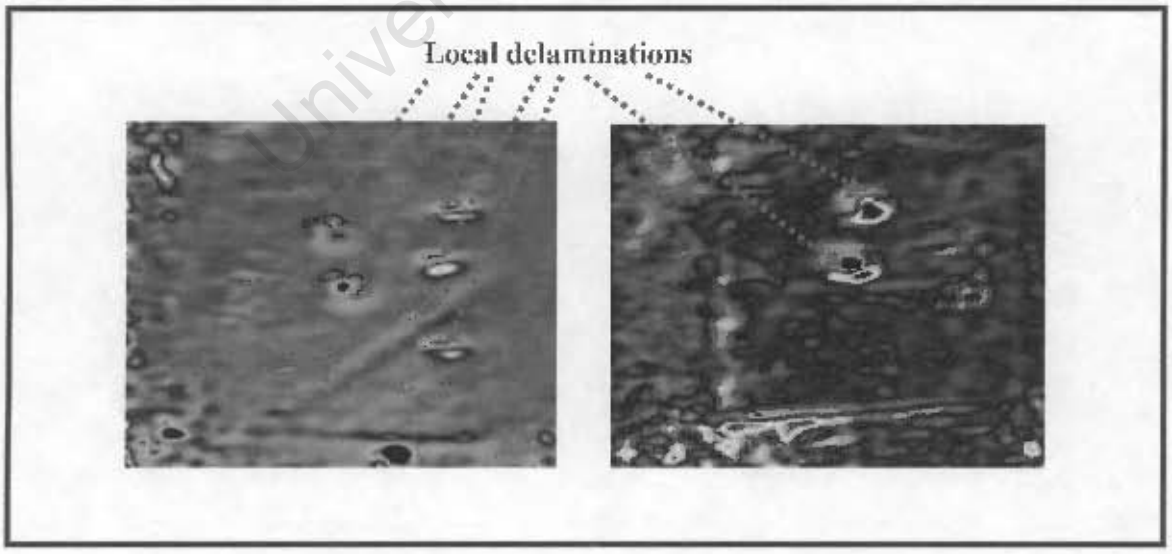

Figure 2.27: Inspection results on both sides of 800x600mm^2 field on the rotor blade with defects [56]

Sim C.W. *et al* [57] carried out a comparison study of vibration analysis and non-destructive testing of the specimen with real-time shearography. In the study, the potential of using dynamic stressing in real-time shearography was explored. The entire experiment consisted of two phases. Phase one involved vibration analysis using real-time shearography and the specimen under test was a square cantilever aluminium plate with sides of 50 mm and thickness of 0.88 mm. This plate was illuminated by an expanded beam of a 60 mW HeNe laser of 632.8 nm wavelength. The real-time shearograms corresponding to five resonance vibration modes at increasing excitation frequency were recorded. Phase two of the experiment involved non-destructive flaw detection in composites plates made from mats of glass-fibres. A 60 mW HeNe laser of 632.8 nm was also used to illuminate the specimen. It was deduced that, real-time shearography coupled with vibrational means of stressing is a convenient and effective way of determining the out-of-plane displacement gradient of a vibrating structure at resonance mode. It was further established that, shearography can be used to detect debonds or delaminations in composite plates.

Andersson and Barend [58] did a feasibility study of various NDT methods in order to identify and verify a cost effective inspection method for a stiff stainless steel skin sandwich construction with a low-density core. The study required the detection of artificially created disbonds in the structure. The investigation included literature studies, selection of feasible methods, evaluation of the methods and finally selection of a preferred NDT-method and application trials. The NDT methods used included: Ultrasonic, resonance technique (described as spectroscopy), Mechanical Impedance technique, Pitch-and-catch technique (described as velocimetric method), Bondimeter technique and shearography. The first four techniques mentioned did not give reliable indications of the defects. Some techniques only gave vague indications that were not different to the general variation obtained in defect free areas. The authors, however, continued the investigation with the application of shearography, and the following were considered at the application trials; excitation method, geometry effect on results, inspection areas (limitation of technique) and defect characterization (sizing and depth position). Other inspections were made on thicker and thicker test samples to try to find

the skin thickness limitation for shearography. For thicker skins larger temperature differences were necessary to detect defects. It was found that from the 50 mm diameter, defect detection was vaguely distinguished from the background noise on doubler bonded to foam core, and the 25 mm diameter defect was detected in bondline between the 3 mm skin and 2 mm doubler. The authors concluded that, shearography successfully detected and estimated depth position of the defects in relatively stiff areas. Figure 2.28 and Figure 2.29 shows shearographic results of the defects.

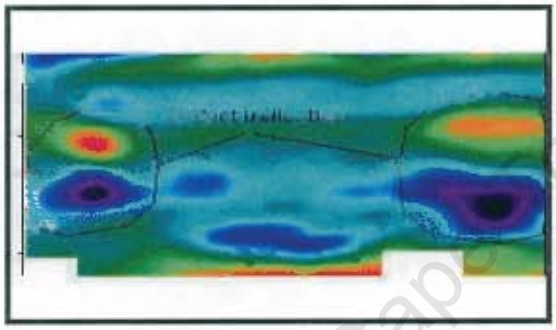

Figure 2.28: Shearography results on: (a) Disbond type I, an area left without adhesive, (b) Disbond type II, A plastic foil taped to the skin [58]

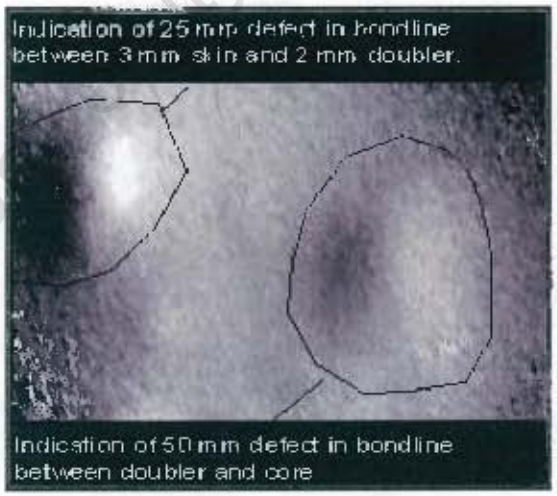

Figure 2. 29: Shearography results on thicker samples [58]

Lt. Col. Slawomir *et al* [59] carried out a study to determine damages which could be detected and which happen during the service life of main rotor blades (MRB) of helicopters used in Polish Armed Forces. The damages under investigation included: disbonds (skin to honeycomb, skin to spar) both metal and composite MRB; delaminations (composite skin); cracks (mainly in the metal MRB); and water ingress (honeycomb cells). Selected NDT techniques such as: D-Sight, Shearography, MIA, Pitch-Catch, Ultrasound, Ultrasound Phased Array, and Eddy Current were used in the study. Shearography with vacuum loading was applied for disbonds inspection, and the authors rated the technique to have good sensitivity and high speed of inspection. Figure 2.30 shows the results of the shearographic inspection of the skin to honeycomb disbonds.

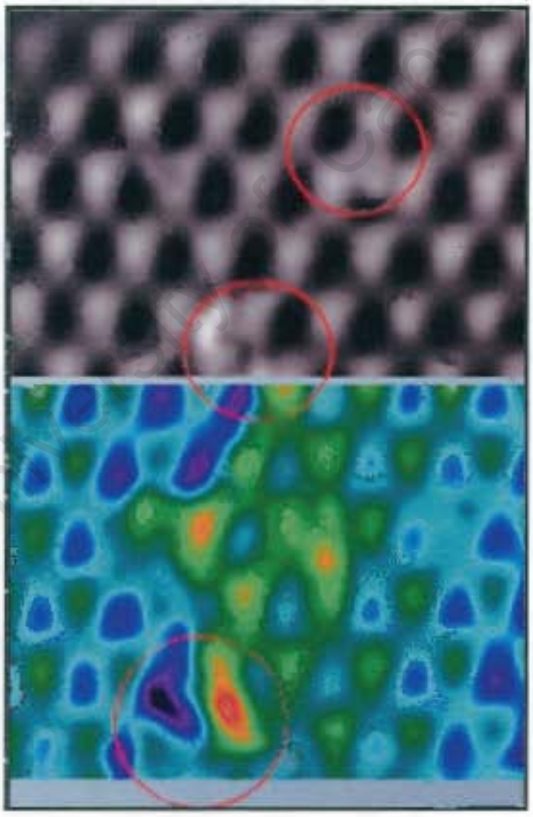

Figure 2.30: Skin to honeycomb disbonds with a variety of "double bull's eyes" [59]

CHAPTER 3

3. Impact damage detection in aircraft composite materials

3.1 Damage in Composite materials

Composite materials and in particular Carbon Fiber Reinforced Plastics (CFRP) are currently used more in structures and components of both civilian and military aircraft because of their mechanical resistance, high toughness, low- specific weight and resistance to corrosion in comparison to metals. Thus, accordingly with non-homogeneous nature of the material, measures must be taken to preserve the structural integrity of the aircraft. This can be achieved by ensuring that the frame pattern of the fibers is not compromised [24]. Composite materials are exposed to various damages during their service life which may be due to static loading, low energy impact during the manufacture and environmental factors such as moisture ingress etc.

Sala, G. [60] confirms that, environmental agents that cause damage to composites are "electromagnetic effects, fire and high temperatures; lightning and electrical discharges, ozone (chemical degradation); ultra-violet radiation (UV); out-gassing at high-vacuum; erosion by rain and sand; low-energy impacts (by hail or gravel) that induce BVID; moisture uptake, and contact with organic liquids such as fuels, lubricants and de-icing fluids." The author also pointed out that, during normal service, aircraft are exposed to all these agents with time, and hence, the critical aspects of the defects to be detected required more attention. The author further observed that. "In particular large delaminations between layers are generated by collision even at low energy due to falling tools, hail storm, flying birds or debris. This and other causes can give not only hidden delaminations but also cracks. The impact damage is usually underestimated since the projectile does not indent the surface due to low energy of impact."

Ibekwe *et al* [61] also considers BVID from a low velocity impact event as very dangerous because they cannot be detected visually and lead to structural failure at loads well below design levels. The authors revealed that "the loss of strength and stiffness of laminated composites at elevated temperatures is intensified by the increased rate of water absorption at high temperatures." They further investigated that the UV radiation alone has a significant effect on reducing the residual load carrying capacity of impact damaged laminates.

Galea *et al* [62] also confirmed that "while impact can cause a significant amount of delamination, often the only external indication is a very slight surface indentation and this type of damage is frequently referred to as barely visible impact damage (BVID)". Many other researchers [63] also, consider low-velocity impact particularly BVID as potentially dangerous, because it reduces the loading resistance and may destructively propagate. Kim J.K [64] too, confirms that, "it has been proven that, the presence of internal damage in BVID causes substantial losses in strength and stiffness of the composite components".

In order to appreciate damage due to impact in composite materials, it is necessary to understand the concept of low-velocity impact. This is thus, discussed in the next section.

3.2 Low-velocity impact

Defects due to impact in composite materials are much more complex, and less well understood than metallic ones [65]. Based on this fact, it is necessary, to know the behaviour of these materials at impact in order to quantify the defects accurately, and therefore, the understanding of failure modes which results from low velocity impacts is essential. Hancox N.L [66] defines impact as "the relatively sudden application of an impulsive force, to a limited volume of material or part of a structure". The author, however, further justifies his definition and considers the terms 'relatively' and 'limited' as being subjected to a wide range of interpretations.

Generally, impacts are categorized into either low or high velocity, but there is not a clear shift between classes and usually there is a disagreement on their definition. Sjöblom *et al*, and Shivakumar in [67], define low-velocity impact as "events which can be treated as quasi-static, the upper limit of which can vary from one to tens of ms^{-1} depending on the target stiffness, material properties and the impactor's mass and stiffness".

Olsson, R [68] recommends that, the most common way of classifying impact events is to differentiate between "high velocity" and "low velocity" impact. He therefore suggests that, even though no consensus has been established on criteria for these two categories, the upper limit of low velocity impact ranges from 10 to 100m/s. Abrate, S. [69] also considers low-velocity impacts as those which occur for impact speeds of less than 100 m /s. Other researchers in [66] suggest that the type of impact can be classed according to the damage incurred, especially if damage is the prime concern. It is, however, noted that, High velocity is characterized by penetration induced fibre breakage, and low velocity by delamination and matrix cracking.

Davies and Robinson in [70] suggests that, the term "low velocity" should be defined since high velocity produces local ballistic types of damage, far from invisible, and extremely local. The authors, hence, define low velocity as "that lower bound which does not excite through thickness stress waves but allows the material to respond dynamically so that it can deform without producing the local 3-D stress fields". The authors further observe that this velocity turns out to be about 20m/sec in CFRP if tool drop and similar accidents are considered, and that Low velocity impact damage may occur during manufacture, maintenance, or in service by accidentally dropped tools, runway debris or hailstorms.

In low-velocity impact, the dynamic structural response of the structure is extremely important as the contact duration is long enough for the entire structure to respond to the impact and therefore, more energy is absorbed elastically [71]. However, the understanding of the modes of failure in composites is important, and this is discussed in the next section.

3.3 Modes of failure in low-velocity impact

By virtual of being heterogeneous and anisotropic, the fiber reinforced plastic (FRP) laminates produces four major modes of failure. Short, G.J *et al* [72] observes that, "the main damage modes in laminates composite are, matrix cracking, fiber-matrix debonding, delaminations, and fiber fracture". Matrix damage, delamination and fibre failure/fracture are briefly discussed in the following sections.

3.3.1 Matrix damage

Matrix damage is the first type of failure induced by transverse low-velocity impact, and usually takes the form of matrix cracking but also debonding between fiber and matrix [67, 72]. Matrix cracks occur due to property mismatching between the fiber and matrix, and are usually oriented in planes parallel to the fiber direction in unidirectional layers.

Islam and Craig [73] observed that, "matrix cracking is the cracking of the resin within a layer, and that, fibers perpendicular to the loading direction produce stress concentrations in the matrix". The authors further examined that, since the failure strain of the matrix is lower than that of the fiber, when subjected to a load, the difference in failure strain causes the matrix to crack. A general picture or analysis of a typical crack and delamination pattern is shown in Figure 3.1 below.

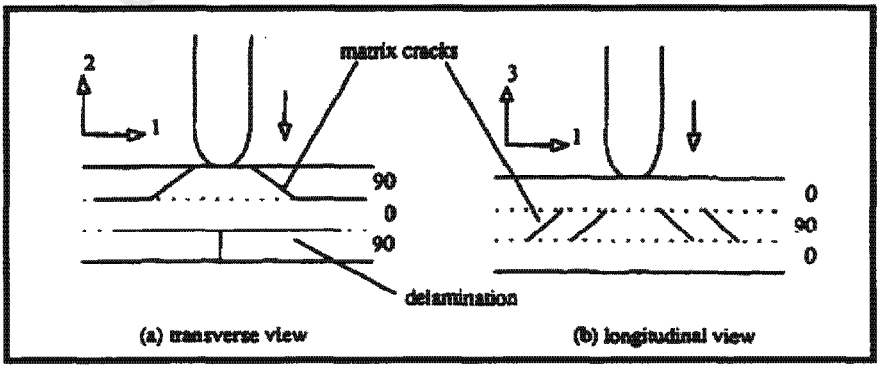

Figure 3.1: Typical crack and delamination pattern [67, 73]

The matrix cracks in the upper layers in Figure 3.1 (a) and the middle layer in Figure 3.1 (b) start under the edges of the impactor. These shear cracks are formed by the very high transverse shear stress through the material, and are inclined at approximately 45^0. There is also a relationship between transverse shear stresses, the contact force and contact area respectively. The crack on the bottom layer of Figure 3.1 (a) is referred to as a bending crack because it is brought about by high tensile bending stresses and is typically vertical.

3.3.2 Delamination mode

A delamination is a crack which can propagate in the resin-rich area between plies with different fiber orientation [67, 74]. Further studies byYen, C.F, [74] revealed that, "Delaminations which are caused by transverse impact usually come about after an energy threshold has been reached and that delamination only occurs in the presence of matrix cracks". This type of damage appears as debonding of adjoining plies in laminated composites. Stresses that lead to delamination could result from out-plane stresses such as mismatch (i.e. the different fiber orientations between the layers) in Poisson ratios between plies, which results in shear stresses near the ply interface. These shear stresses produce a bending moment that is balanced by a stress in the thickness direction. Just like in matrix cracking where the main contribution to damage occurs at the tension side, delamination is also prominent on the tension side. At very short times after impact, however, it begins on the neutral plane, where maximum shear stresses are present.

Morais *et al* [75] assessed that, the presence of delaminations may not be critical if only tensile stresses are to be of concern. The authors, however, observed that "delaminated areas will affect the flexural stiffness of laminates, and the initiation of delamination depended on laminate thickness". They further noted that, "the maximum value of shear stresses at the neutral plane of a laminate subjected to 'bending like' impact events must, in fact, be carefully taken into account, and that, laminates with an elastic mismatch due to laminate geometry, stacking sequence or materials properties can have huge delaminations due to shear stresses."

3.3.3 Fibre failure

It has been reported [67] that there is less information on this type of damage, as research has concentrated on the low-energy modes of damage. This damage mode however, usually takes place much later in the fracture process than matrix cracking and delamination. Further details in the report disclose that, fibre failure occurs under the impactor due to locally high stresses and indentation effects and that these effects are principally managed by shear forces and on the non-impacted face due to high bending stresses. It should also be mentioned that, fibre failure initiate much earlier in the service life of the laminates composite and accumulate quickly until the final failure [72].

CHAPTER 4

4 Experimental techniques

Helicopter rotor blades are important safety and highly complicated parts composed of a mixture of materials and components. Each rotor blade is fabricated as a composite, with foam or honeycomb materials forming the core of the blade, covered with one or more layers of fibre reinforced plastics on the outside. Reinforcement of these plastics is achieved by adding, Kevlar or glass fibers. Stressed areas such as the leading edge of the blade are reinforced with metallic layers to increase the strength [56]. From the NDT point of view, the complexity of this material requires NDT techniques that have a high probability of detection (POD) in terms of sensitivity, if defects or flaws in such materials can be detected and quantified.

Digital shearography and IRT are optical techniques that are able to detect defects in composites, and were used in the experiment to detect the artificially created flaws in the specimens provided. Original pieces cut from different helicopter main rotor blades, a composite material cut from an original Unmanned Aerospace Vehicle (UAV) wing, and part of the UAV wing itself were the specimens used in the experiments. These specimens were donated to the NDT optical laboratory of the University of Cape Town, in the Mechanical Engineering Department. This section therefore outlines the procedure and setup used to test the specimens for defects, using Digital shearography and IRT.

The testing was divided into five experiments: experiment number one involved the inspection of specimen number one. This specimen was part of the helicopter main rotor blade with nine artificially created flaws in it. The specimen was stressed from the far side (from the back) and was inspected from the front side where the defects could not be seen; the second experiment involved stressing the same specimen from the inspection side (front side). The third experiment involved soaking the whole specimen (helicopter main rotor blade) in the drying cabinet in order to stress it uniformly. However, in all these tests, the inspection was done from the front side. The objective of the tests was to

quantify the defects by relating the number of fringes created to the depth where the defect was located. Experiment number four involved the testing of BVID in a composite material from the UAV wing. Finally, experiment number five involved the testing of three different specimens: part of helicopter main rotor blade with three artificially created flaws and only one flaw was investigated; part of helicopter main rotor blade with nine artificially created flaws and only one flaw was investigated; the third specimen was part of the UAV wing with one artificially created BVID. In all these three specimens each flaw was stressed from the far side and the front side respectively, and each flaw was inspected six times. Thermal stressing using the regulated infrared lamp was used to stress the specimens, and the stressing times were 5 seconds, 10 seconds, and 15 seconds respectively. All the defects during the testing in experiment number five were simultaneously exposed to shearographic and IRT testing.

The general standard inspection procedures for shearography and IRT systems and equipment setup are initially discussed in the next section, and this is followed by descriptions of setups pertaining to each experiment.

4.1 Digital Shearography Setup

The equipment setup comprises the following items:

1. A continuous wave 30mW Helium-Neon (HeNe) laser with a wavelength of 632.8nm and coherence length of 100mm. A continuous wave laser is used as it is characterized by the continuous (steady-state) emission of coherent light at relatively low power.
2. A Microsoft XP personal computer (PC) with an Intel Pentium 4 processor. Custom written software is installed on the computer. The PC is also fitted with a digitizer card and an expansion card.
3. A PC monitor to view the fringe patterns.
4. Tripod stand to secure the infrared lamp
5. Test specimen in place (helicopter main rotor blade).
6. Infrared lamp to heat the specimen.

7. Beam expander to disperse the laser light so that the entire inspection area is illuminated.
8. Adjustable mirror to guide the laser through the beam expander.
9. Shearography unit with camera, mirrors and focusing unit
10. Additional laser
11. magnetic stands to provide support to the specimen
12. Vibration free optical table
13. Counter weight to balance the tripod

Figure 4.1 shows the equipment setup with the specimen in position.

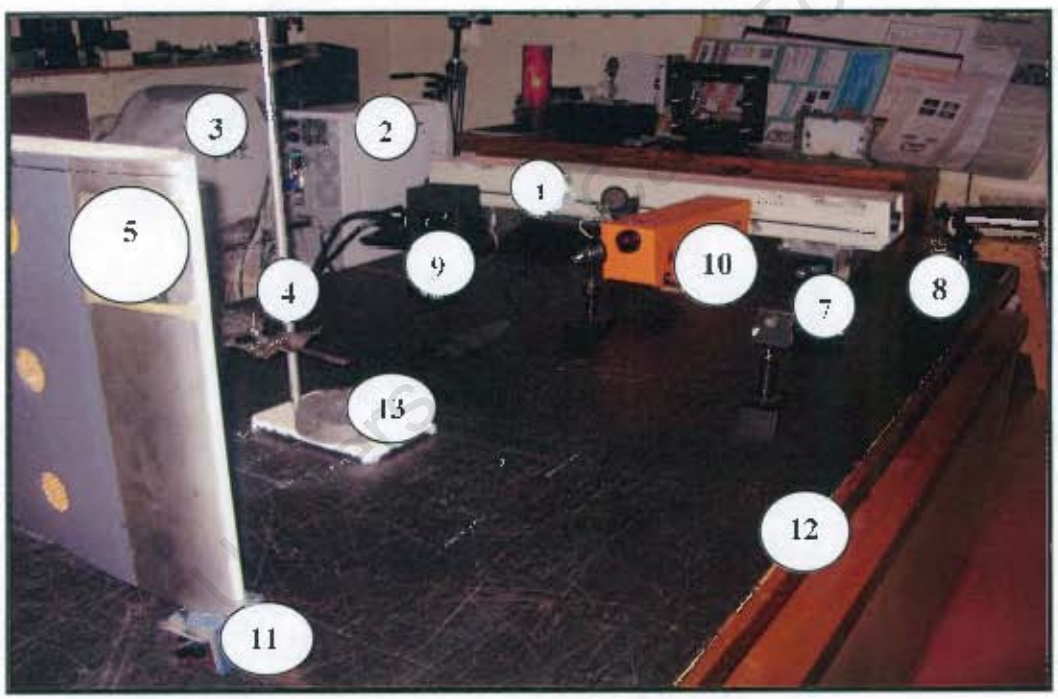

Figure 4.1: Equipment setup

Testing Environment

The experiments took place in the optical laboratory at the University of Cape Town in the Mechanical Engineering Department. The set up of the equipment was done on a vibration free optical table, although vibration isolation is not necessarily a requirement for shearography. The table's surface is a 25mm steel plate which lies on inflated rubber

tubes that rests on a solid steel base. The specimen was fixed in place as long as its stability was not compromised.

CCD Camera connections

Two CCD camera cables were used. One cable supplies power to the CCD camera from the computer. The other cable called a Camera Link cable which connects to the frame grabber or digitizer card on the computer was used to transmit data from the CCD camera to the computer. Moreover, the Camera Link cable also transmits data from the computer to the CCD camera so that the gain of camera can be controlled using Graphical User Interface (GUI) software since the camera has a built-in look-up table (LUT) for dynamic range control. This arrangement permits the user to control the contrast and brightness of the CDD camera detector directly.

PC start up and CCD camera focus

When the computer is started up, the CCD camera is also switched on because the latter is powered by the computer, and this happens simultaneously. Once the custom software is opened and loaded a Windows style interface as shown in Figure 4.2, allows the user to view the live video of the specimen being inspected. This also permits the user to focus the CCD camera by adjusting the focusing controls and zoom on the closed circuit television (CCTV) lens. The mode controls used are: Video green button to trigger video motion; video pause button; video stop button; video mode for setting up specimen at correct shear; shear mode to capture the image; phase mode; slider for brightness; viewing space for created fringes and filter button. Other controls are optional to the user.

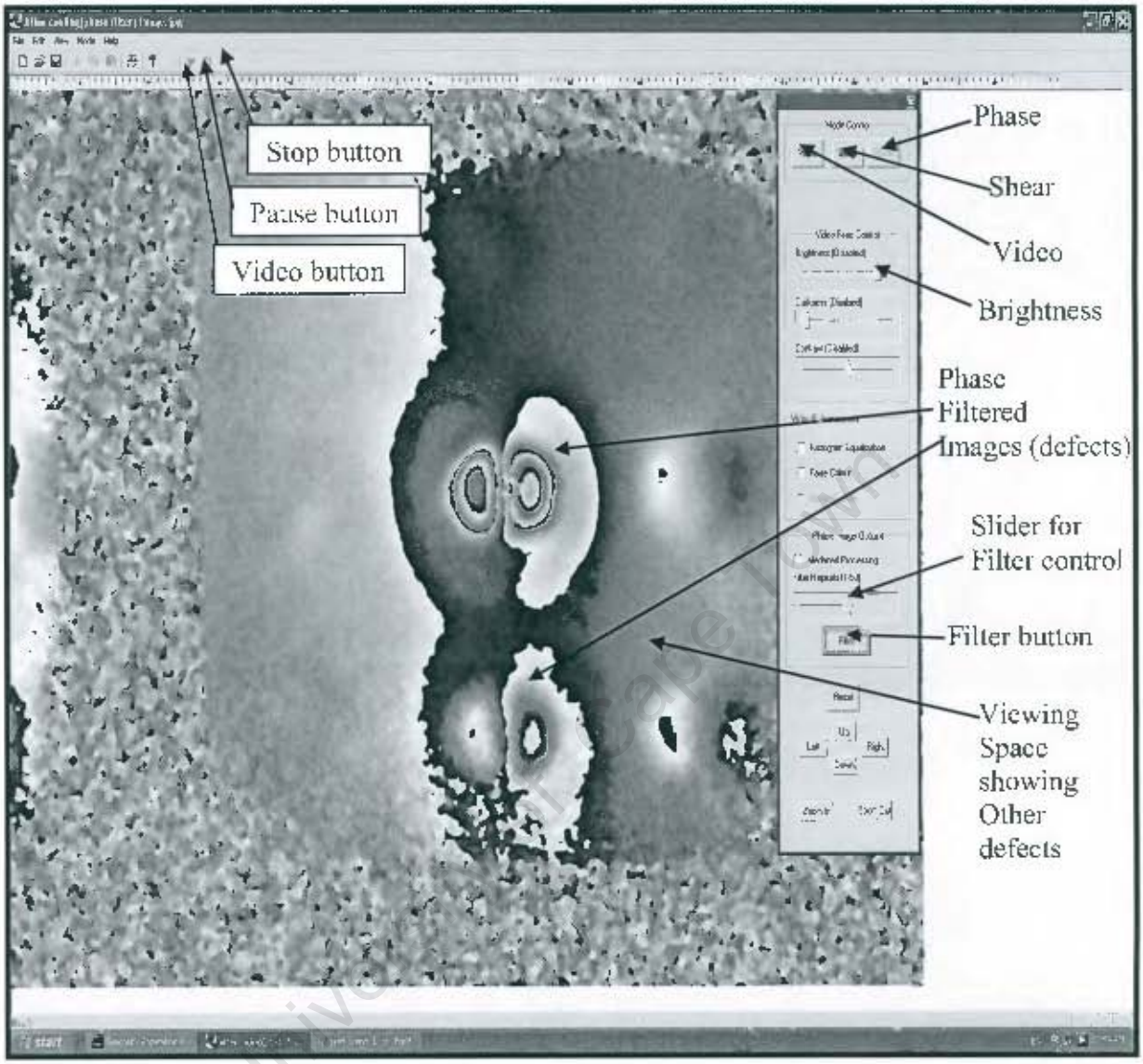

Figure 4. 2: Windows user interface

The software controls the digitizer card, the expansion card, real-time image acquisition and subtraction processes for the fringe pattern generation.

Shear Application

Shear is established once the camera is focused. This is done by adjusting the two screws on the miniature angle mount. The sensitivity of the interferometer is attained by increasing the amount of shear. This, however, results in the reduction of the maximum

area that can be inspected. Focusing the camera should be the priority because it is difficult to distinguish whether the CCD camera is focused or not when the image on the screen is sheared.

Lens adjustment

The laser is powered and the beam expander is attuned so that the laser light dispersed can illuminate the required area of the specimen under test. The viewed specimen's surface at this point will appear "grainy" due to speckle. The speckle can be made bigger or smaller by adjusting the aperture of the lens. Reducing the speckle size permits the device to detect smaller displacements. Speckle size, nevertheless, is limited by the resolution of the CCD camera and thus when the speckle reaches a certain size it can no longer be resolved. The resolution of the CCD camera is 1300 x 1030. A small test can be done by lightly pushing the finger down on the vibration isolation table to determine whether the speckle will "twinkle". If the speckle (i.e. black and white spots) appear like they are moving around when the table is depressed, then the speckle should be able to detect minimal displacements. The aperture does not only affect speckle size but it is also adjusted so that the right amount of light will enter the detector of the CCD camera. However, the amount of light and speckle work together so much that, if the speckle can be clearly seen then that is the correct amount of light.

Switching to shearography mode

The interferogram can be observed by pressing the shearography button shown on the windows interface on the right in Figure 4.2 above. Subsequent to pressing the button the software will capture or grab an image of the live video so that an "unstressed" image of the object can be stored in the computer. This image is used in the subtraction process to generate the fringe patterns.

Switching to phase-stepped shearography mode

Selection of the type of mode is optional. The user can either chose normal shearography mode or phase-stepped shearography mode. If the user wishes to use the shearography

mode, then this step will be skipped, but if the user wants to go into Phase-stepped shearography mode then the other mode will be skipped.

Getting into Phased-stepped shearography mode requires the user to press the Phased-stepped shearography button on the right side of the viewing screen on the user interface shown in Figure 4.2. Phased-stepped shearography will only work if the piezo-electric transducer (PZT) is connected to the expansion card on the computer. The software controls the (PZT) by sending a binary number to the expansion card. The binary number is converted into a voltage by a digital to analogue converter and sent to the PZT through the cable that connects it to the computer so that a calibrated micro-displacement can occur. When the button is pressed, an image of the unstressed object is stored in the computer for use in the fringe generation routines. A clicking sound will then be heard as the PZT goes through its micro-displacements.

Stressing the object

The object can be stressed by using one of the following: (1) thermal stressing (2) mechanical stressing (3) vacuum or pressure stressing and (4) vibration stressing or acoustic loading. The manner of stressing is dependent on operator's choice. During thermal stressing, heat is provided and applied by either a hairdryer or infrared lamp for the stipulated or set time. Heating the surface of the object generates a thermal wave that propagates through the material. Defects within the material will disturb the generated temperature gradient and lead to localized strains and therefore the presence of a flaw can be identified.

As soon as the object is stressed, fringe patterns will appear on the viewing screen. The computer performs the subtraction process near real-time and constantly updates the viewed video feed. This is due to the fact that the frame grabber is set on continuous grab and therefore the entire process of formation and later the degradation of the fringe patterns can be observed. The degradation of the fringe patterns can occur due to two reasons; (1) the heat supplied to the object has dissipated or (2) too much heat has been

provided which will cause the fringes to run over one another hence canceling the fringes.

Brightness and Contrast adjustments

This is an optional operation on the part of the user. It is done whilst stressing the object under inspection and when the resulting fringe patterns are viewed. This is achieved by moving the respective slider on the user interface shown in Figure 4.2, so that clear and prominent fringe patterns can be observed. The brightness and contrast slider on the user interface act independently of the Graphical User Interface (GUI) software controlling the CCD camera and changes the brightness and contrast of the video feed after being retrieved from the CCD camera.

Fringe pattern storage

Fringes are captured once an indication of further creation of fringes is observed. This is characterized by the diminishing signs of creation of the already created fringes. The next thing is to pause the live viewing of the fringe patterns by pressing the pause button on the user interface. Then the live video which is now a frozen image can be carefully scrutinized or stored for later use. Windows photo editor can be used to make further adjustments such as cropping and auto balance to improve visibility of the overall image.

Filtering stage of fringe patterns

In Phase-stepped shearography, once the fringe pattern is paused the user has the option of filtering the image by pressing the filter button on the right hand side of the interface shown in Figure 4.2. Before this is done the user can adjust the number of loops of the filter by moving the number of loops slider left or right. This prevents the image from becoming over filtered and hence causing vital information to be lost. Once the image is filtered it can also be stored for later use.

4.1.1 Preparation of the test specimen no.1: Helicopter main rotor blade

Nine artificial flaws equally spaced and with varying flaw depths were created in the specimen. A 44 mm diameter hole-saw was used to drill the specimen such that the carbon-fiber skin was removed. The honeycomb was then extracted in order to expose the flaw depth. The center distance between holes was 140 mm, and the depth of flaws were: 2 mm, 5 mm, 10 mm, 13 mm, 16 mm, 30 mm, 43 mm, 57 mm and 64 mm respectively, and these are shown in Figure 4.3 below, and flaw depths are shown in Table 4.1. It should also be mentioned that, the depth of flaw is the distance from the inspection side where the flaw cannot be seen to the surface of the honeycomb. In other words the area to be inspected is the thickness of the honeycomb left after extracting the drilled portion to create the flaw. A cross section view of the helicopter main rotor blade is also shown in Figure 4.4

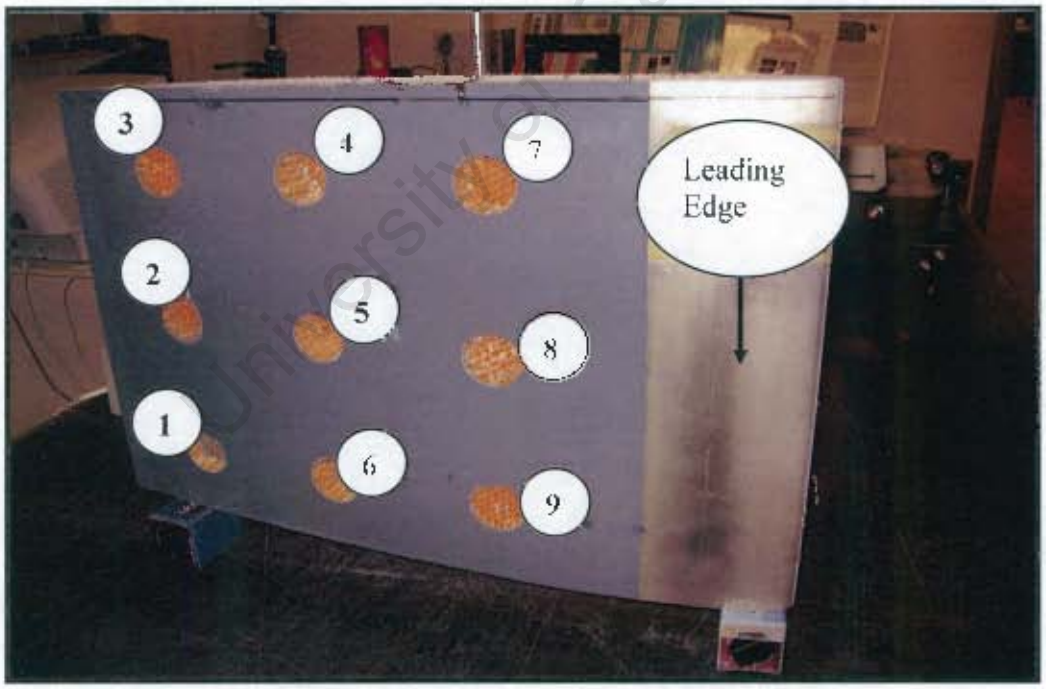

Figure 4.3: Helicopter main rotor blade with nine created flaws prepared for testing

Table 4. 1: Flaw depths

Flaw number	Diameter of flaw (mm)	Depth of flaw (mm)
1	44	2
2	44	5
3	44	10
4	44	13
5	44	16
6	44	30
7	44	43
8	44	57
9	44	64

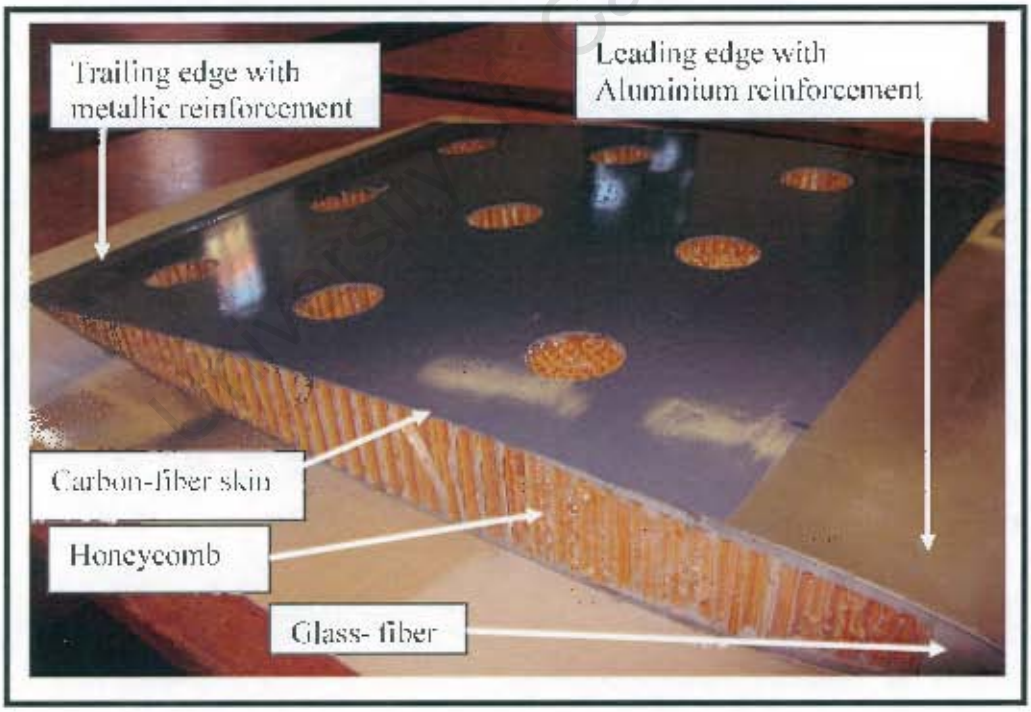

Figure 4.4: Cross section view of helicopter main rotor blade

4.1.2 Experiment no.1

4.1.2.1 Test Specimen 1: Inspection during far side heating

The specimen was positioned 235 mm away from the infrared lamp, and the lamp was secured in place by using the tripod stand. Each flaw was inspected five times and the fringe patterns were obtained after initially stressing the flaw at the far side for one second. The purpose of subjecting the flaw to more than one inspection event was to increase accuracy by averaging the number of fringes obtained. The same procedure was applied to two and three seconds stressing respectively. In all the inspections, the stress time was controlled by a regulator, designed to cut off the supply of infrared heat automatically after the preset time has elapsed. In this way the amount of heat supplied to each flaw was controlled. Figure 4.5 shows the setup during the far side heating.

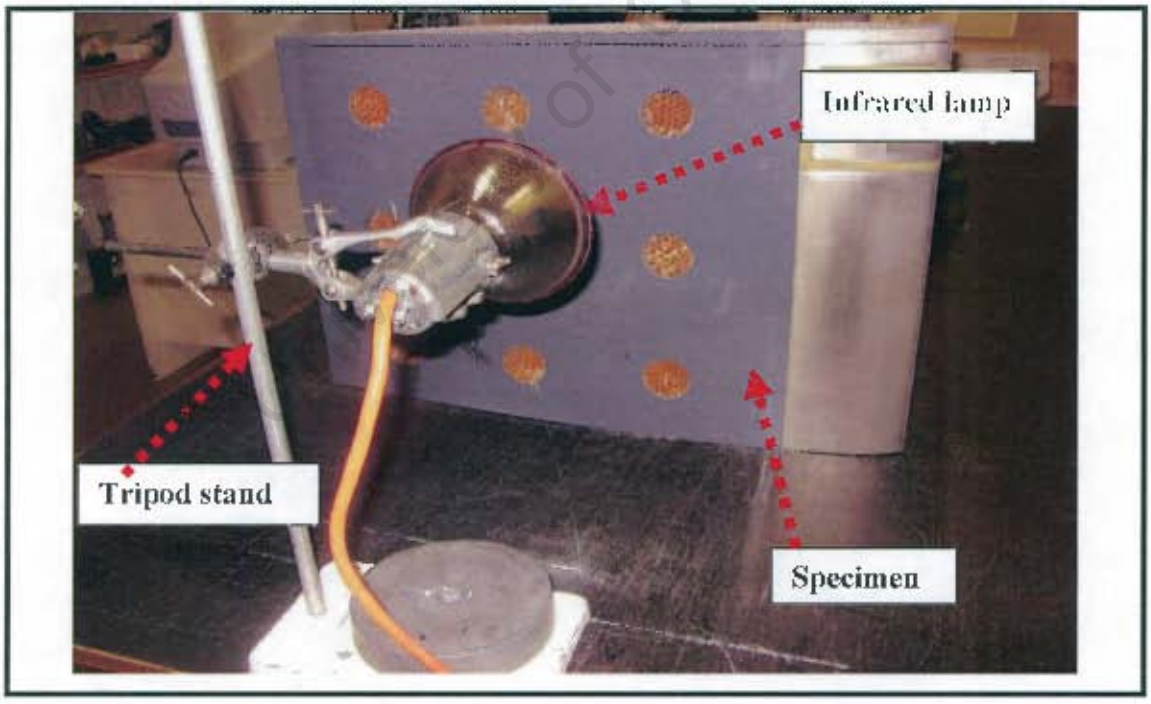

Figure 4.5: Experiment no. 1 test specimen set up

4.1.3 Experiment no.2

4.1.3.1 Test specimen 1: Inspection during front heating

In order to quantify the defects during front heating, it was imperative to make some adjustments in the setup of the equipment. In view of this, the infrared lamp was positioned very close to the specimen at a distance of 65 mm away from the inspection surface, and the stress time was set to 5 seconds this time. Only four different flaws were chosen for this test, and in order to increase the accuracy in the number of fringes obtained, each flaw was inspected eight times, and the time taken to create the fringe patterns for each flaw was recorded. Consequently the average time to generate the fringes for each flaw was recorded. The tripod stand was also adjusted for each flaw in order to accurately align the infrared lamp with the flaw position. Alignment of the flaw with the lamp was critical so that the desired amount of heat was received by the flaw. Figure 4.6 shows the setup for experiment no.2.

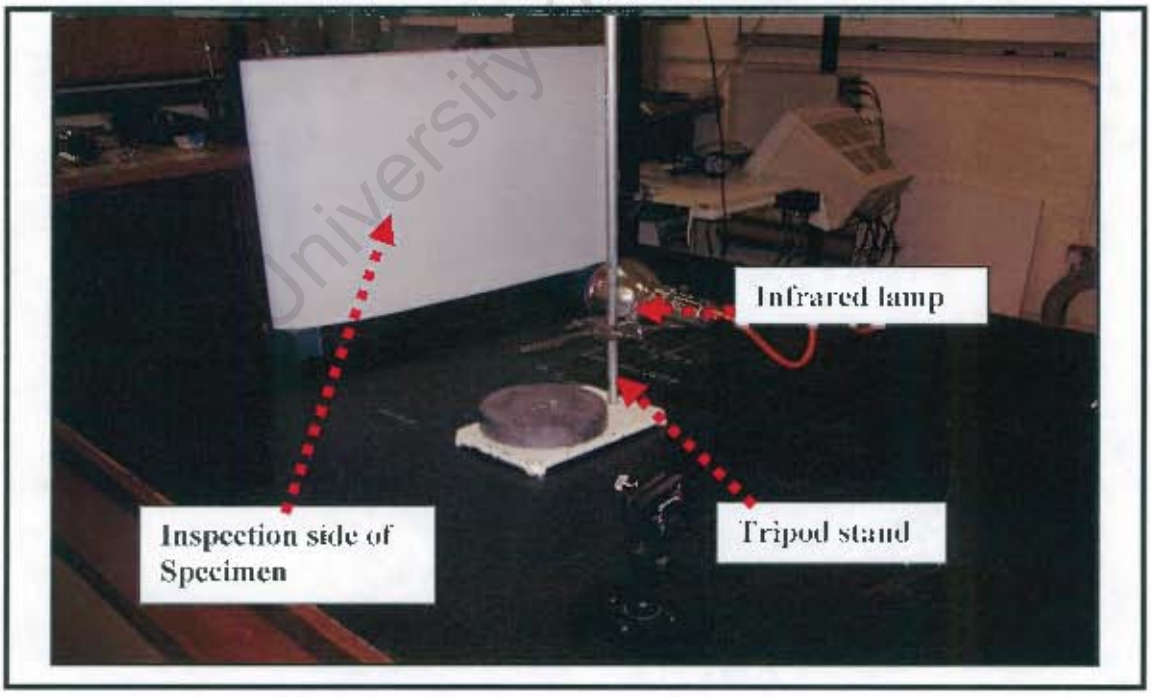

Figure 4.6: Experiment no.2 test specimen setup

4.1.4 Experiment no.3

4.1.4.1 Test specimen 1: Uniform stressing

The objective of this test was to view all the flaws in a single video show, in order to capture and compare the fringe patterns to the flaw depths. The specimen was positioned in a heating cabinet and left to soak in the heat for one hour, at a temperature of 45^{0}C. The ambient temperature at the time was 22^{0}C. It was later placed on the optical table for testing after one hour of soaking. All the setup requirements to fulfill the objective were done, and as part of the requirements, the specimen was adequately illuminated by using two lasers. Figure 4.7, is a demonstration of the specimen positioned in the heating cabinet with the thermometer for recording the specimen temperature in place. Different images were then captured and stored by the CCD camera and the digitizer in the PC. Figure 4.8, shows the specimen positioned at the table ready for testing.

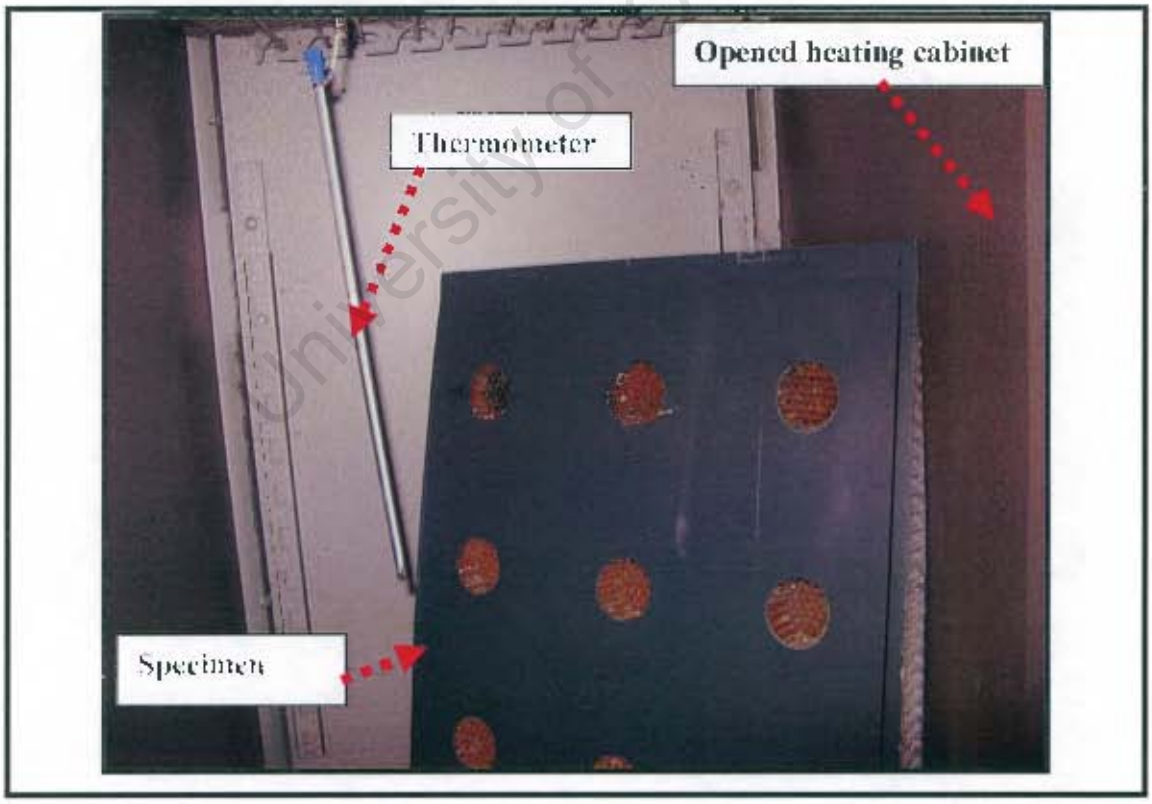

Figure 4.7: Experiment no.3, Specimen positioned in the heating cabinet

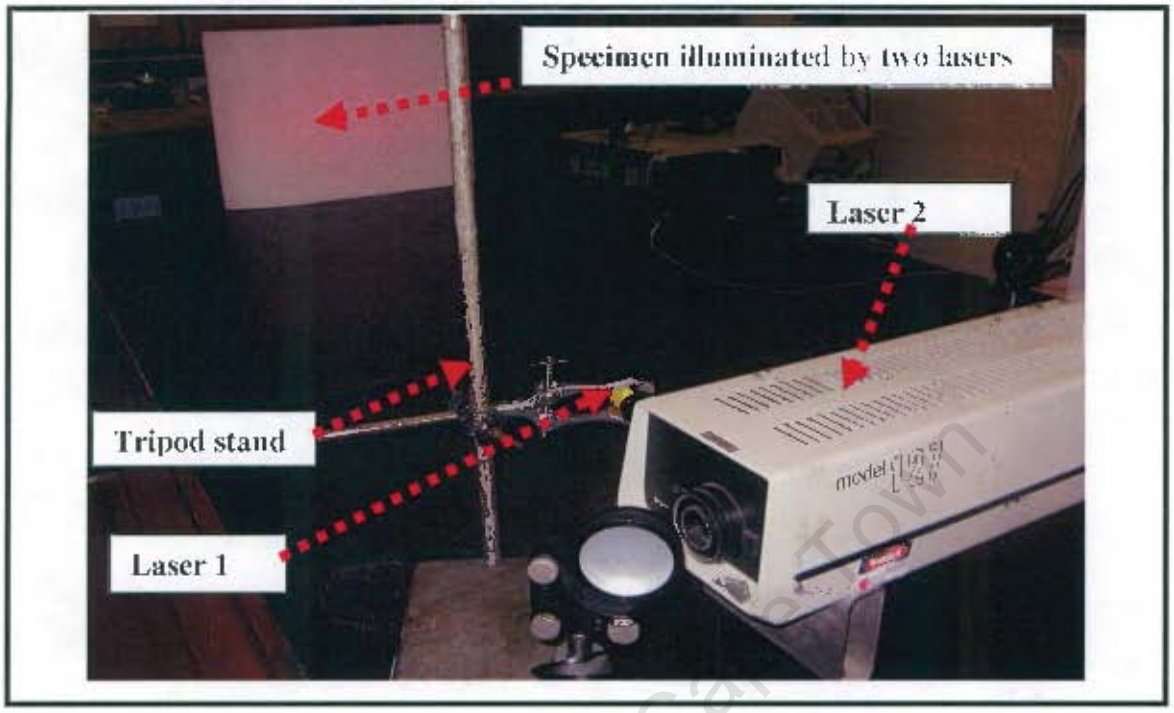

Figure 4. 8: Specimen illuminated by two lasers

4.1.5 Experiment no.4

4.1.5.1 Impact damage testing of UAV composite material

The main objective of this test was to detect Barely Visible Impacted Damage (BVID) in the composite material using digital shearography. This was to be achieved by creating artificial defects of different magnitude in the specimen using the impactor. The impact events were controlled to low magnitude so that the specimen was not penetrated and only internal or barely visible damage was introduced. In order to achieve different levels of damage, impact heights were varied initially from 180 mm to 100 mm for the first specimen. In the second specimen five BVID were created and the impact heights varied over the range 260-60 mm. After impact, the specimens were immediately inspected using shearography and, the fringes created were captured at intervals during the "recovery" process.

In shearographic testing, the amount of deformation or strain around the defect has a relationship with the number or density of fringes created, and consequently quantification becomes evident. Therefore, for the purpose of quantification, the fringe patterns created in two defects for the first specimen were observed five times at an interval of thirty minutes of cooling down, and the number of fringes created for each defect was monitored during the cooling process. The images were captured in phase mode and the time to capture these fringes was recorded. For the second specimen with five created defects, the initial pictures showing fringes were captured and the specimen was left to relax for approximately 15 hours before subjecting it to further inspection.

The specimen (panel) used for testing, was cut from part of the original wing of an Unmanned Aerospace Vehicle (UAV). The wing was donated to the University of Cape Town, NDT optical laboratory. The panel consisted of two fiber glass skins sandwiching a honeycomb, with overall dimensions of 304 x 100 x 7 mm, and this was secured firmly into a fixture prior to testing. Figure 4.9 shows part of the original wing from which the specimen was cut. The setup of the experiment before impact is also shown in Figure 4.10. Figure 4.11 shows the setup used to create impact damage in the specimen.

Figure 4.11 below, shows a steel rule (1) magnetized at arrow position (2) to the base plate (3) and vertically positioned to measure the heights from which impact damage was to be initiated. The impactor (4) was held in position to coincide with the marked or circled area on top of the specimen (5).The impactor was hemispherical, 20 mm in diameter and weighed 0.065 kg. It was allowed to fall freely on the specimen and the defects were created accordingly. Precautions were also taken to ensure that the specimen was held firmly while releasing the impactor. The motion of the impactor was achieved by means of the gearing system (not shown in the figure).BVID were created and the specimen was ready for inspection.

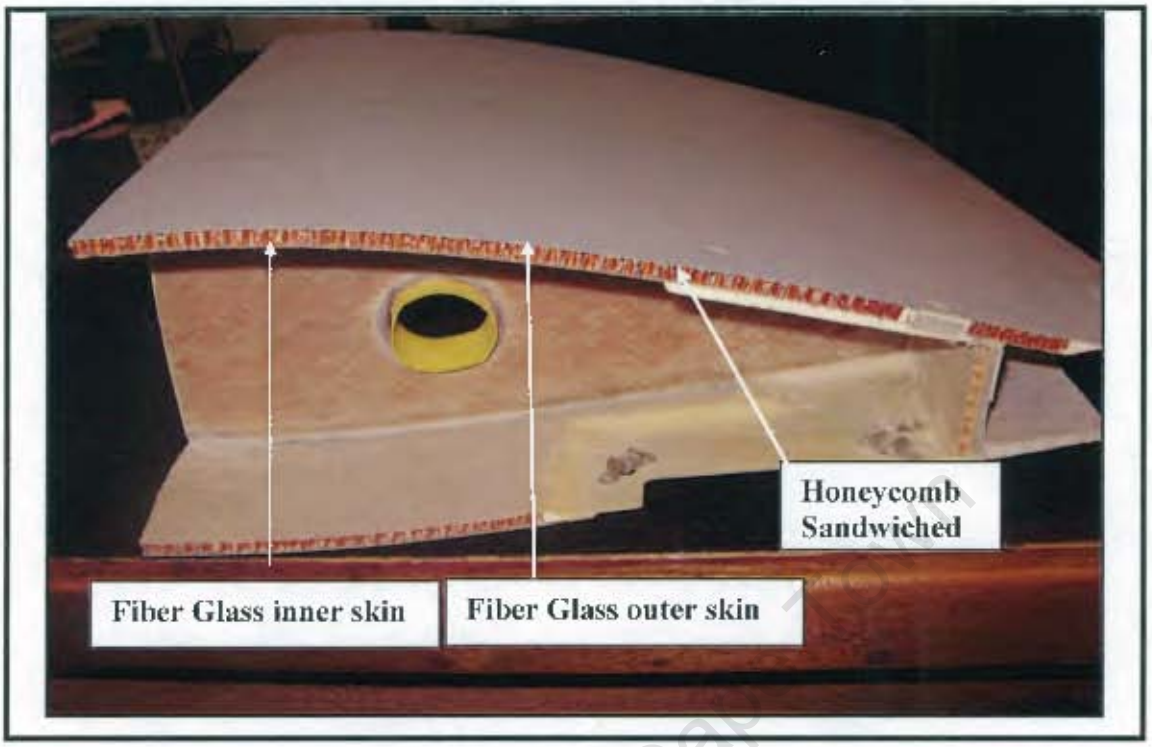

Figure 4.9: Part of original UAV wing from which the specimen was cut

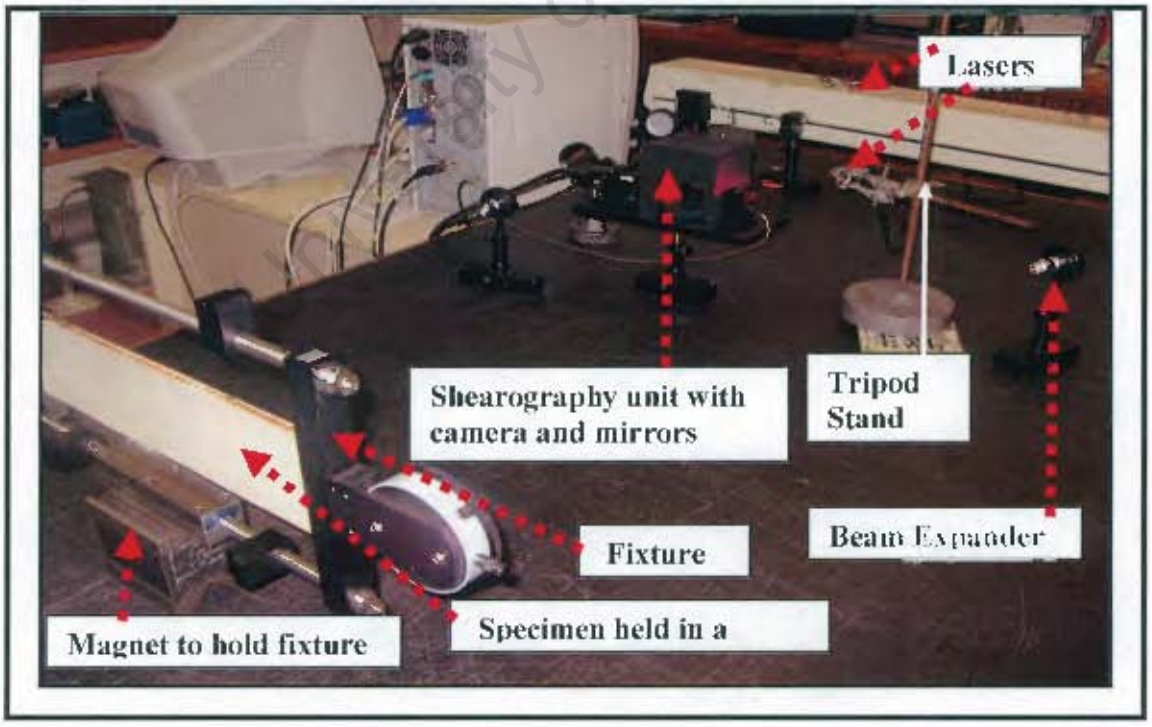

Figure 4.10: Experiment no.4 setup of the equipment

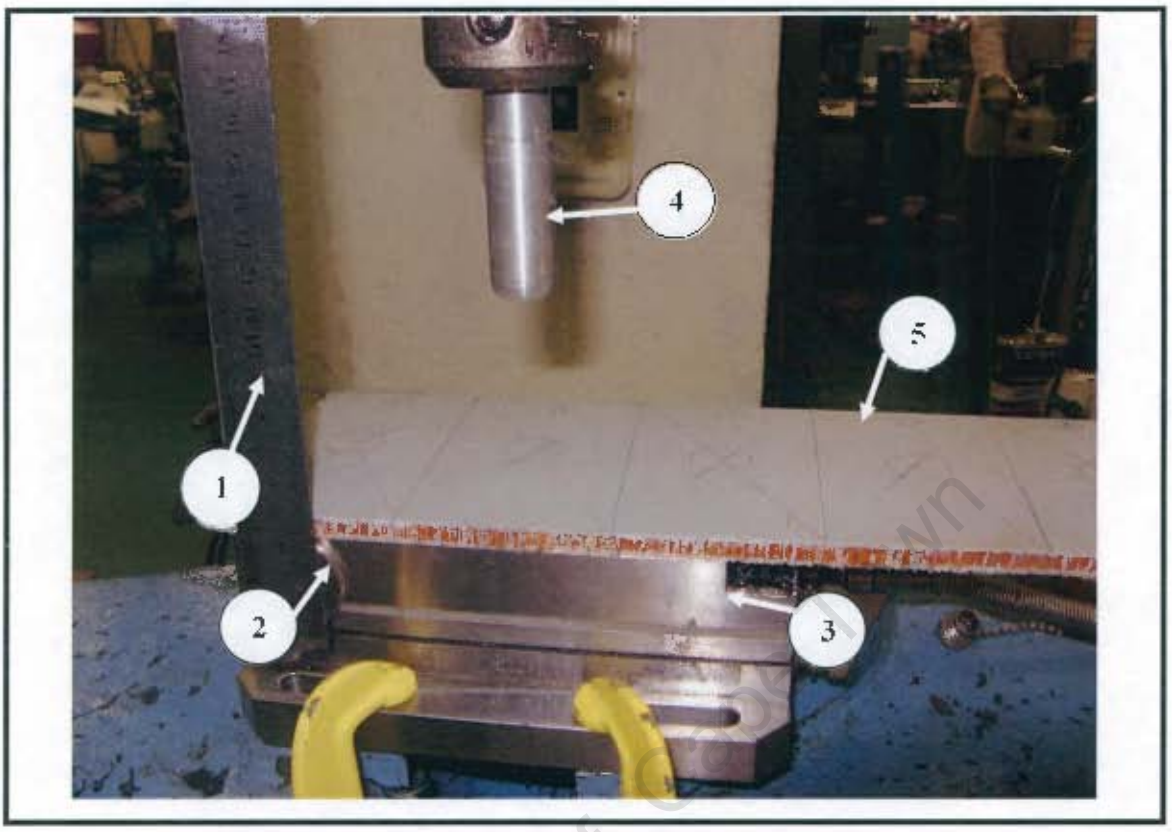

Figure 4.11: Experiment no.4 Set up to create impact

4.2 Experiment no.5: IRT and Shearographic testing

4.2.1 Background of IRT

In this experiment the IRISYS IRI -1011 Thermal Imager was used simultaneously with shearographic system during the testing of the following specimens: part of helicopter main rotor blade with three artificially created flaws and only one flaw was investigated; part of helicopter main rotor blade with nine artificially created flaws and only one flaw was investigated; the third specimen was part of the UAV wing with one artificially created BVID. IRISYS IRI Thermal Imager 1011 has so far been considered a modern thermal imager product, and is currently popular among professional users including the military. It is handy and very similar in size to a digital still camera. This imager incorporates devices such as: detector, drive electronics, optical modulator, laser pointer and four standard or rechargeable batteries [76]. Power can also be supplied from an

external DC supply. The system includes an optional pistol grip handle (not shown in the figure) which holds the 'Pocket PC' as a combined processing, display unit and image storage device. As an option, the output of the imager can be shown and processed in real time using a PC, and temperatures can be precisely measured. Figure 4.12 shows the picture of the IRISYS IRI 1011. Details of the equipment are presented in subsequent sections.

Figure 4.12: IRISYS IRI -1011 Thermal Imager [76]

4.2.2 An overview of IRISYS IRI -1011 operation

It has been reported that, the IRISYS IRI -1011 Thermal Imager has been developed from the successful IRISYS IRI 1001 hand held industrial thermal imager, using the well-proven IRISYS proprietary infrared array based detector (ABD) system. The technology used is comparable to the single-element passive infrared (PIR) detectors used in everyday security, alarm and motion sensing systems. It has an integrated circuit mounted

ceramic detector which generates a 256 pixel real-time temperature display, and this eliminates completely the need for sophisticated and costly cryogenic cooling [77]. An optical system projects the external scene on to the detector array, enabling the temperature at each of the 256 pixels to be accurately measured at a rate of eight times every second, over a range from -10 to +300C, over a 20 degree field of view, with a sensitivity of 0.5K at 30C.

An option to display the thermal images can be made to either use Grey scale, Red-blue or Green-blue color. In this experiment the Red-blue color option was used. Two moveable temperature measurement cursors are also available to evaluate the temperature anywhere in the thermal image. Both individual and temperature difference values are displayed and over one thousand (1000) images can be saved to the pocket PC for retrieval or downloading to a PC [77].

4.2.3 Components of the IRI 1011 Thermal Imager

The successful operation of the IRI 1011 Thermal Imager depends on the following components: the hardware, using the laser pointer, using the IRI 1011 Thermal Imager with a "Pocket PC', and using PC Software-IRISYS 1011 Imager. These components are discussed in the following section.

Hardware

The IRI 1011 system is designed for use with a 'Pocket PC' and the imager is connected through an RS232 serial sync cable. The IRI 1011 has an 'on/off' switch, while the 'Pocket PC' has a separate power switch.

Using the Laser Pointer

This feature is used to allow the operator to illuminate and identify the centre of the scene that the Thermal Imager is viewing. When the IRI 1011 unit is switched 'ON', the laser button can be pressed to view the position of the scene under investigation.

The illumination of the area of interest to be viewed is usually by default temperature measurement pixel. The later is the central point on the 'Pocket PC' which is indicated by a red circle. Figure 4.13 shows a screenshot of IRISYS 1011 Imager 'Pocket PC' and some other important features of a 'Pocket PC'.

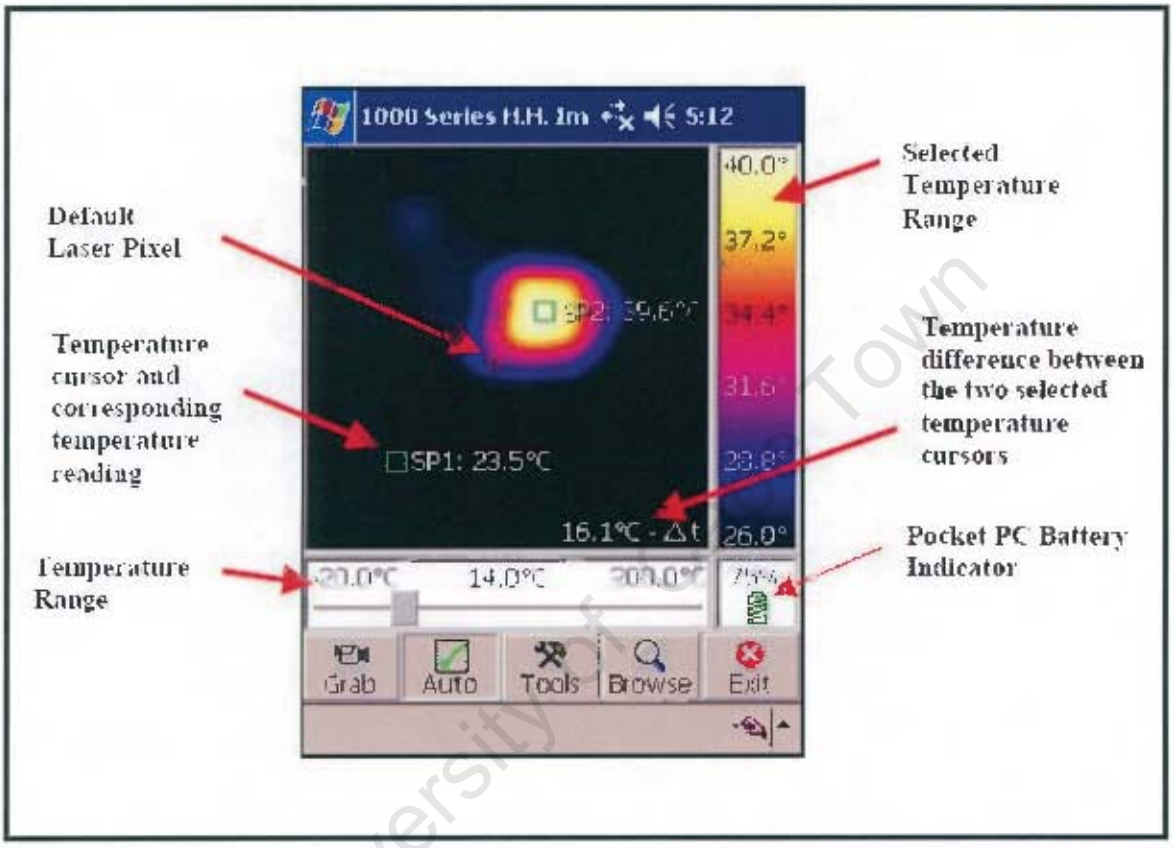

Figure 4. 13: Screenshot of IRISYS 1011 Imager 'Pocket PC' Software [78]

An indication of the pixel dimension is given by the length of the laser bar, and in order for the IRISYS 1011 to provide a precise temperature reading, the minimum area of the picture being viewed must be a square that totally surround the laser bar. This therefore makes the laser pointer useful for achieving the maximum viewing range of the IRISYS 1011in specific applications.

Using the IRISYS 1011 Thermal Imager with a 'Pocket PC'

In this experiment, the IRISYS 1011 Thermal Imager was used with the 'Pocket PC' and was run on Microsoft 'Pocket PC' 2002. The 'Pocket PC' was used to display, process

and store snapshots of thermal images. In order to display the snapshots from the 'Pocket PC' onto the PC, ActiveSync was installed on the PC and communicating with the 'Pocket PC'.

4.2.4 Software Button Operations

This section discusses some important software buttons used within the IRISYS 1011 Imager software. The discussion is with reference to Figure 4.13 above.

Grab

This button takes a snapshot of the currently displayed image. The user decides whether to save the image or not. Choosing 'No' implies that the snapshot taken has to be discarded and hence prompting the user to return to live mode. If an image has to be saved, then the option has to be 'Yes' and the image is thus stored for future use.

Auto

This button operates in two modes: "ticked box" Continuous Auto, and Unticked box" continuous Auto, In "ticked box" Continuous Auto mode, the temperature range and sensitivity of the image for ease of viewing is continuously adjusted, where as in Unticked box" continuous Auto mode the 'Auto' button can be used to switch continuous Auto on or off. In the 'Unticked box" continuous Auto, the 'Auto' button is used in a one shot mode i.e. each time the button is pushed it will automatically adjust the temperature range and sensitivity for the present scene.

Tools

This feature provides access to the following: image label, where the user can enter their own selected name for saved snapshot; image folder where the user can set the path directory to which snapshot images are saved; ambient (^{0}C), where the user can set the ambient temperature and the software compensates for this to give more accurate temperature readings. This is, however, limited to 200^{0}C. Calibration is yet another setting, and if there is more than one calibration file available for the imager, the user can

select the appropriate file from this box. For one calibration file, this selection box may not be displayed; setting the correct emissivity for the material being imaged is important to achieve the accuracy of temperature readings. Hence emissivity is another image label found in the tool's button. The number of image frames to be integrated can be set to 'Integration OFF' or up to 10 frames using the integration label. This function reduces "noise" on the image and it is turned off when imaging a moving scene. Other features in the tools button are 'interpolate', '2nd Element' and 'continuous Auto' details of which can be found in the user manual.

4.2.5 Snapshot transfer from a 'Pocket PC' to a PC

Microsoft ActiveSync must be installed to be able to transfer Snapshot images from the 'Pocket PC' to a PC. From the file menu in ActiveSync "Explore" is selected and this opens a "Mobile Device" window. A double click is made on "My Pocket PC' and then a 'double click' is made finally on "My Documents" and eventually the Snapshots are selected. The Snapshots are then copied to a suitable folder on the PC for future use.

4.2.6 Experiment no.5: testing procedure

This section describes the experimental procedure used during the testing of the following specimens: part of helicopter main rotor blade with three artificially created flaws and only one flaw was investigated; part of helicopter main rotor blade with nine artificially created flaws and only one flaw was investigated; the third specimen was part of the UAV wing with one artificially created BVID. Digital Shearographic and IRT techniques were simultaneously used in the testing of the specimens. The shearographic system was positioned on the laboratory's optical table facing the test specimen and connected to the personal computer. The IRISYS IRI 1011 system was mounted on the tripod stand with the camera also facing the specimen as for example figure 4.15. The laser pointer from the IRISYS IRI 1011 system camera was used to locate the IRT camera viewing the exact surface position where the flaw existed beneath it.

The testing procedure for each flaw in the specimens was done sequentially; the first sequence involved capturing the first image (i.e. a reference image for the Shearographic system) when the specimen was at room temperature conditions. The specimen was heated and both images i.e. (The IRT and shearographic) were stored while displaying the typical hot spot and bull's eye respectively and both indicating the presence of the flaw. Because the intention of this test was to establish a comparison of "sensitivity" of the two systems, the specimens had to be left to return to room temperature. This was dictated by the fact that when storing the initial shearographic image it cancelled the reference image. Therefore the procedure had to be repeated and the specimens were allowed to cool down to room temperature again under observation, for the evidence of which system continued to display the presence of the defect while the other no longer indicated it.

Each specimen was thermally stressed from the back and front side for a specific time, and each flaw was inspected six times. The stress times used were; 5 seconds, 10 seconds, and 15 seconds respectively. Typical arrangements of the specimen used in the experiment are shown from Figure 4.14 to Figure 4.16. Figure 4.14 for example is the setup for a UAV specimen containing the BVID defect. The results of the tests are presented in chapter five of the thesis.

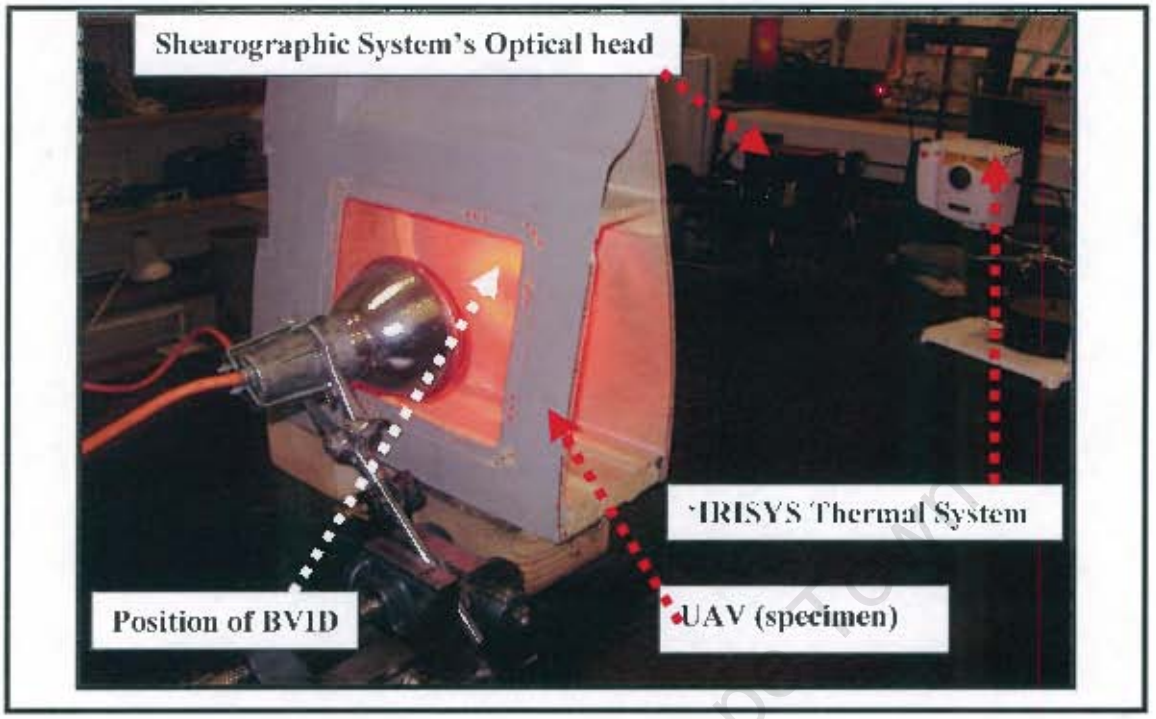

Figure 4. 14: UAV specimen containing the BVID defect

Figure 4.15 below shows the setup of the helicopter main rotor blade with three artificially created flaws and the middle flaw as shown in the figure was investigated. The figure shows the specimen positioned for far side heating.

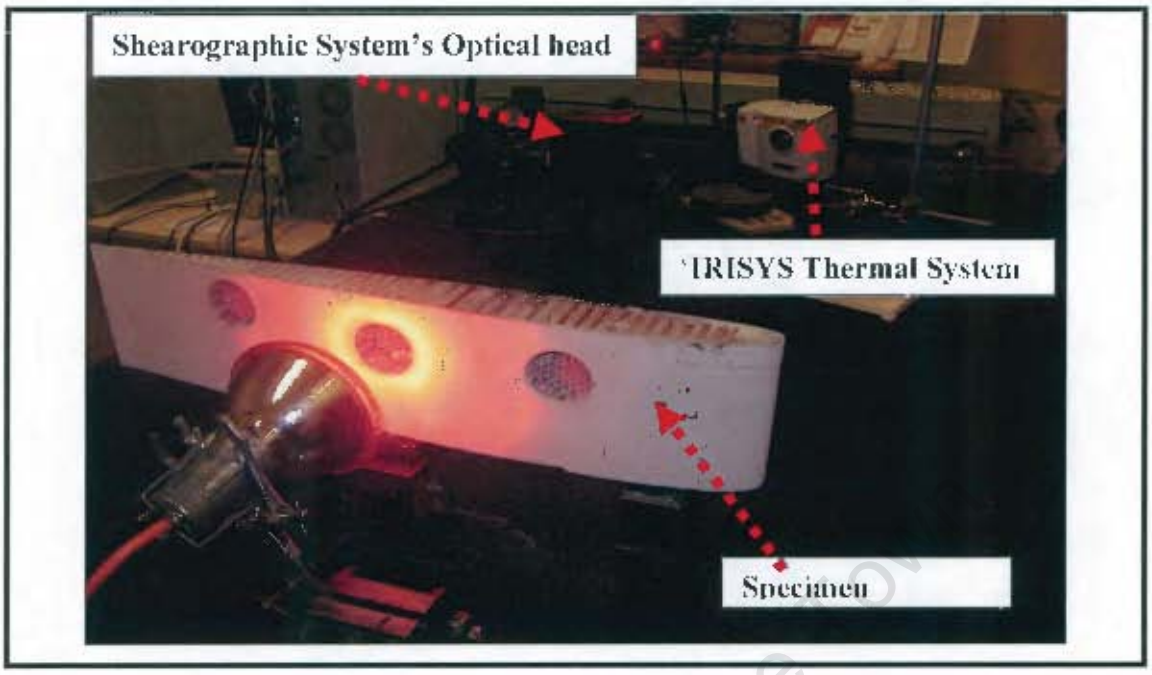

Figure 4.15: Helicopter main rotor blade with three artificially created flaws

Figure 4.16 below shows the setup of the helicopter main rotor blade with nine artificially created flaws and the flaw investigated is shown in the figure.

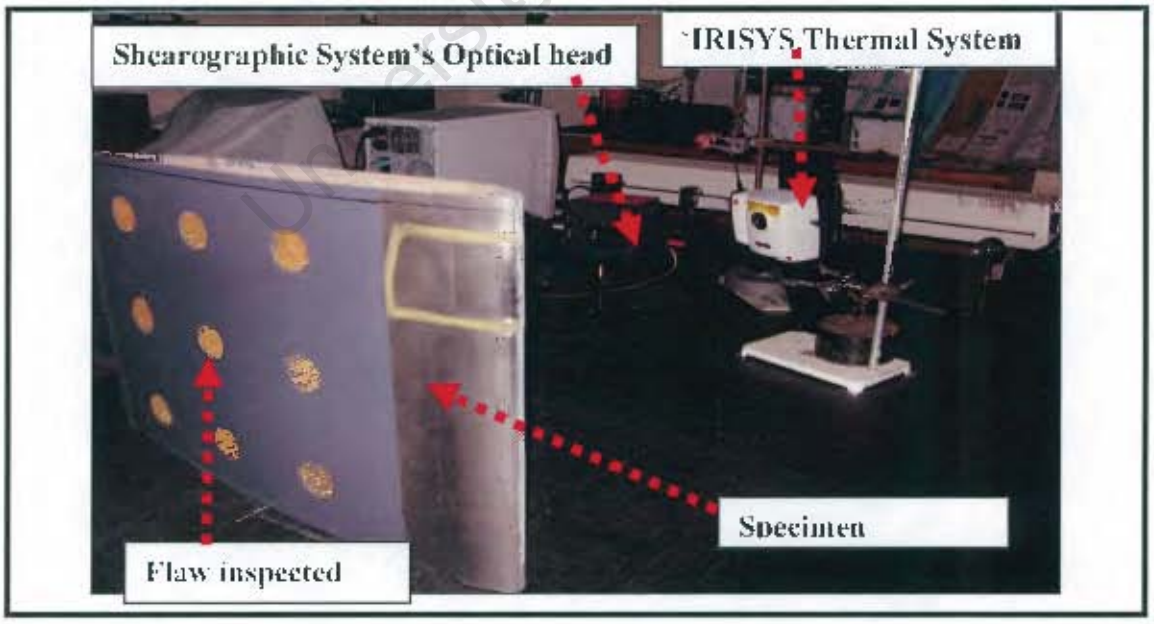

Figure 4. 16: Helicopter main rotor blade with nine artificially created flaws

CHAPTER 5

5 Results and analysis

5.1 Digital Shearographic test results

5.1.1 Experiment no.1 test results: test specimen no. 1

Specimen 1, with defects at various depths from the inspecting surface, was tested using digital shearography. The software was set to real-time mode so that the response of the specimen to stressing could be observed almost instantaneously. The tests were carried out using horizontal shear. In other words shearing was along the x-axis. The results are presented and analyzed in subsequent sections.

5.1.1.1 Test specimen no. 1 thermally stressed at the far side for one second

The seven fringe patterns shown in Figure 5.1(a)-(g), are typical results obtained whilst inspecting the defects from the near surface of the specimen, where the defects could not be seen. Each flaw was inspected five times and the patterns were obtained after thermally stressing the flaw at the far side for one second. The purpose of subjecting the flaw to more than one inspection event was to increase accuracy by averaging the maximum number of fringes obtained before they began to disappear again due to the cooling of the specimens. The same procedure was applied to two and three seconds thermal stressing respectively.

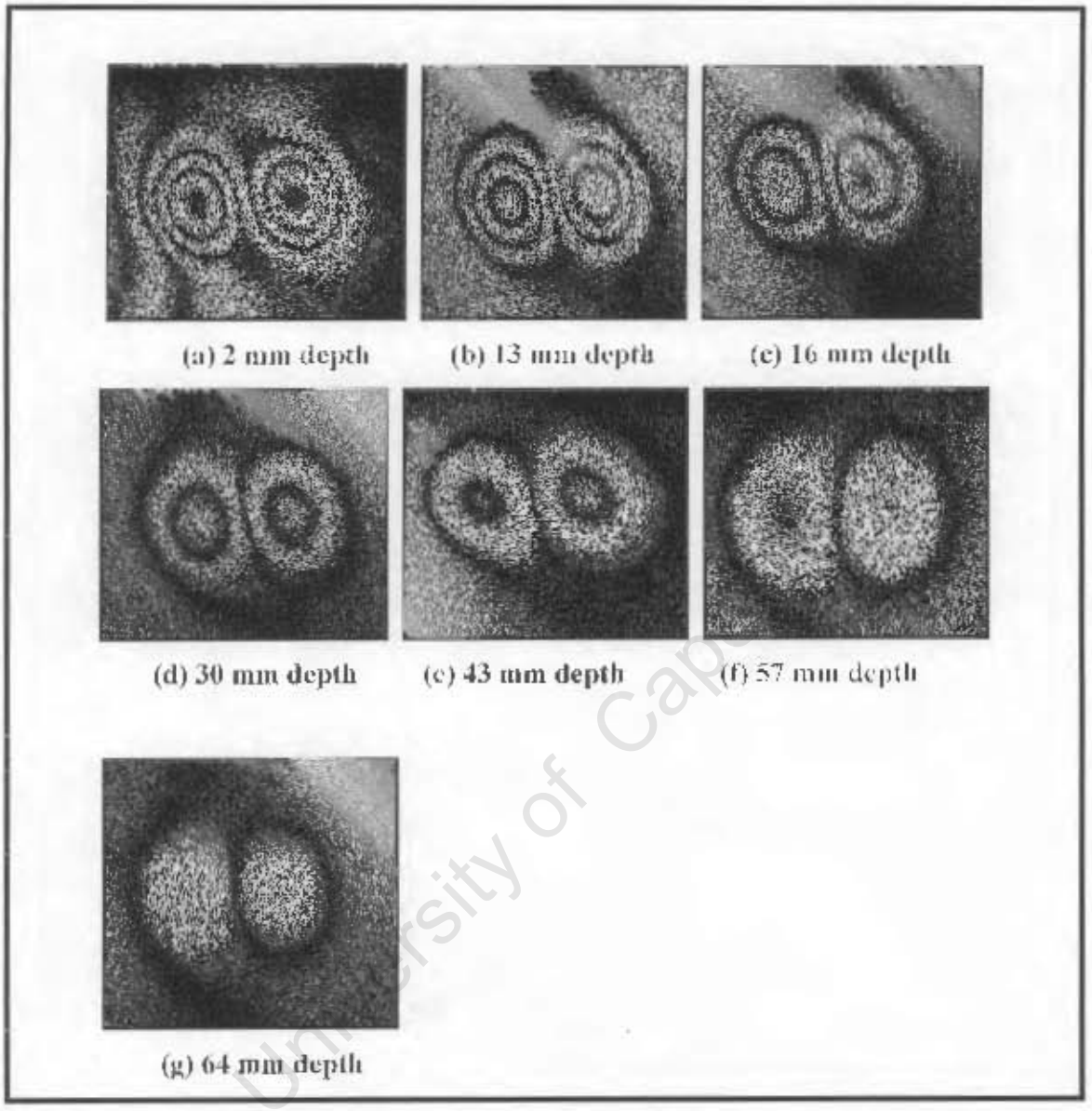

Figure 5.1: (a)-(g); Averaged fringe patterns for 1 second stress

The presence and location of the defects are clearly identified by the familiar "double bull's eye". The number of fringes around a defect usually indicates the amplitude of the localized displacement induced, and this is influenced by the depth and size of the defect. However, the basis for comparison of depth or size of defects depends on whether the defects are perturbed uniformly for the same time. It can be observed that the patterns are characterized either by an increased or reduced number of fringes, as an indication of the presence and location of the defect, relative to its closeness to the inspected surface.

5.1.1.2 Specimen no.1 thermally stressed at the far side for 2 seconds

Figure 5.2 (a)-(g) shows the averaged fringe patterns obtained after stressing the specimen for two seconds. It should be observed that, the number of fringes increased for each flaw as compared to a one second stress inspection. This also suggests that the more stress you apply to the specimen, the more fringes you expect.

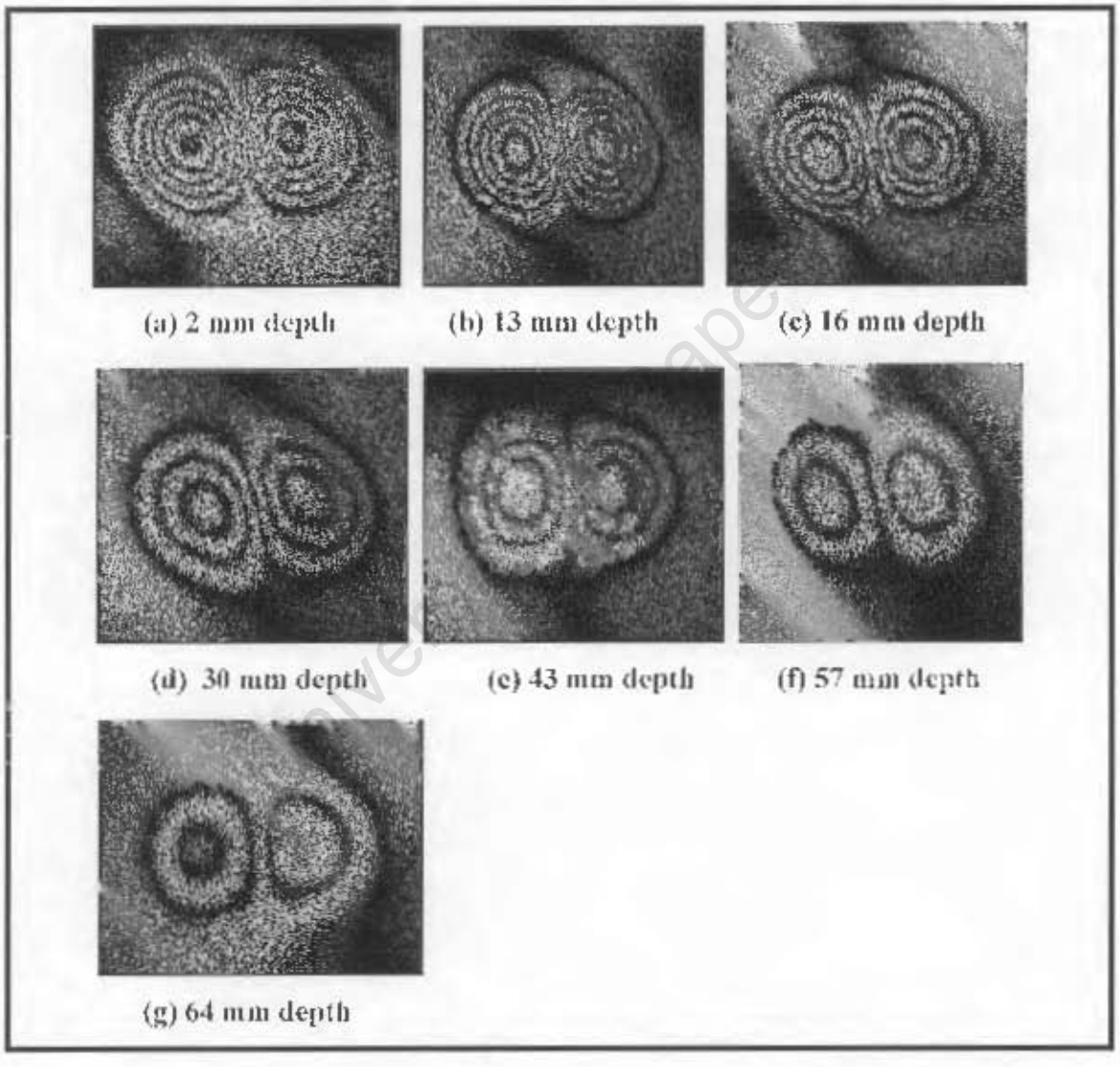

Figure 5.2: (a)-(g): Averaged fringe patterns for 2 seconds stress

5.1.1.3 Specimen no.1 thermally stressed at the far side for 3 seconds

Figure 5.3 (a)-(g), shows the averaged fringe patterns obtained after stressing the specimen for three seconds.

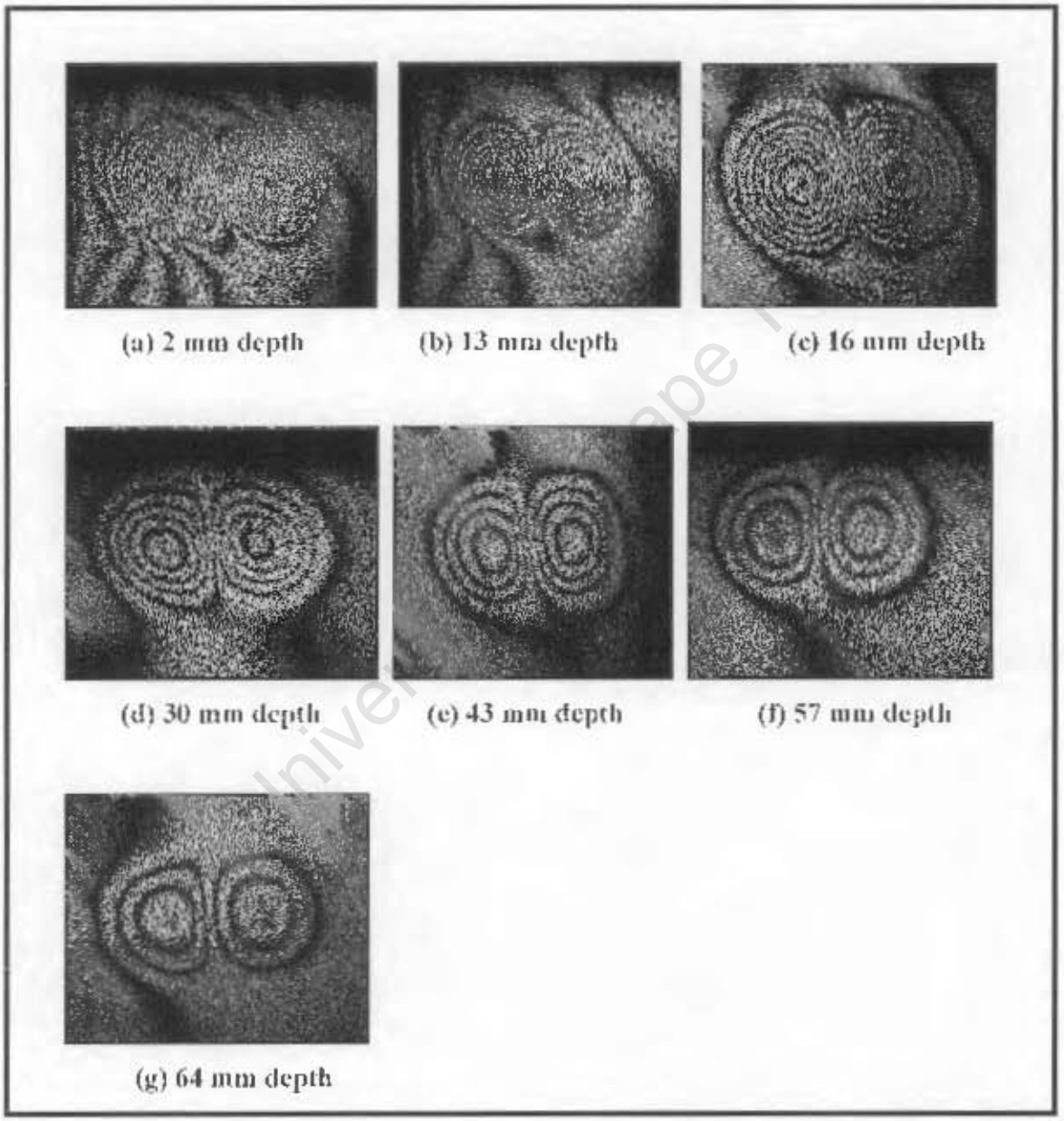

Figure 5.3: (a)-(g): Averaged fringe patterns for 3 seconds stress

5.1.1.4 Data collected and graphical presentation of inspection

Table 5.1, shows the data collected for the average number of fringes and the corresponding depths for each flaw. The results are represented in graphical form as depicted in Figure 5.4.

Table 5.1: Number of fringes as a function of depth of defect

Depth of defect (mm)	Fringes in 1 second of stress	Fringes in 2 seconds of stress	Fringes in 3 seconds of stress
2	4	6.5	9.5
13	3	5	8
16	2.6	4.5	7.5
30	2	3.5	5
43	1.75	3	4
57	1.5	2.5	3.5
64	1	1.8	3

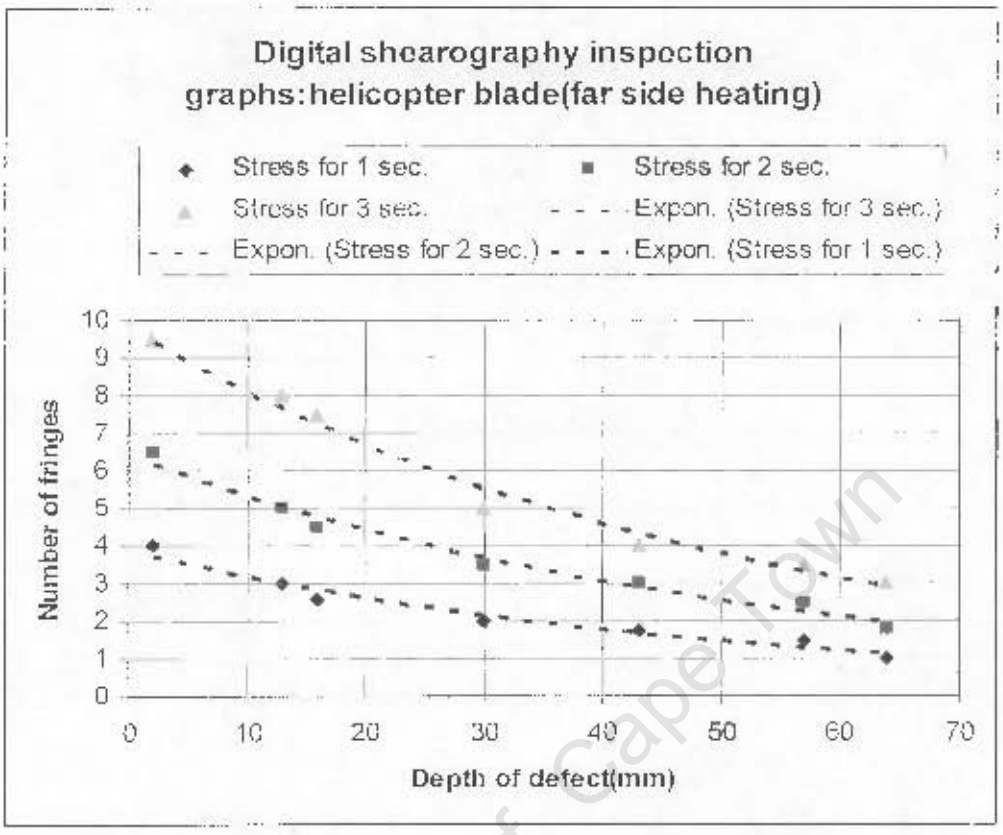

Figure 5.4: Number of fringes as a function of depth

5.1.2 Experiment no.2: Specimen no. 1 thermally stressed from front side

In order to quantify the defects in the selected flaws in the specimen, there was need to capture a predetermined number of fringes for each flaw and thus a different testing procedure was used. This time the infrared lamp was positioned 65 mm away from the front surface of the specimen. Four flaws of different depths were chosen from the specimen for analysis, and each was stressed for 5 seconds and inspected eight times. Again the number of inspections done on each flaw was to enhance the accuracy in the number of fringes obtained, and hence an average time for all the eight tests was noted for each flaw. As usual, the inspection was done from the near surface where the flaws could not be seen. It must be mentioned that the average time indicated is the time it took to capture the predetermined number of fringes per flaw. The four fringe patterns shown in Figure 5.5 (a)-(d), are typical results obtained for this inspection.

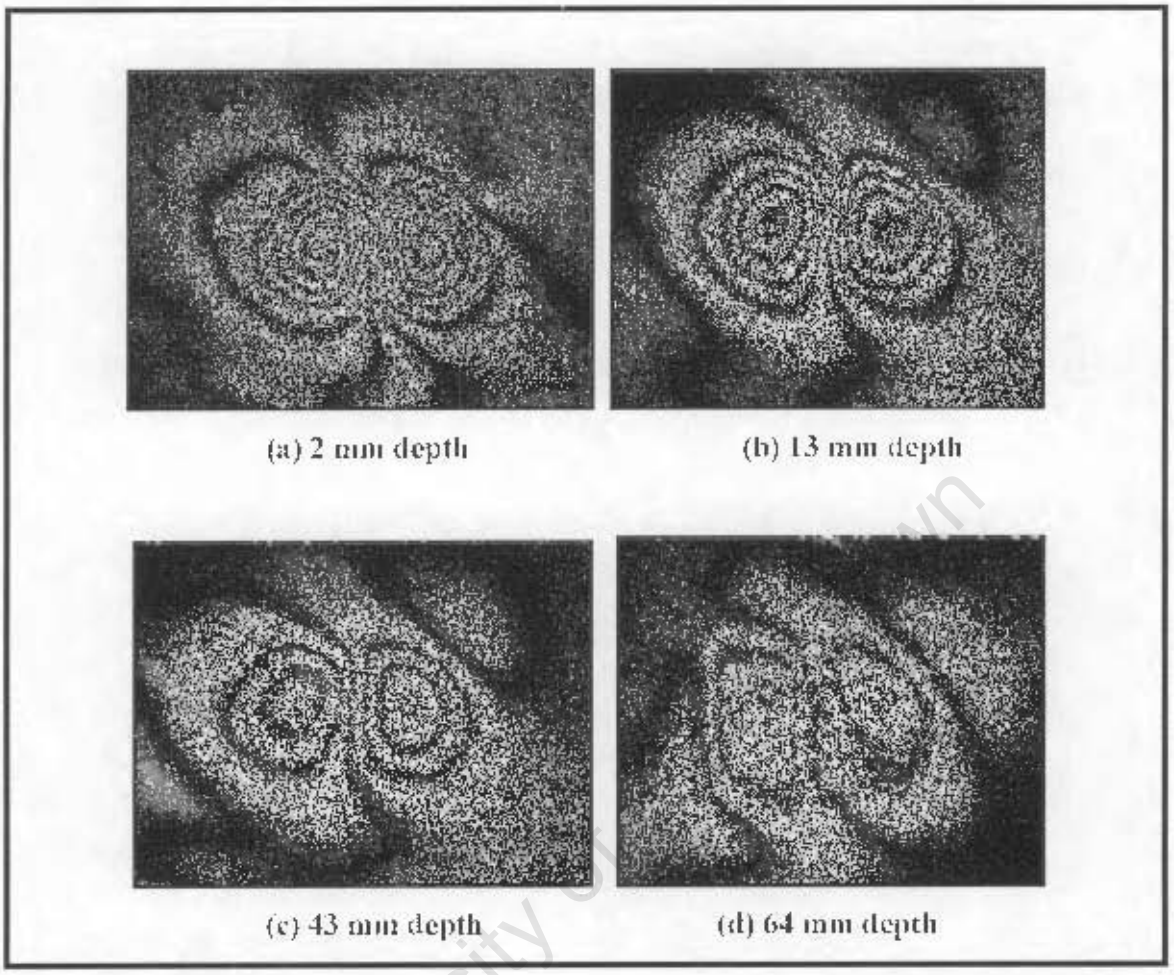

Figure 5. 5: (a)-(d): Fringe patterns due to front heating

Table 5.2 shows the data collected for this test. For convenience, the defects or flaws were labeled from 1 to 9 and each number corresponds to a specific depth as shown in table 5.2.

Table 5.1: Depth of defect as a function of average time in seconds

Defect number	Corresponding depth of defect (mm)	Average time taken to capture fringes in each flaw (seconds)
1	2	74.135
2	-	-
3	-	-
4	13	64.01
5	-	-
6	-	-
7	43	59.4
8	-	-
9	64	49.9

A graphical presentation of the data collected for the test (front heating) is shown in Figure 5.6 below.

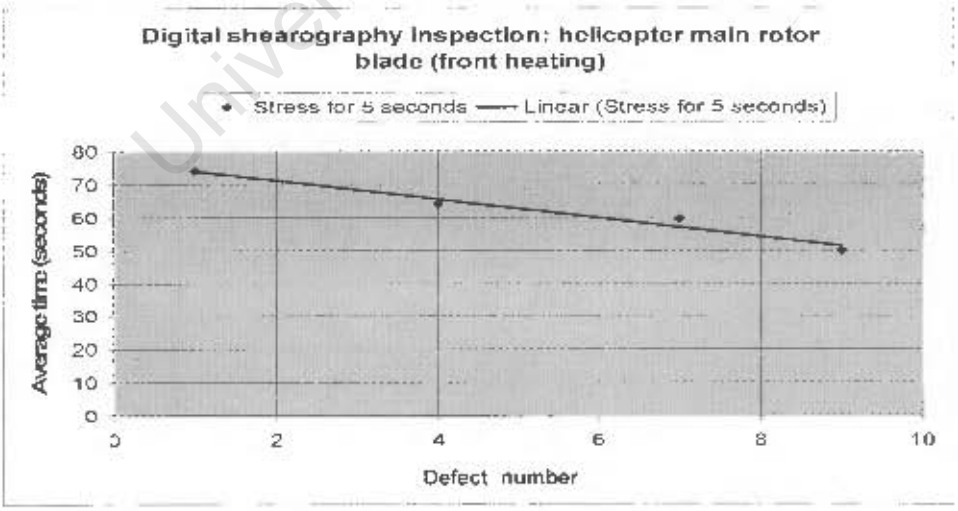

Figure 5.1: A graphical presentation of average time versus defect number

5.1.3 Results of experiments

5.1.3.1 Experiment no.1: Specimen no. 1 thermally stressed from far side

When the specimen is heated from the far side, the heat generated encounters the flaw much quicker and therefore gets localized faster as it further propagates through the material. There is less background noise during back heating (far side), and therefore the number of fringes created is fewer as opposed to when the specimen is front heated. Moreover, the fringes created, are of good quality and even, as compared to those created through front heating. The number of fringes created is also related to the depth of the flaw, and this can be observed from Figure 5.1(a)-(g), where the 2 mm defect depth, shown in figure 5.1(a), has more fringes than the other flaw depths. It should also be mentioned that, according to the design of the flaws in the specimen, the 2 mm flaw is along the trailing edge of the helicopter blade and much of the honeycomb had to be removed in order to obtain the desired flaw depth. This resulted in exposing the carbon fiber skin of the blade through which localization of heat took place. This implied that, the heat generated had direct contact with the carbon fiber skin and thus many fringes where created faster for this particular flaw. Figure 5.7 below (viewed from the top), shows the flaw positions (a) and (b) in red colour, and the heat flow through and around them. The blue boundary line represents the assumed thickness for the specimen.

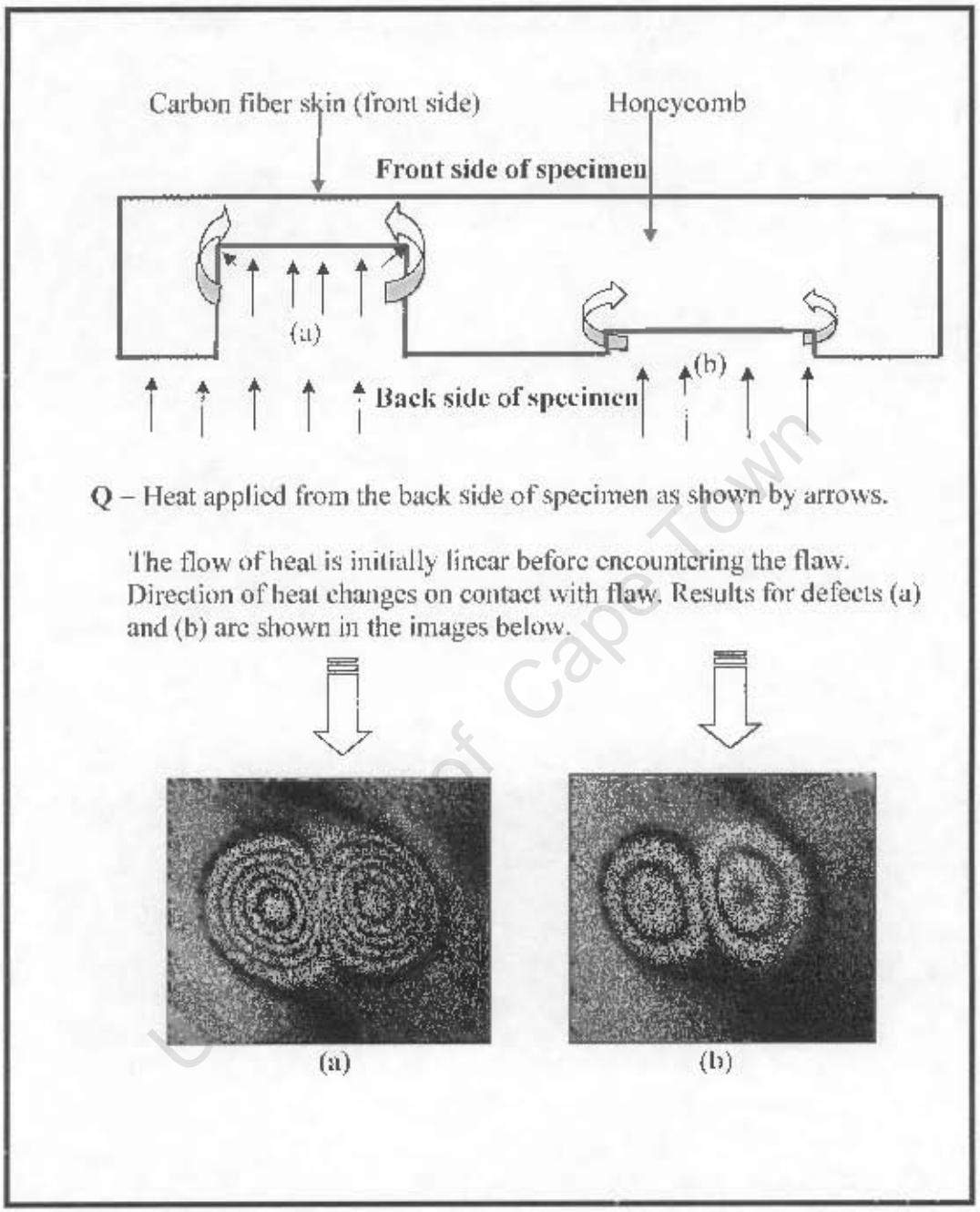

Figure 5.7: (a) Typical fringes for defect nearer to observer. (b) Typical fringes for defect further from observer.

For a "deeper flaw", the thickness of the honeycomb when measured from the inspection surface is obviously larger, and the heat has to filter through this thicker potion of the

honeycomb before encountering the inspection surface. This implies that the heat dissipates or degrades through the thickness of the honeycomb core from the flaw to the inspection surface. Thus the temperature at the surface is not high enough to create a large number of fringes. Consequently fewer fringes are created for a "deeper flaw". Figures 5.1(b)-(g) shows the trend of fringe pattern creation in relation to the depth of flaw, with the "deepest flaw" having the least number of fringes. Based on these findings, it is therefore, possible to quantify the depth of a defect or flaw during the inspection process.

5.1.3.2 Experiment no.2: Specimen no.1 thermally stressed from front side

During front heating, flaw manifestation is more complex, and there is considerable background noise generated in the image of the surface being inspected. Initially, the heat generated permeates through the carbon fiber skin, and then through the honeycomb matrix before encountering the flaw. The core beneath the surface acts as a conduit accelerating the rate of heat propagation toward the flaw space. When the heat flow reaches the "delamination" it slows down as it encounters a less conductive medium. It is only then that the build up of heat in the space between skin (inspection surface) and depth of flaw begins to increase affecting the surface temperature and hence the creation of fringes. For delaminations very near the inspection surface the build up of heat is faster hence the creation of large number of fringes at the beginning of the process. By the time the deeper flaws begin to manifest their presence the ones near the surface have cooled down and show reduced number of fringes. The shapes of fringes also are not as even, compared to those created by back heating.

The procedure, however, in terms of quantification of defects or flaws is similar in both cases. In this case, "smaller depths" from the inspecting surface, produces more fringes initially than deeper ones and this can be confirmed by the results obtained in Figure 5.5(a)-(d). This is also graphically represented in Figure 5.6 above. Figure 5.8 in the top view, is an illustration of the heat flow through the specimen, and the resulting fringes

created during front heating. The depth of the defect is measured from the front side of the specimen.

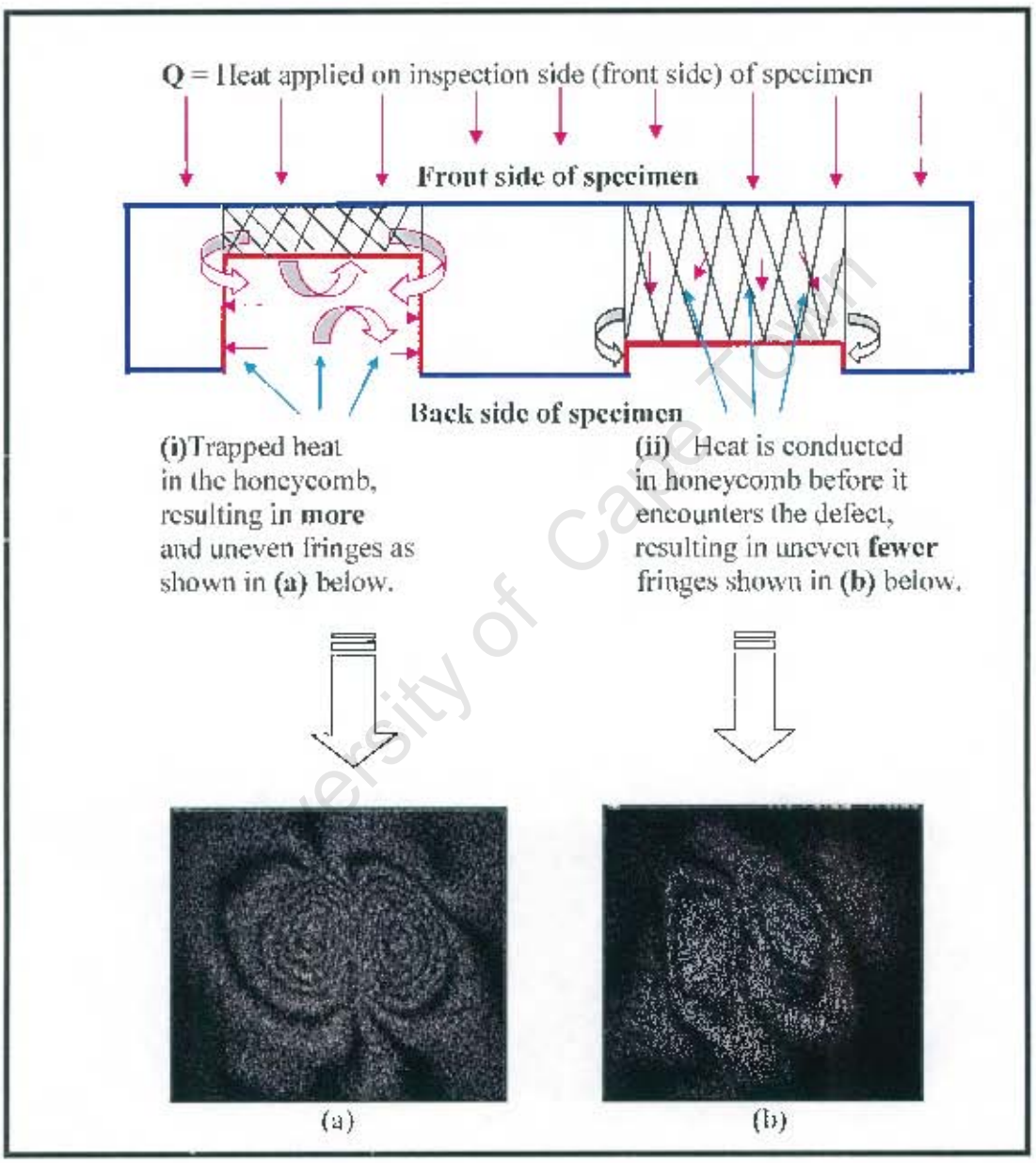

Figure 5. 8: (a) Typical fringes for "shallow defect" (b) Typical fringes for "deeper defect"

5.1.3.3 Experiment no.3: Specimen no. 1 thermally stressed uniformly

The flaw depths were numbered from 1 to 9, to correspond to their respective depth sizes as discussed earlier. Initially, a high concentration of fringes was observed from flaws 1, 2, 3, and 4 as seen in Figure 5.9. These were the shallow flaws and the fringe patterns were captured as they formed. It was obviously not possible to see all the flaws clearly during the first video show because of variations in the temperature differences between the flaws, which were dependent on the flaw depth, and therefore the cooling rates were different. Other flaws started showing fringes after refreshing the video. This was, however, expected especially from deeper flaws (more material). By then flaws 1, 2, and 3, in Figure 5.10, showed a diminished number of fringes as compared to the rest of the flaws. On the other hand, fringe patterns for flaws 7, 8, and 9 became more visible after further cooling.

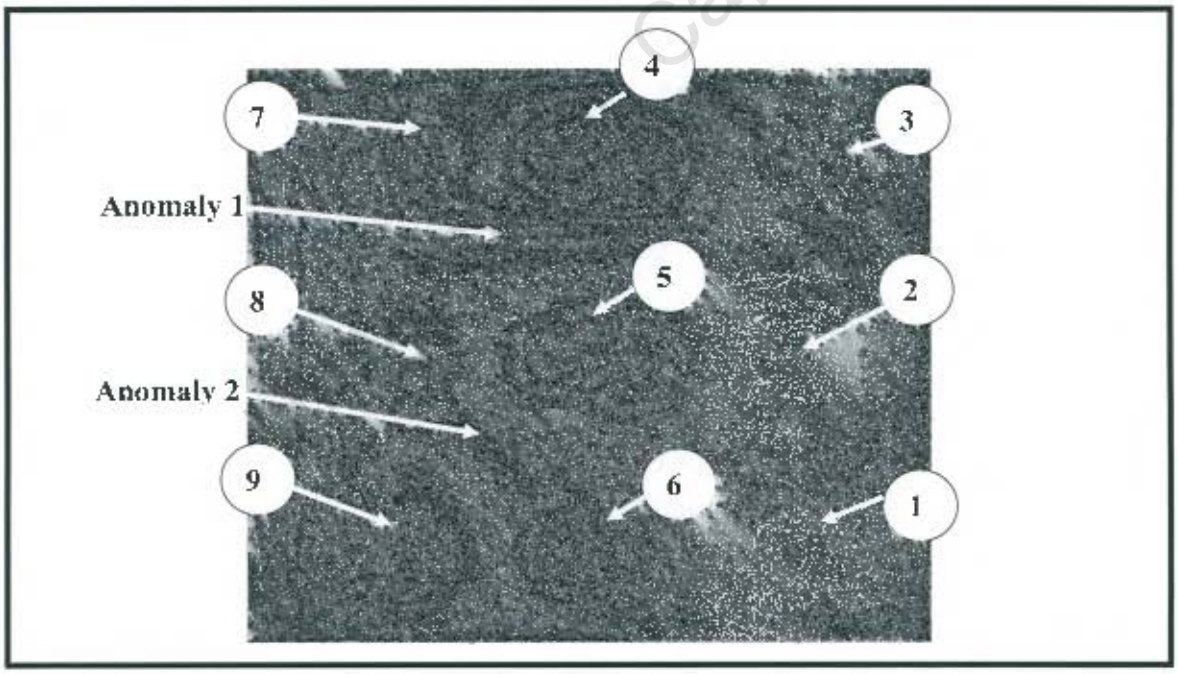

Figure 5. 9: Flaws 1, 2, 3 and 4, showing a high concentration of fringes

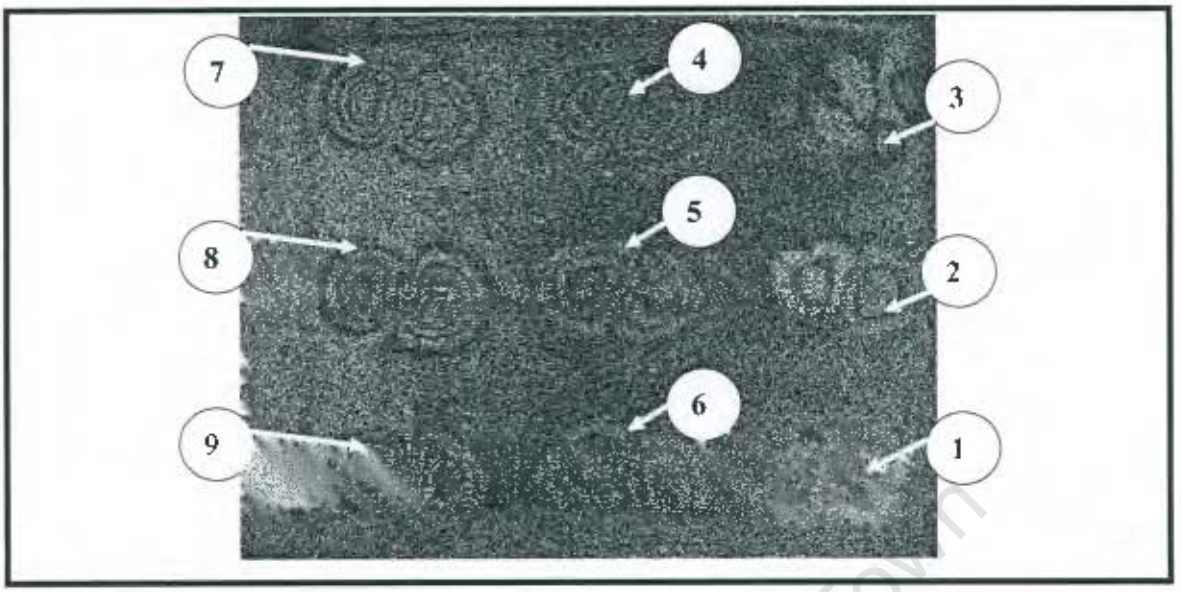

Figure 5.10: Fringe patterns for flaws 7, 8, and 9 clearly visible

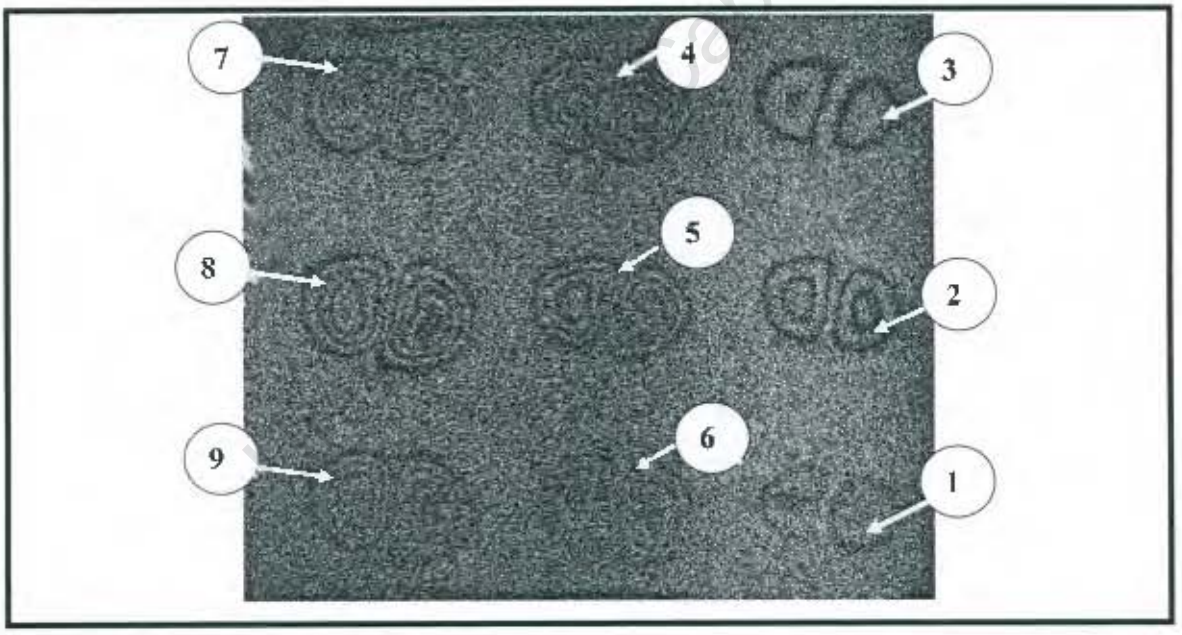

Figure 5.11: Flaws 1, 2, and 3 depicting reduced number of fringes

There were some distortions in the material which were revealed by shearography during the initial stages of fringe creation. This is demonstrated by anomaly 1 and 2 shown in Figure 5.9 above. This is also an indication of the sensitivity of digital shearography to flaw detection. A large portion along flaws 7, 8, and 9 in Figure 5.9, near the leading

edge of the blade, shows a distorted pattern, and hence the fringe patterns around these flaws are not as clear as was expected. However, after further cooling, a different picture of fringe patterns free from distortion was exposed. This is clearly illustrated in Figure 5.10 and Figure 5.11 above. The reduced number of fringes for flaws 1, 2, and 3, was expected after further cooling. This was due to small temperature difference taking place around each flaw. In other words, the flaw depths are smaller, hence lesser amount of material as compared to those with large portions of honeycomb. This therefore results in their inability to create further fringes, later during the cooling down period.

5.1.3.4 Experiment no.4: Impact damage testing of UAV composite

A preliminary investigation was conducted during the experiment and several samples of the same material were initially inspected for artificially created BVID, before carrying out inspections on the actual test specimens. It was discovered that the material could not retain the created damage permanently in some instances. Initially, Shearography did reveal very vividly the "defects" created immediately after impact without any stressing (thermal or otherwise) and it was possible to count the number of fringes created within these first few minutes of inspection. The situation, however, was different once the specimen had relaxed from the impact after a longer time. The initially recorded image of fringes depicting the familiar "double bull's eye" was not visible again as expected when the specimen was thermally stressed. It clearly showed that, the material recovered from impact to a large extent as long as the skin material was not cracked or perforated.

Based on the observations made above, it became apparent that, the relaxation time of the material could be monitored with a view of establishing the BVID threshold. The first specimen was therefore, prepared and two BVID were created at different heights. The specimen was then inspected six times at intervals of thirty minutes while the material appeared to self recover or heals itself. The results obtained are presented in table 5.3 below.

Table 5. 3: Inspection intervals verses capturing time of fringes in phase

Inspection Intervals	Capturing time of fringes in phase mode(seconds)	Number of fringes Captured for defect one (22 mm height)	Number of fringes Captured for defect two (14 mm height)
1	30.5	5	4
2	273	5	4
3	541	5	4
4	897	5	4
5	1258	5	4
6	1656	5	4

It should be noted that during the relaxation period of three hours (i.e. six observations, one half hour (30 min) apart) the arbitrary choice of observing the creation of four fringes, yielded ever increasing time period. For example initially the rate of recovery from the impact is very fast in that it takes 30.5 seconds to produce four fringes. In contrast after the fourth interval (i.e. 2 hours into the test) the rate of relaxation has been considerably reduced and it took 897 seconds to produce 4 fringes again. After capturing the last image, the specimen was left to relax further, and only subjected to shearographic inspection by thermal inspection on the following day. The images captured on this day, did not, however, produce the same number of fringes or for that matter the characteristic bull's eye as shown in figure 5.12 and 5.13. A graphical presentation of the data shown in table 5.3 is shown in Figure 5.14. The graph suggests that after prolonged relaxation, more time would be required to create a (chosen) "significant" number of fringes, and these fringes were likely to reduce significantly to a point where it may not be possible or barely see the damage, particularly the "flaw" created by impact.

In order to study the behavior of the specimen's material to impact, another specimen was prepared with five BVID introduced from five different impact heights. The images

obtained after the specimen had relaxed for approximately 15 hours are presented in Figure 5.15 and Figure 5.16 respectively. The designations A and B in the images refer to defects with five and four fringes in the left lobe respectively. The image with less number of fringes (B) had received lesser impact.

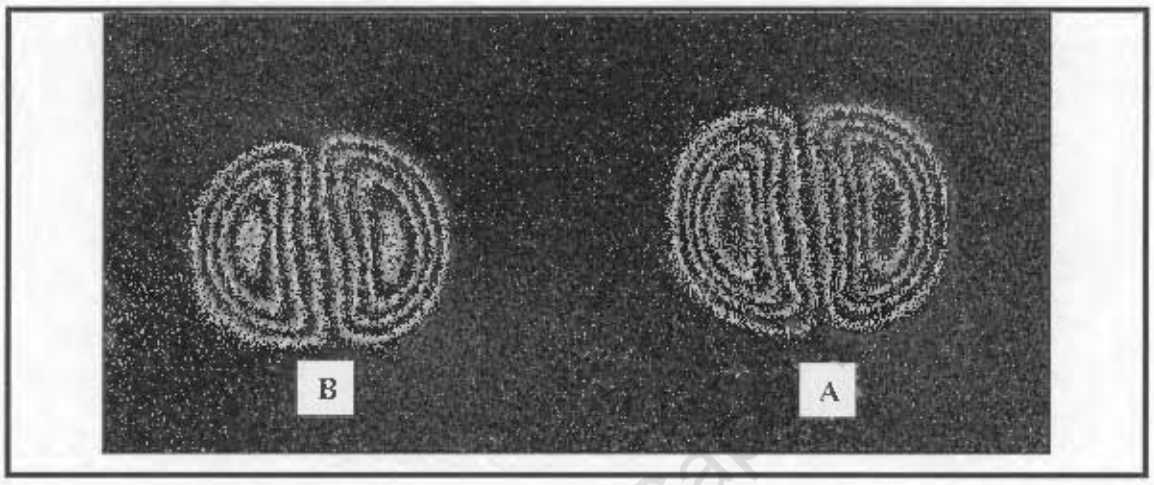

Figure 5.12: Phase fringes captured initially (1st inspection interval) created during 30.50 sec

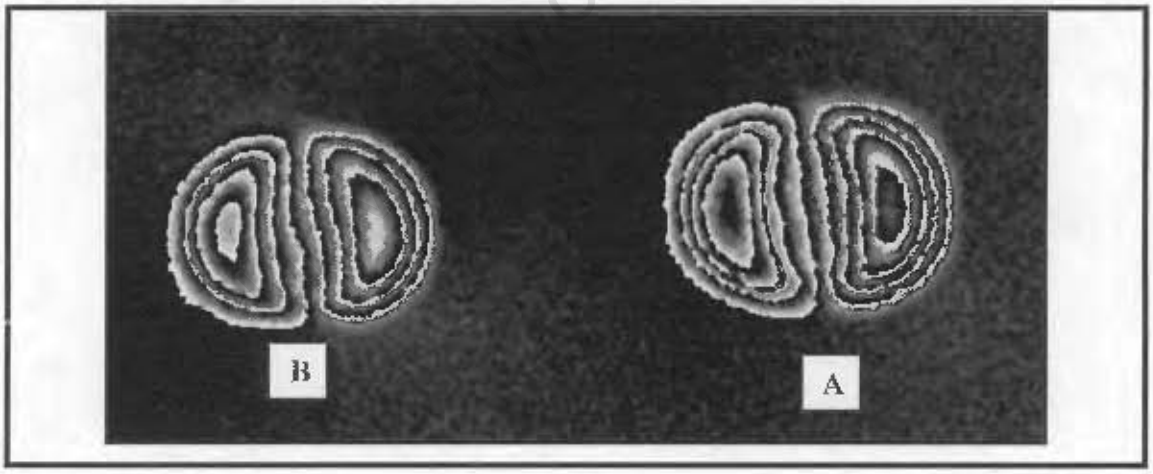

Figure 5.13: Phase filter for fringes as in Figure 5.13.

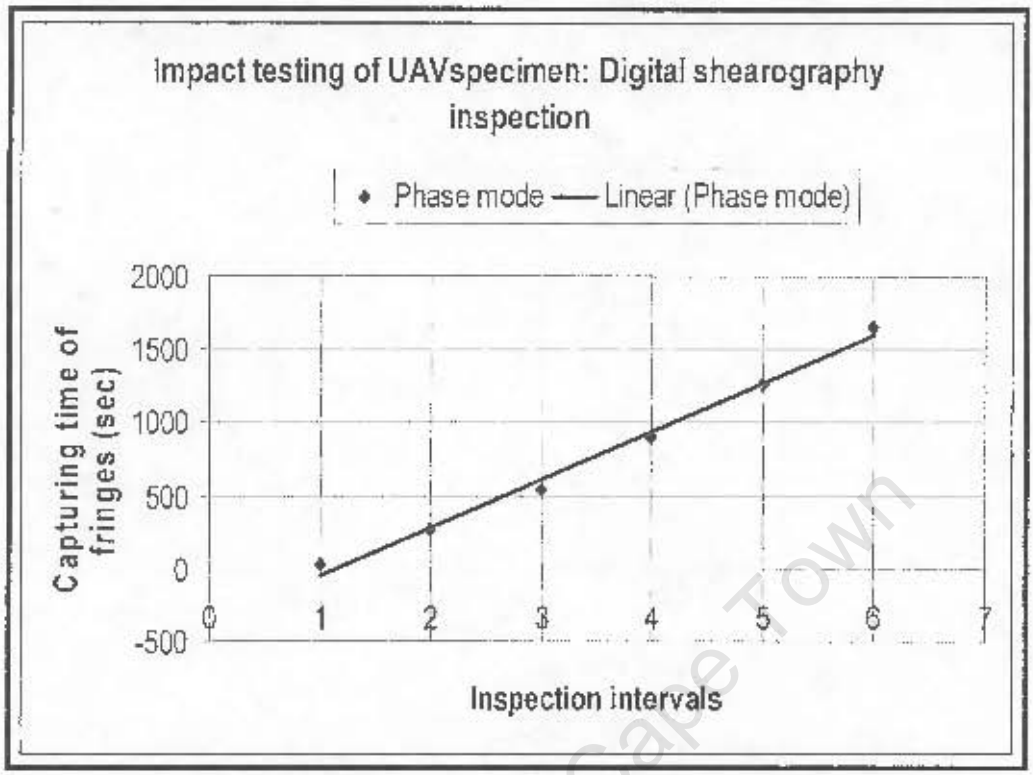

Figure 5.14: Capturing time of fringes verses inspection intervals

Figure 5.15 below shows the image captured on a specimen that was subjected to different impact levels, was left to relax and finally thermally stressed to reveal if any damage was permanent. Table 5.4 shows the impact levels A to E.

Table 5.4: Impact levels A to E

Impact position	Impact height (mm)
A	260
B	210
C	160
D	110
E	60

At position 'E' (Figure 5.15) you can hardly see the fringes, but there is still an indication of the position of impact. Position 'E', appears to be, the threshold for BVID in this experiment. Interestingly, the flaw at position 'A' (with highest impact) is not significant in Figure 5.15. This, however, is revealed by the 'kink' at 'A' in Figure 5.16(see circled spot) after further phase filtering.

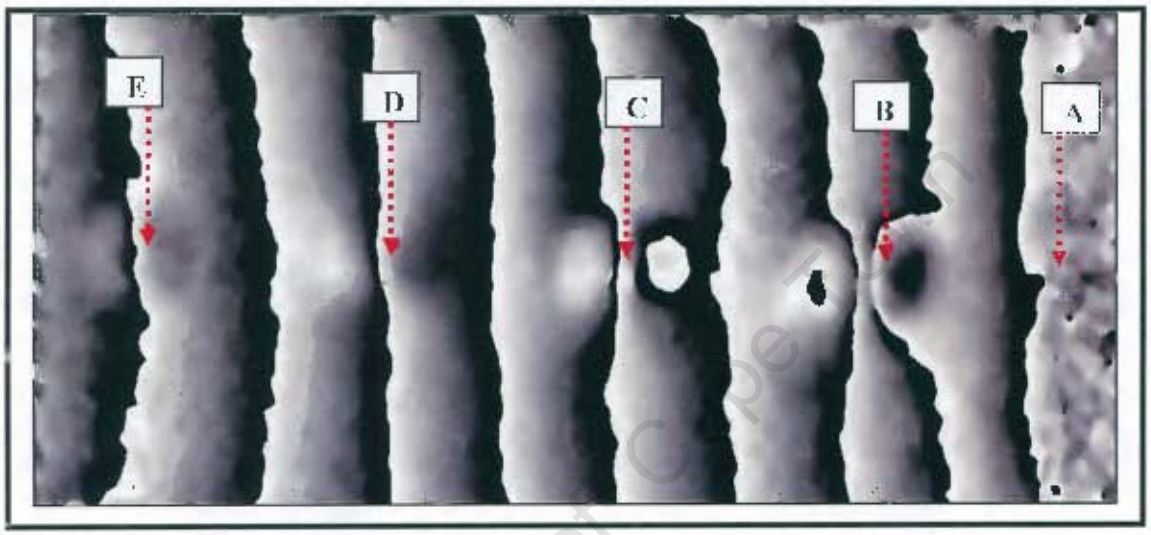

Figure 5. 15: Phase filtered images on application of heat stressing

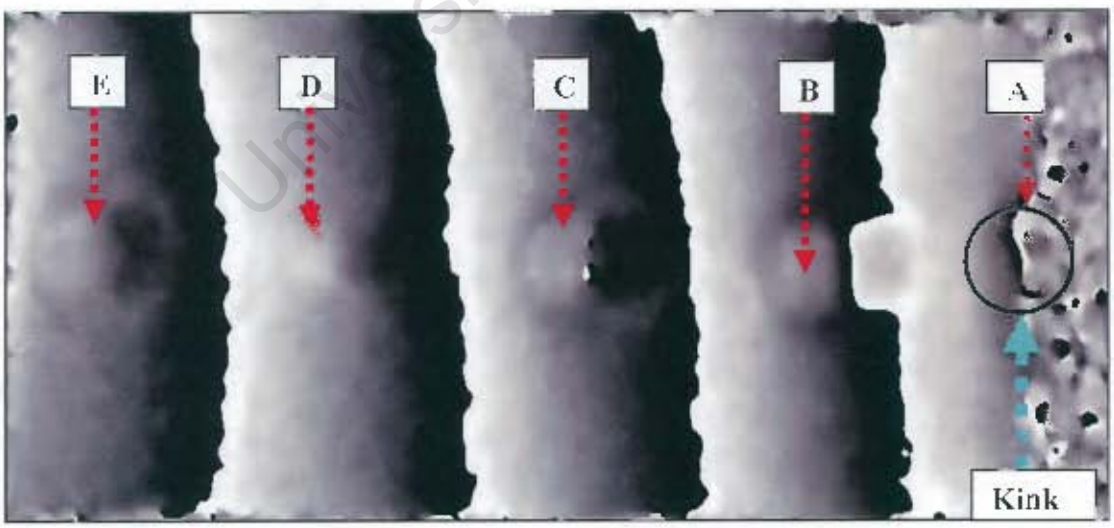

Figure 5. 16: Phase filtered images after refreshing and during further cooling of the specimen shown in figure 5.15

Specimen: UAV wing with BVID, front heating for 5 seconds

The results for this type of inspection are shown in Figure 5.17 and Figure 5.18

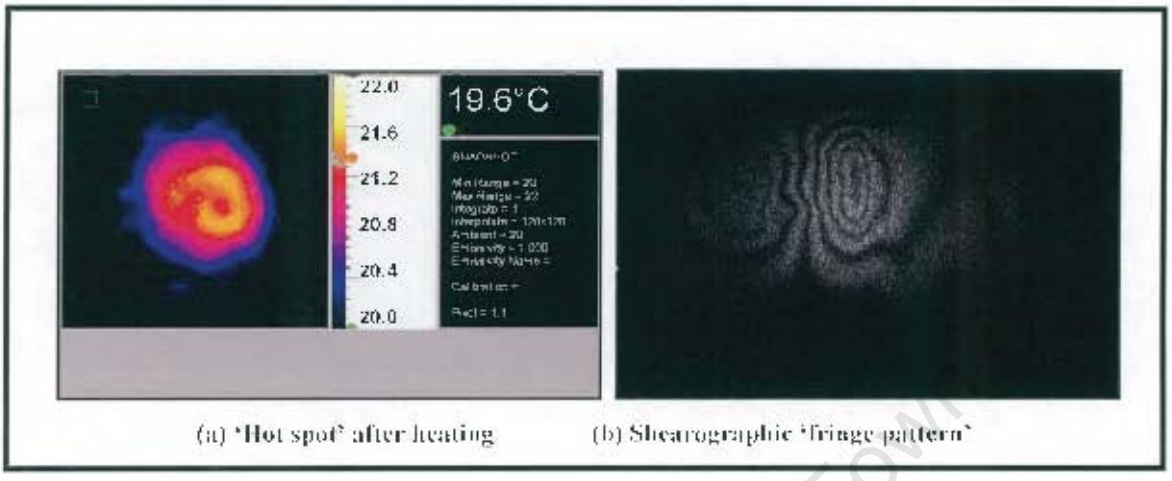

(a) 'Hot spot' after heating (b) Shearographic 'fringe pattern'

Figure 5.17: (a) IRISYS system; (b) Shearographic system

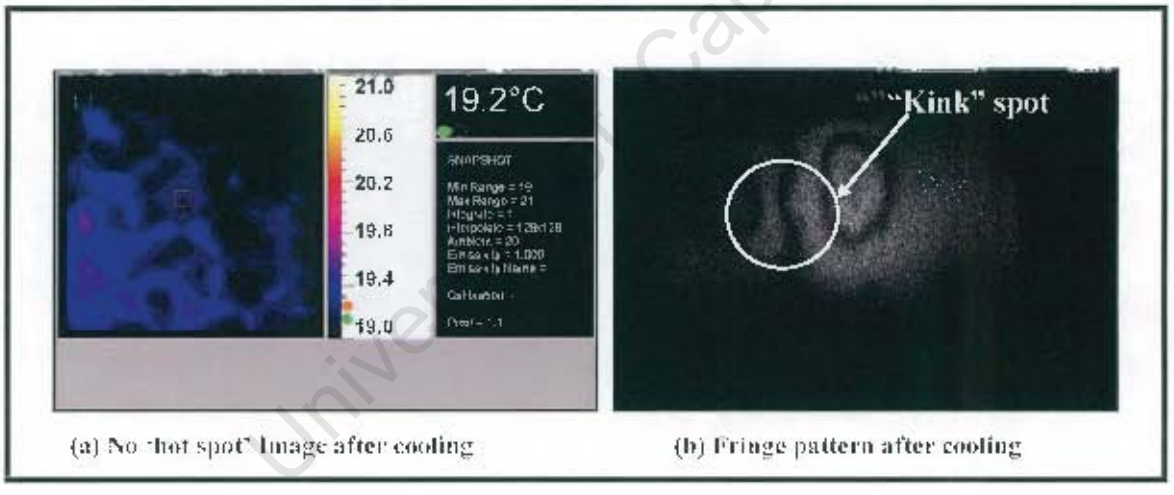

(a) No 'hot spot' image after cooling (b) Fringe pattern after cooling

Figure 5.18: (a) IRISYS system; (b) Shearographic system

Specimen: UAV wing with BVID, front heating for 10 seconds

Typical results are shown in Figure 5.19 and Figure 5.20

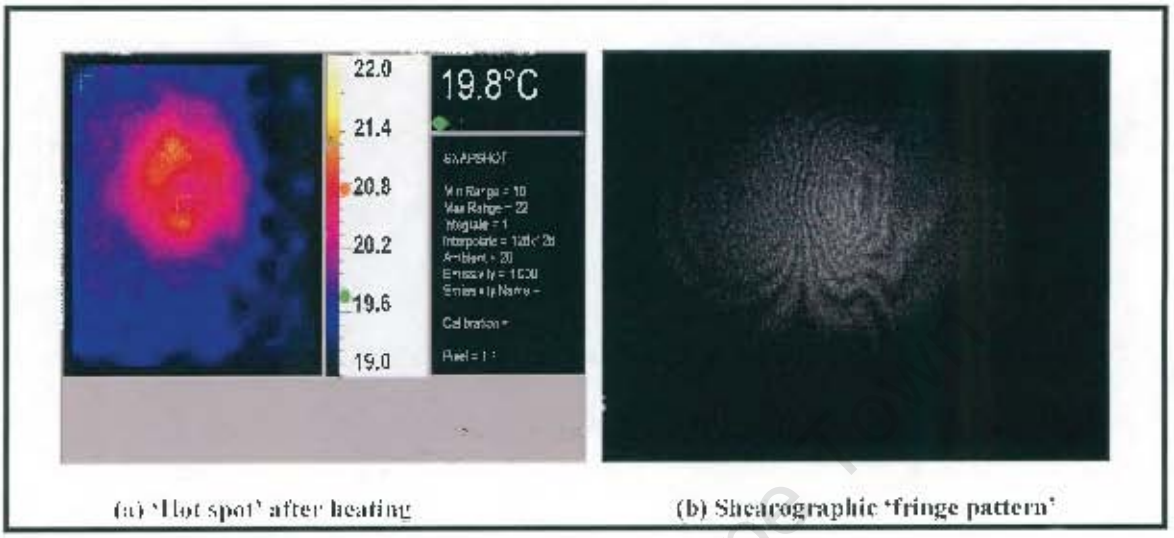

(a) 'Hot spot' after heating (b) Shearographic 'fringe pattern'

Figure 5.19: (a) IRISYS system; (b) Shearographic system

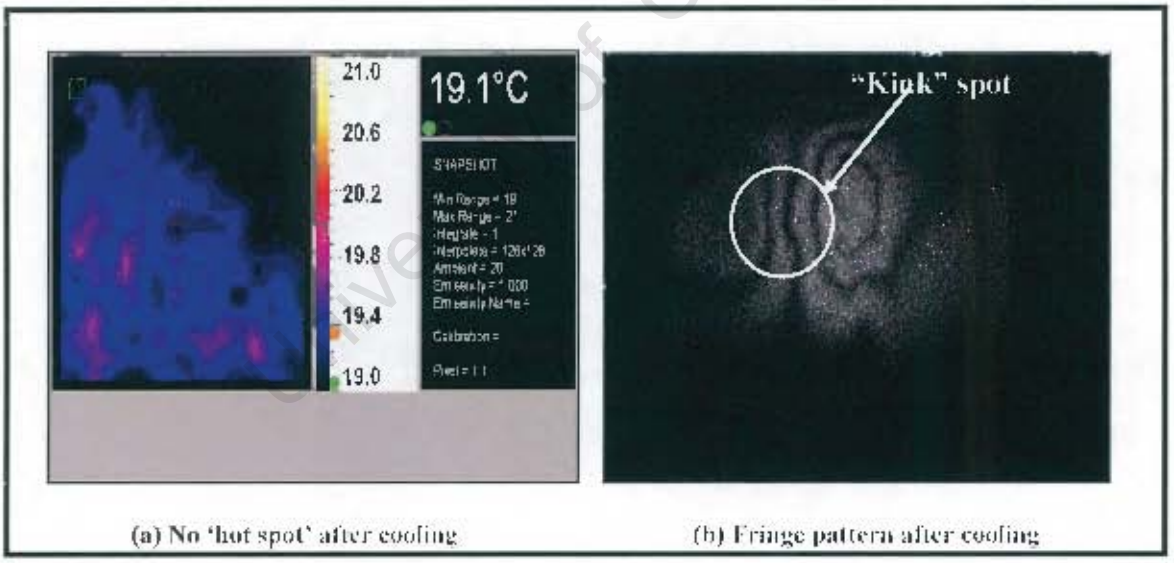

(a) No 'hot spot' after cooling (b) Fringe pattern after cooling

Figure 5.20: (a) IRISYS system; (b) Shearographic system

Specimen: UAV wing with BVID, front heating for 15 seconds

Typical results are shown in Figure 5.21 and Figure 5.22

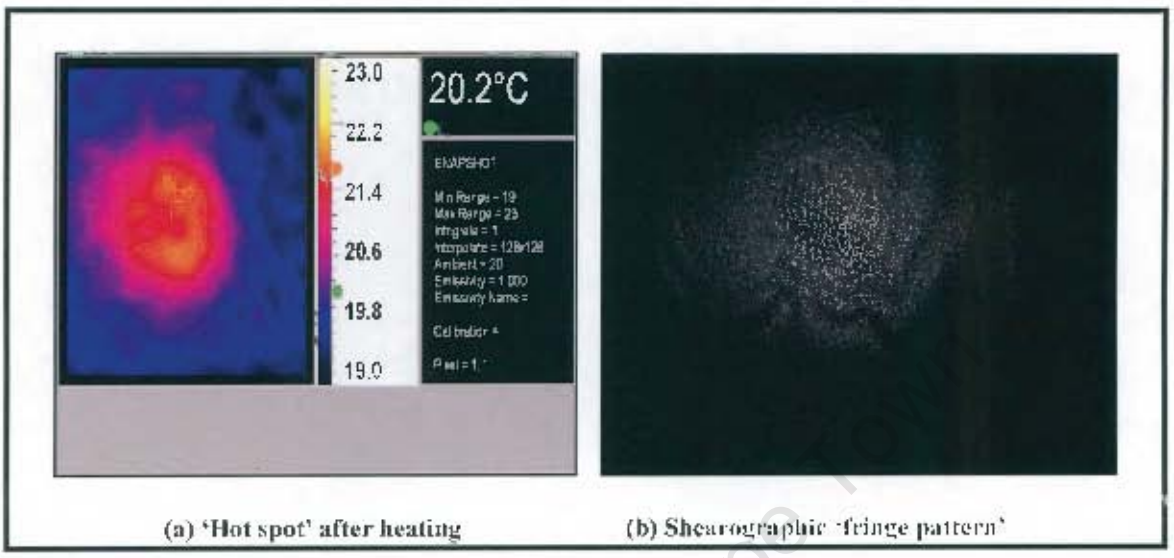

(a) 'Hot spot' after heating (b) Shearographic 'fringe pattern'

Figure 5. 21: (a) IRISYS system; (b) Shearographic system

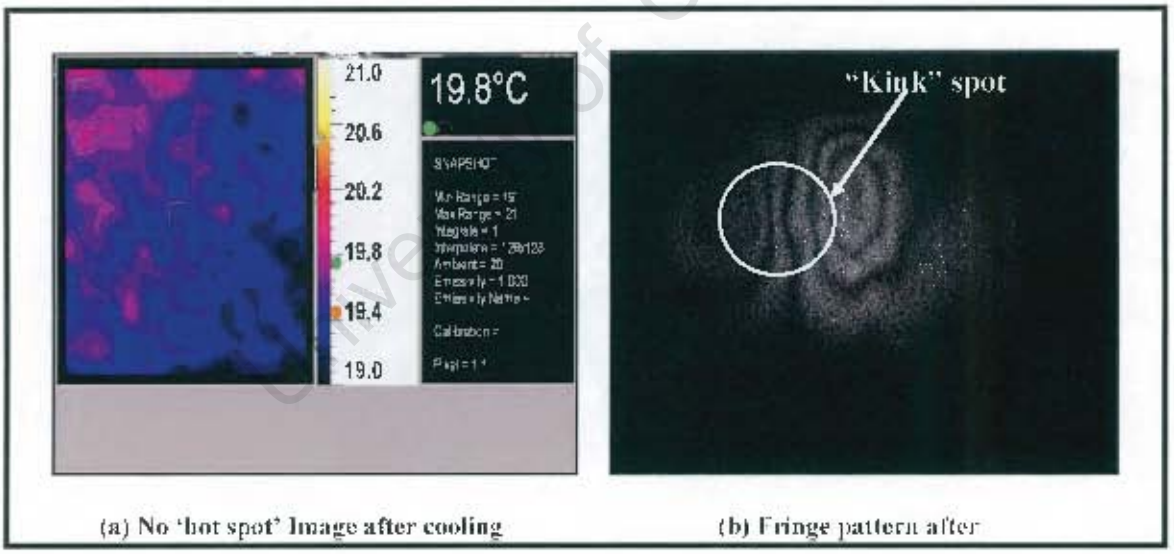

(a) No 'hot spot' Image after cooling (b) Fringe pattern after

Figure 5.22: (a) IRISYS system; (b) Shearographic system

Specimen: UAV wing with BVID, far side heating for 5 seconds

Typical results are shown in Figure 5.23 and Figure 5.24

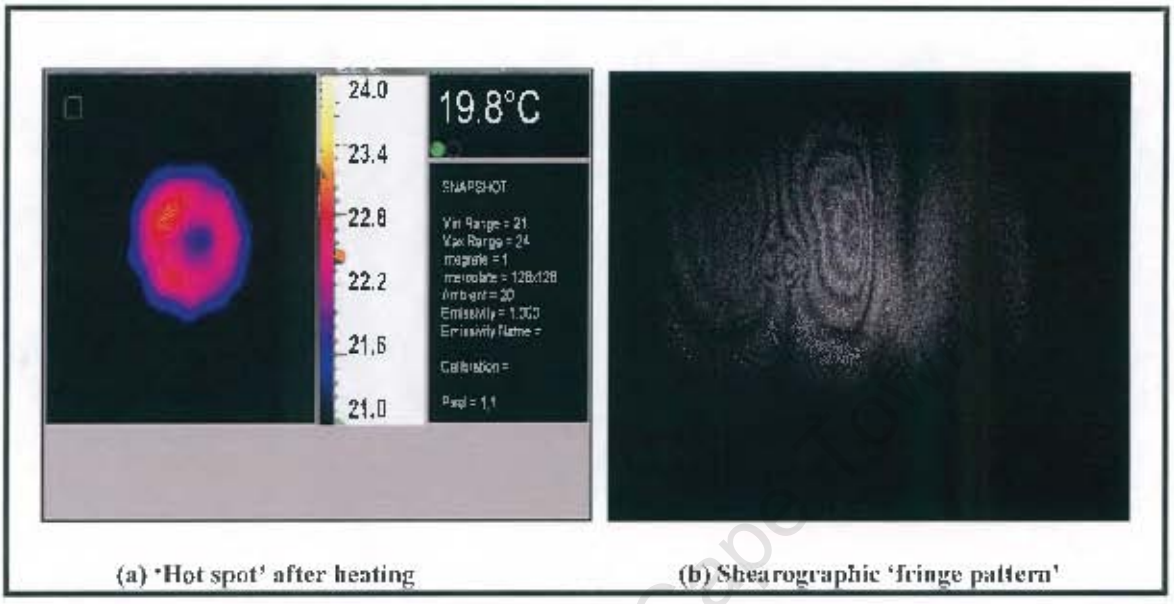

(a) 'Hot spot' after heating (b) Shearographic 'fringe pattern'

Figure 5. 23: (a) IRISYS system; (b) Shearographic system

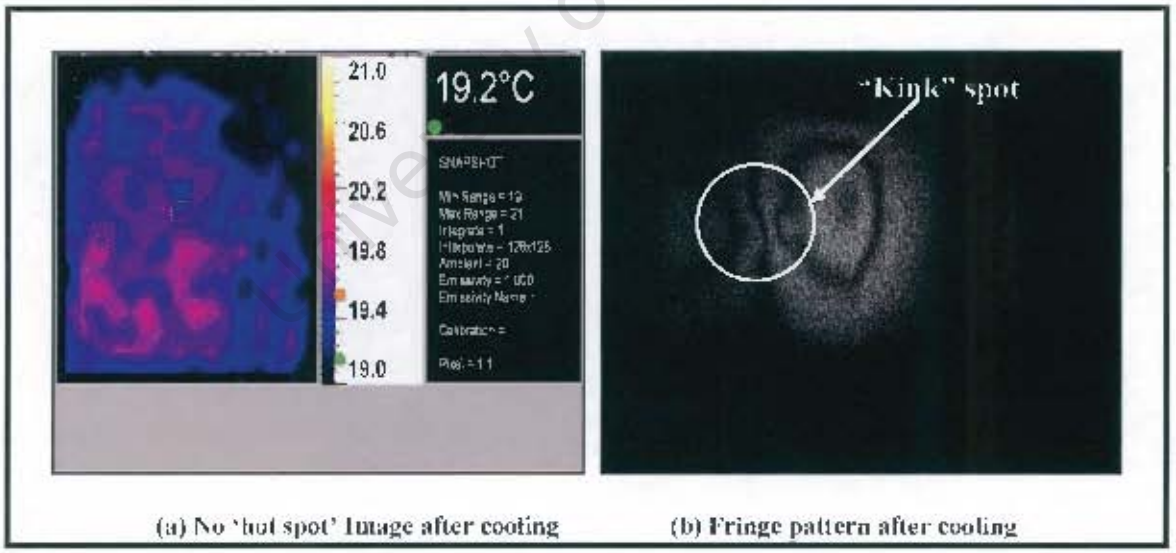

(a) No 'hot spot' Image after cooling (b) Fringe pattern after cooling

Figure 5.24: (a) IRISYS system; (b) Shearographic system

Specimen: UAV wing with BVID, far side heating for 10 seconds
Typical results are shown in Figure 5.25 and Figure 5.26

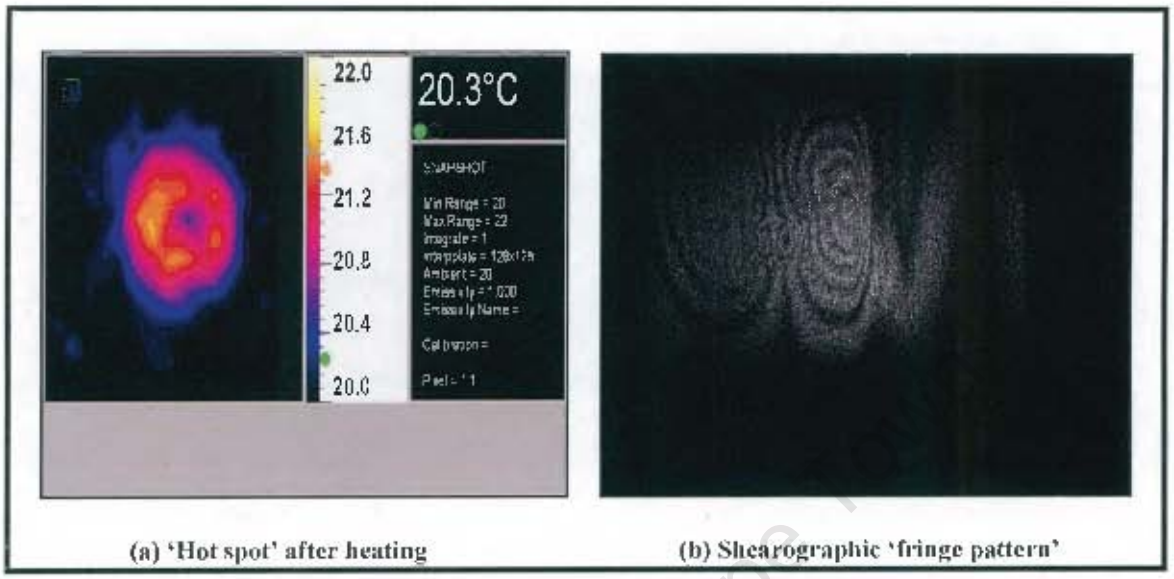

(a) 'Hot spot' after heating (b) Shearographic 'fringe pattern'

Figure 5.25: (a) IRISYS system; (b) Shearographic system

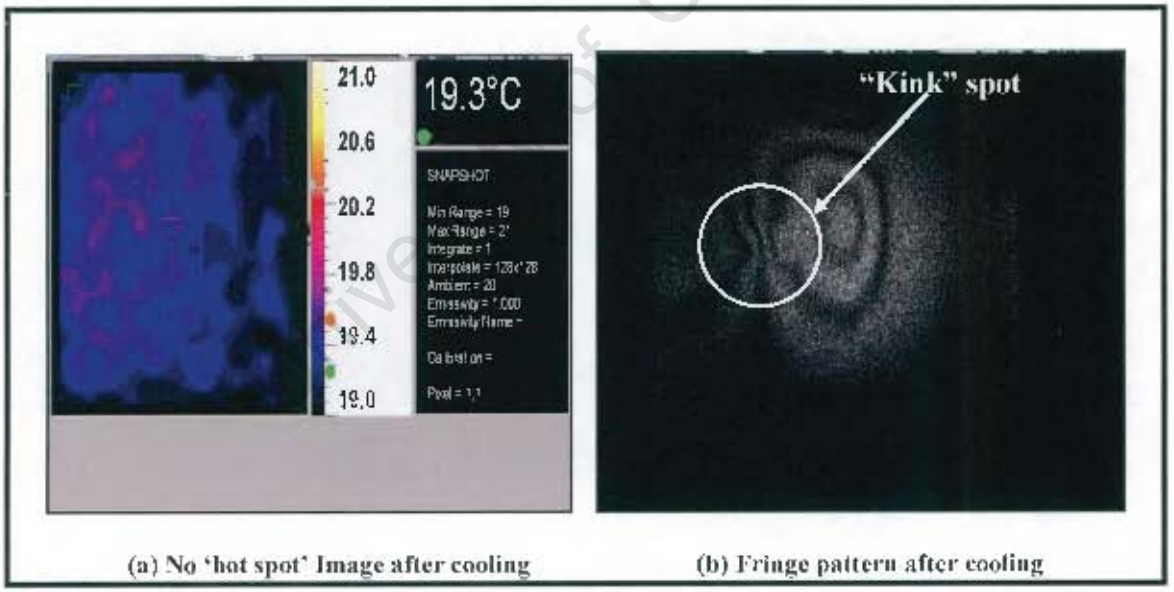

(a) No 'hot spot' Image after cooling (b) Fringe pattern after cooling

Figure 5.26: (a) IRISYS system; (b) Shearographic system

Specimen: UAV wing with BVID, far side heating for 15 seconds

Typical results are shown in Figure 5.27 and Figure 5.28

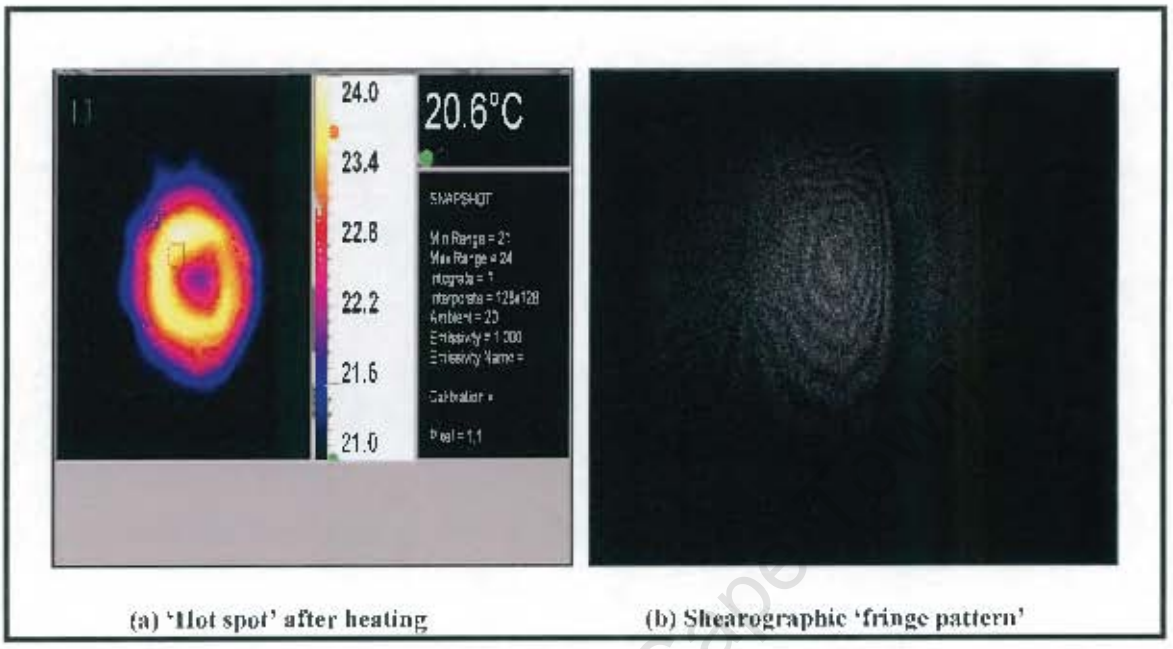

(a) 'Hot spot' after heating (b) Shearographic 'fringe pattern'

Figure 5. 27: (a) IRISYS system; (b) Shearographic system

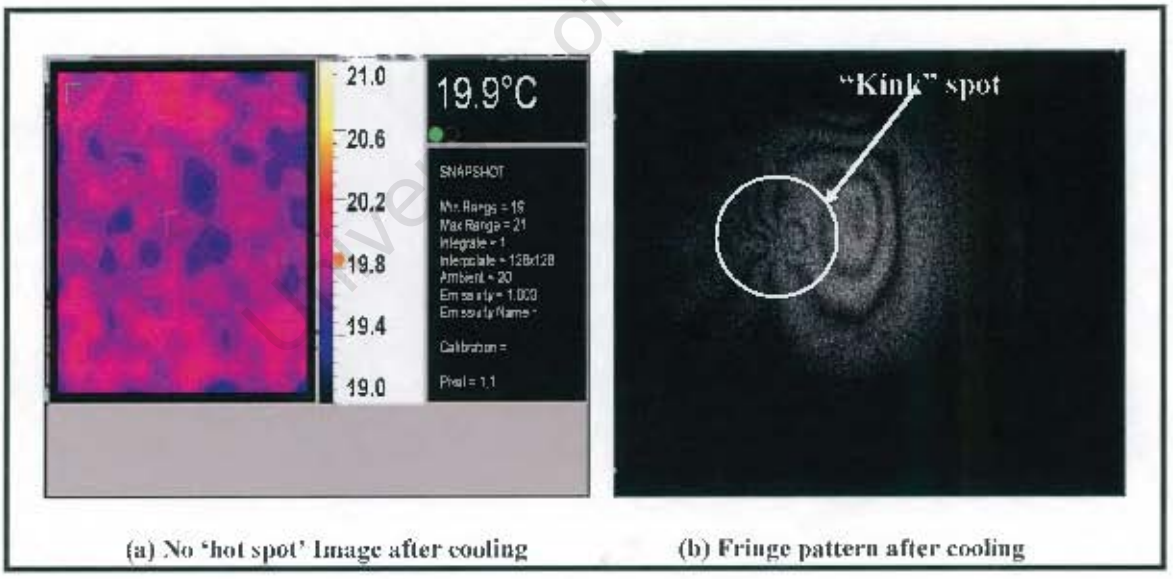

(a) No 'hot spot' Image after cooling (b) Fringe pattern after cooling

Figure 5. 28: (a) IRISYS system; (b) Shearographic system

Specimen: Helicopter blade with 3 defects, far side heating for 5 sec

Typical results are shown in Figure 5.29 and Figure 5.30

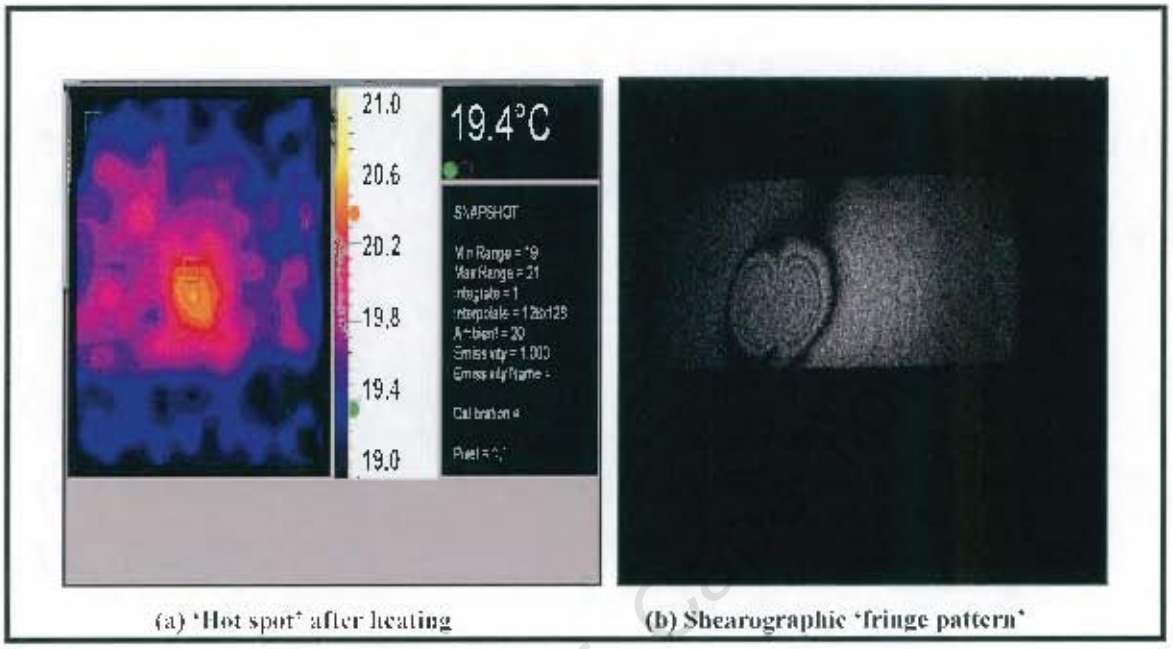

(a) 'Hot spot' after heating (b) Shearographic 'fringe pattern'

Figure 5. 29: (a) IRISYS system: (b) Shearographic system

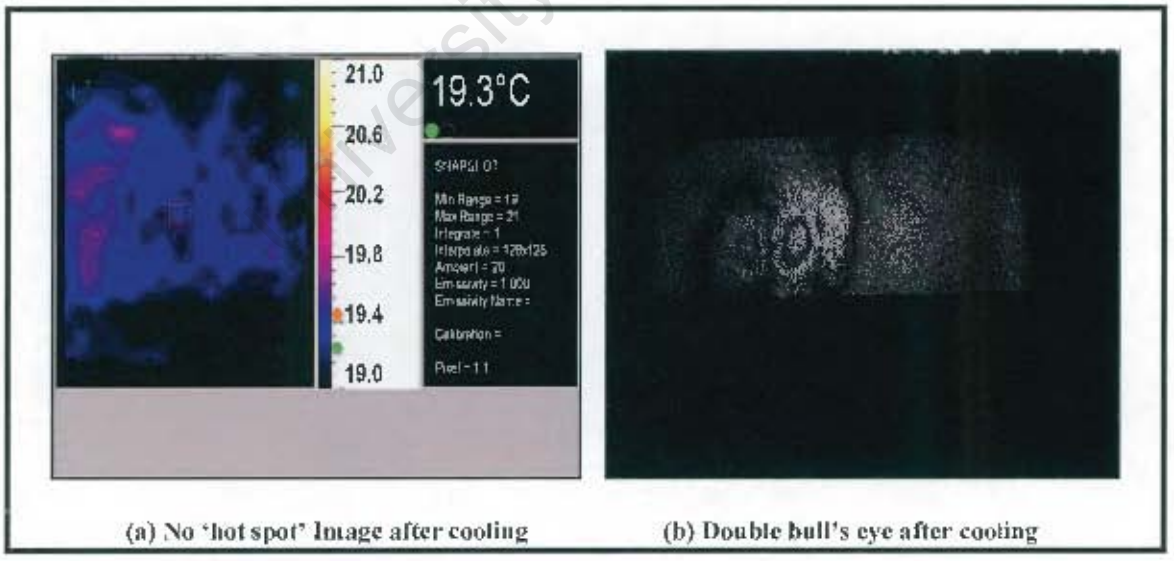

(a) No 'hot spot' Image after cooling (b) Double bull's eye after cooling

Figure 5. 30: (a) IRISYS system; (b) Shearographic system

Specimen: Helicopter blade with 3 defects, far side heating for 10 sec

Typical results are shown in Figure 5.31 and Figure 5.32

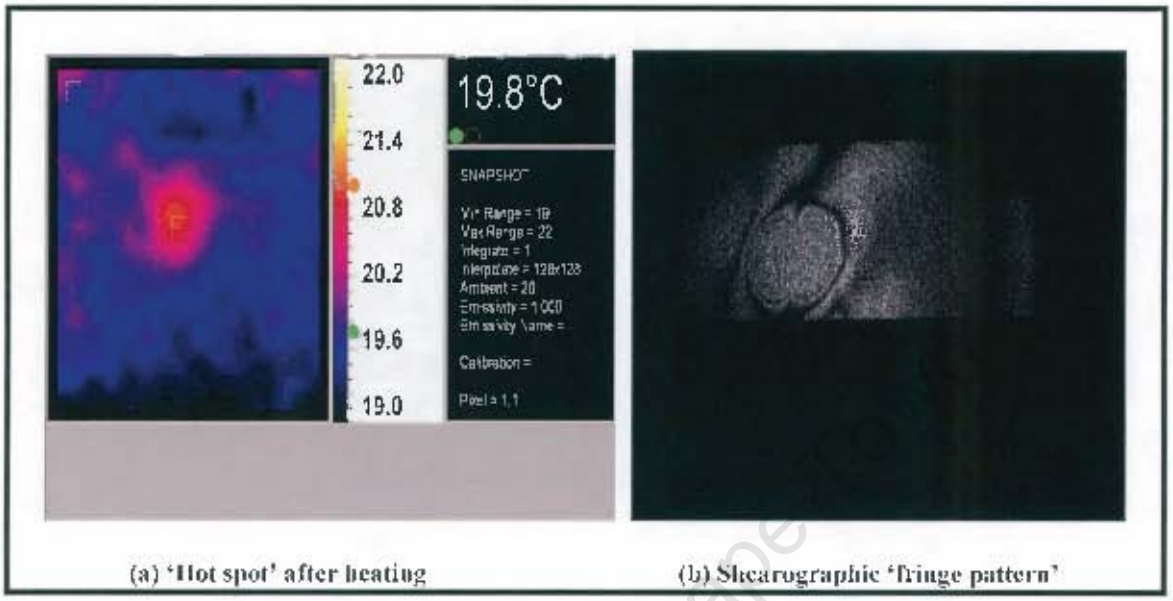

(a) 'Hot spot' after heating (b) Shearographic 'fringe pattern'

Figure 5. 31: (a) IRISYS system; (b) Shearographic system

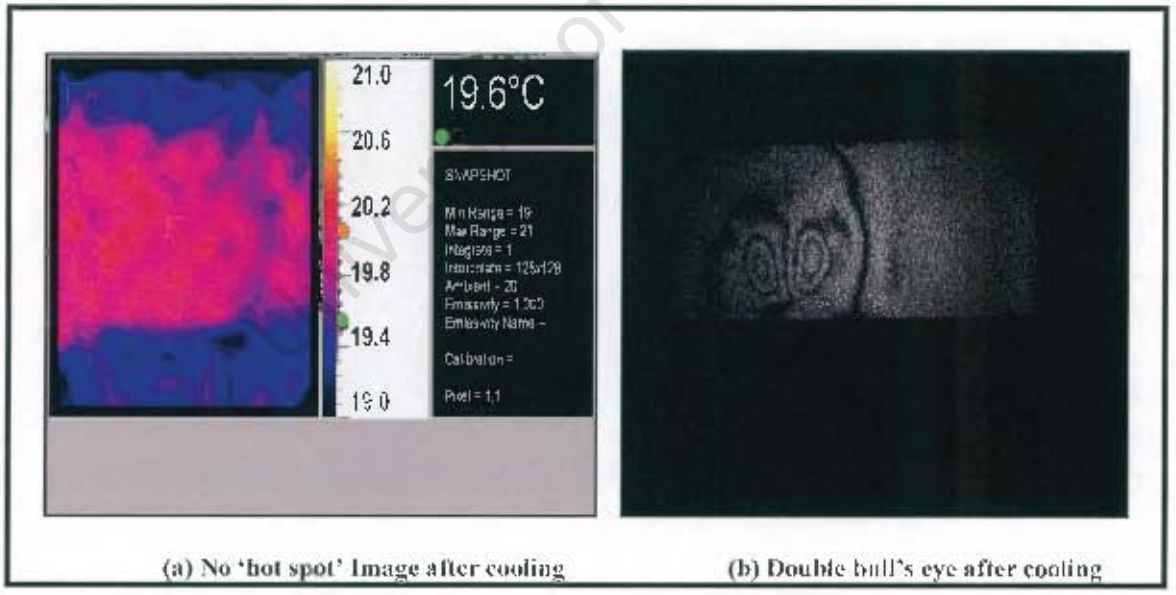

(a) No 'hot spot' Image after cooling (b) Double bull's eye after cooling

Figure 5. 32: (a) IRISYS system; (b) Shearographic system

Specimen: Helicopter blade with 3 defects, far side heating for 15 sec

Typical results are shown in Figure 5.33 and Figure 5.34

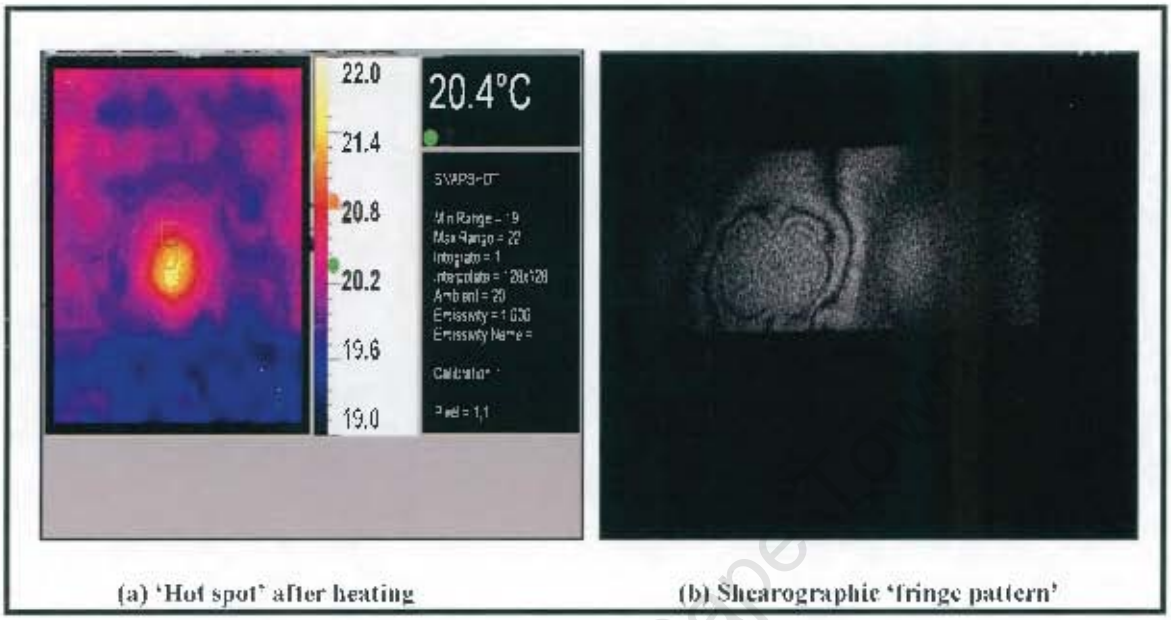

(a) 'Hot spot' after heating (b) Shearographic 'fringe pattern'

Figure 5.33: (a) IRISYS system; (b) Shearographic system

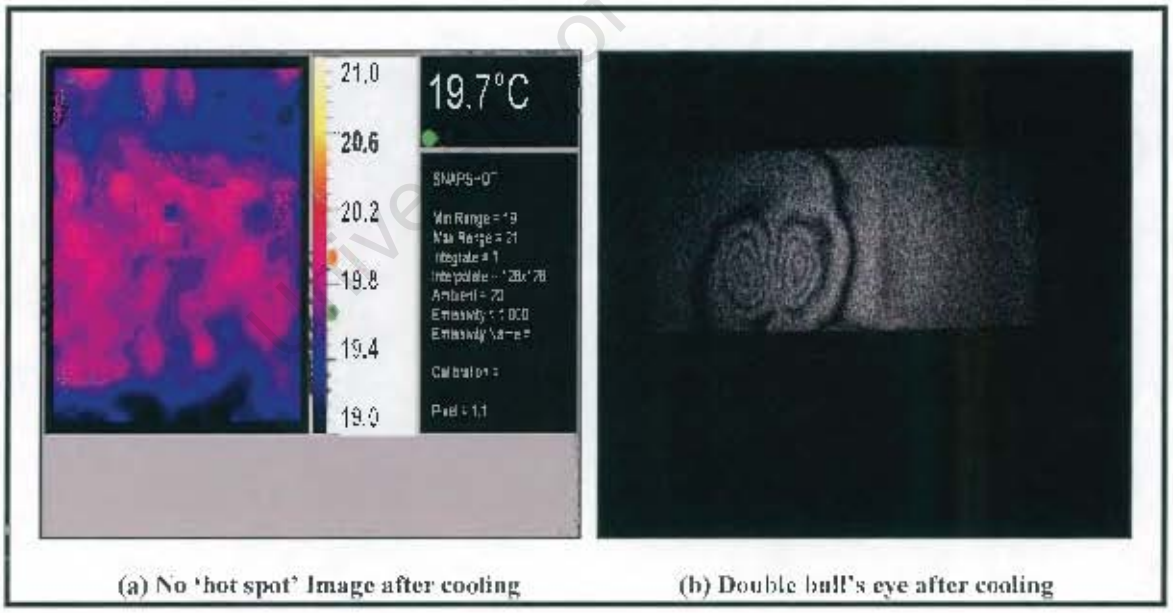

(a) No 'hot spot' Image after cooling (b) Double bull's eye after cooling

Figure 5. 34: (a) IRISYS system; (b) Shearographic system

Specimen: Helicopter blade with 3 defects, front heating for 5 sec

Typical results are shown in Figure 5.35 and Figure 5.36

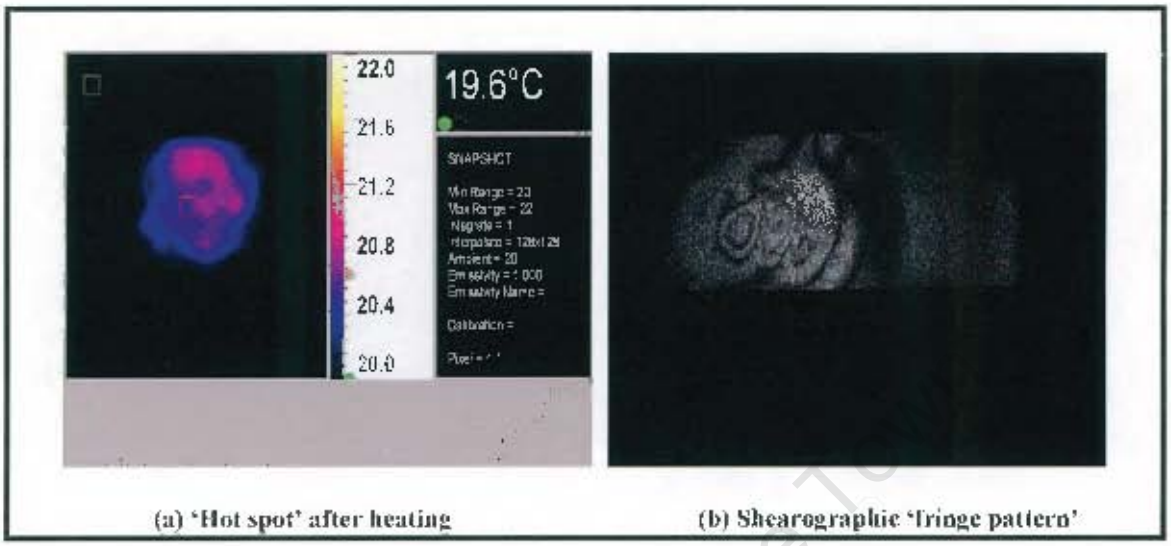

(a) 'Hot spot' after heating (b) Shearographic 'fringe pattern'

Figure 5. 35: (a) IRISYS system; (b) Shearographic system

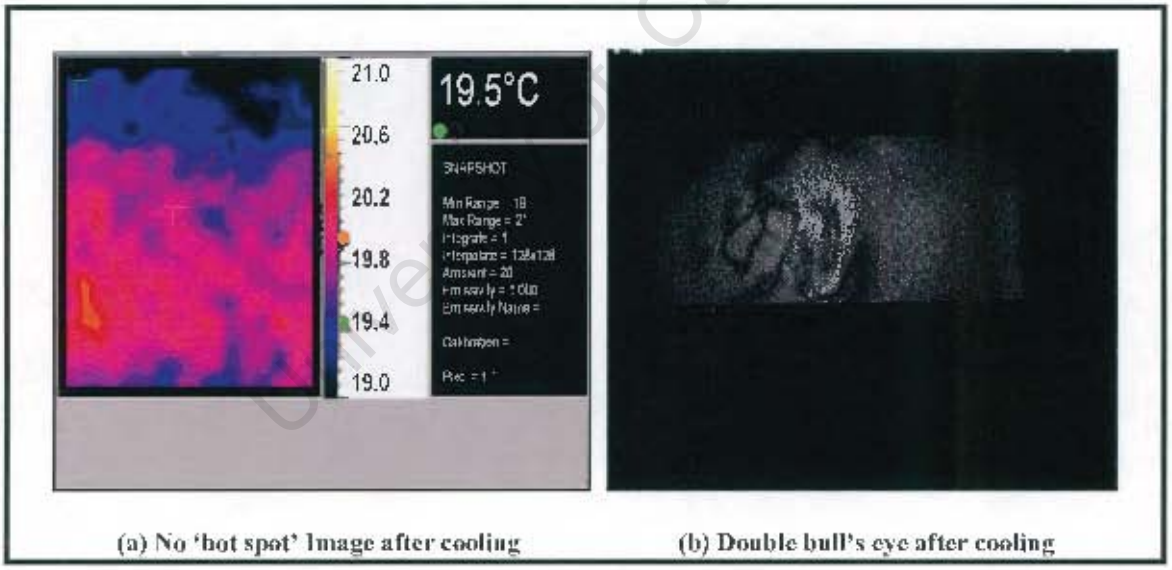

(a) No 'hot spot' Image after cooling (b) Double bull's eye after cooling

Figure 5. 36: (a) IRISYS system; (b) Shearographic system

Specimen: Helicopter blade with 3 defects, front heating for 10 sec

Typical results are shown in Figure 5.37 and Figure 5.38

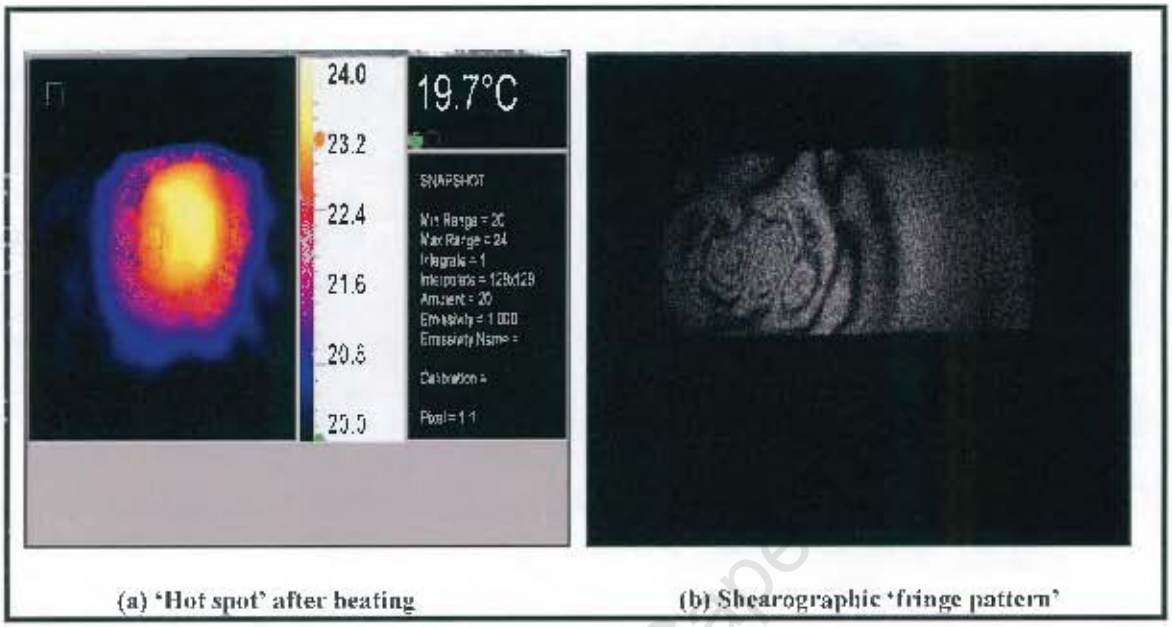

(a) 'Hot spot' after heating (b) Shearographic 'fringe pattern'

Figure 5.37: (a) IRISYS system; (b) Shearographic system

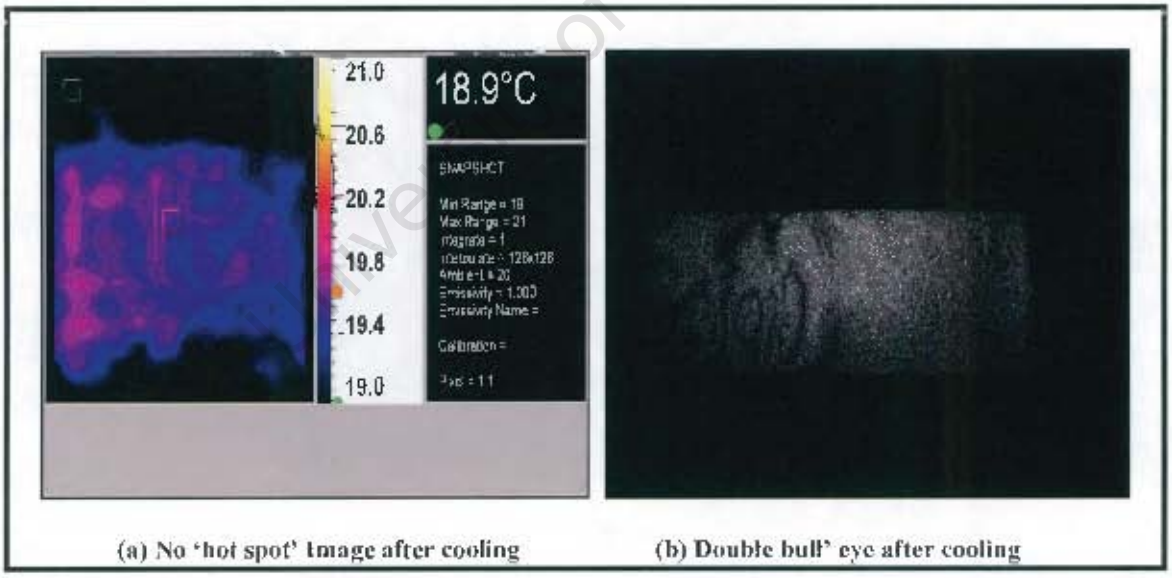

(a) No 'hot spot' image after cooling (b) Double bull' eye after cooling

Figure 5.38: (a) IRISYS system; (b) Shearographic system

Specimen: Helicopter blade with 3 defects, front heating for 15 sec

Typical results are shown in Figure 5.39 and Figure 5.40

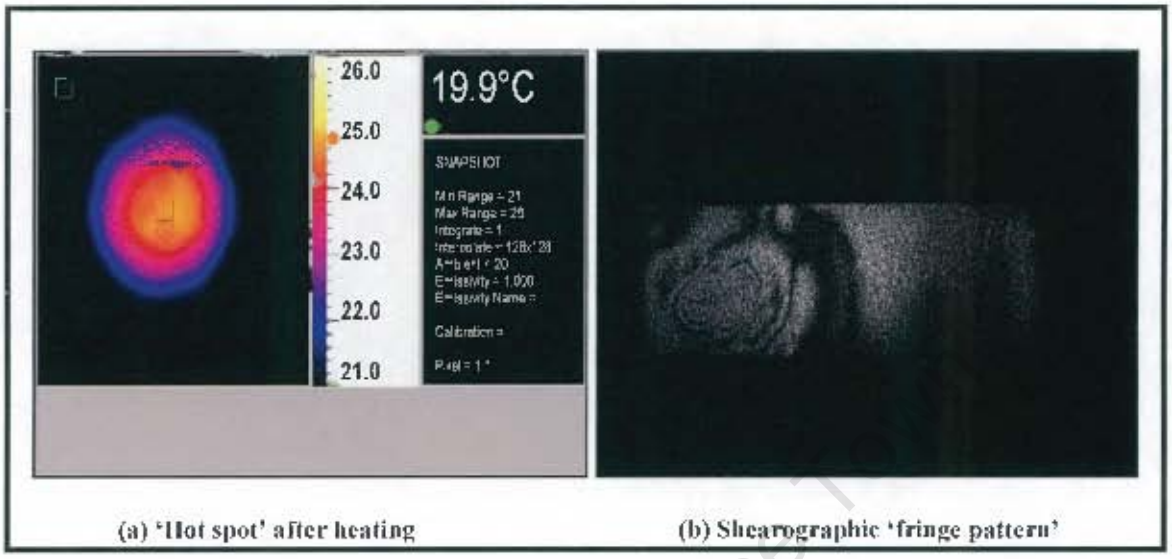

(a) 'Hot spot' after heating (b) Shearographic 'fringe pattern'

Figure 5.39: (a) IRISYS system; (b) Shearographic system

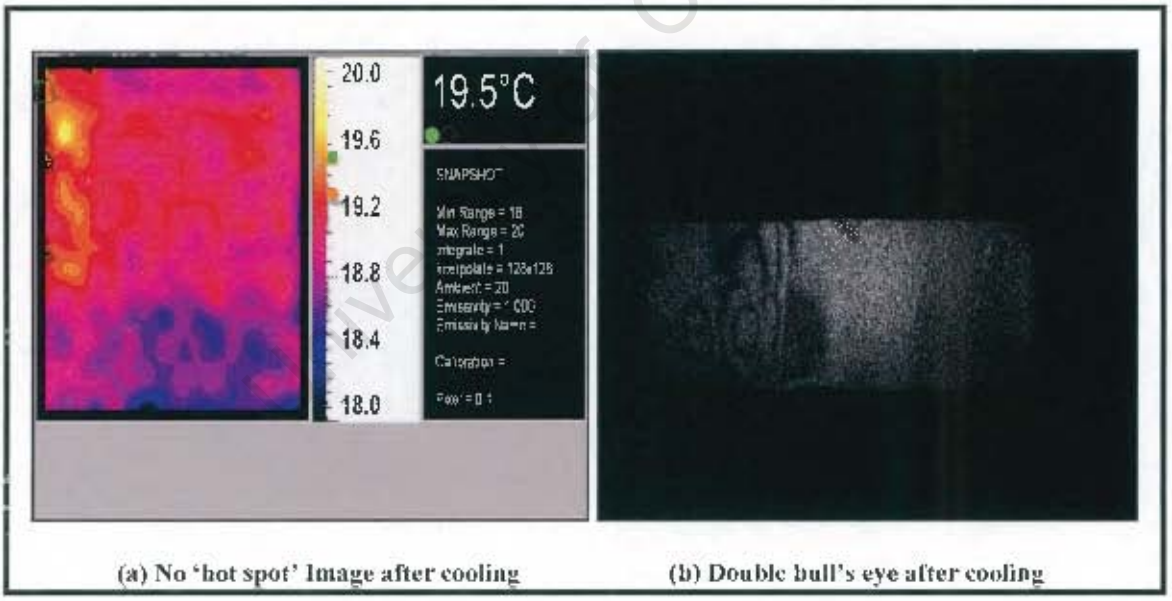

(a) No 'hot spot' Image after cooling (b) Double bull's eye after cooling

Figure 5.40: (a) IRISYS system; (b) Shearographic system

Specimen: Helicopter blade with 9 defects, front heating for 5 sec

Typical results are shown in Figure 5.41 and Figure 5.42

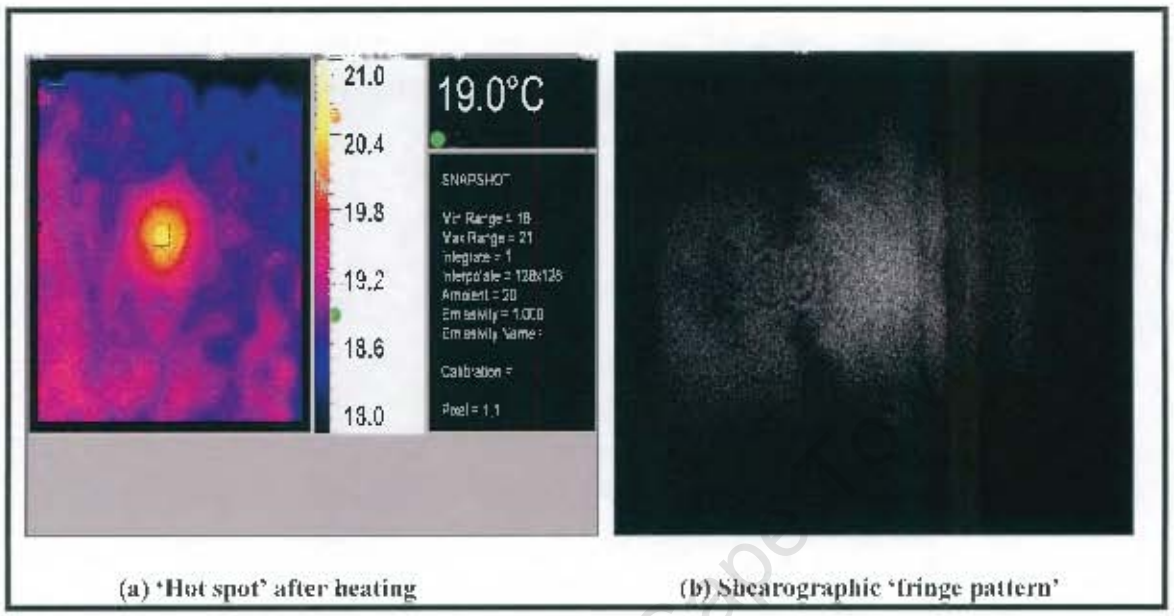

(a) 'Hot spot' after heating (b) Shearographic 'fringe pattern'

Figure 5. 41: (a) IRISYS system; (b) Shearographic system

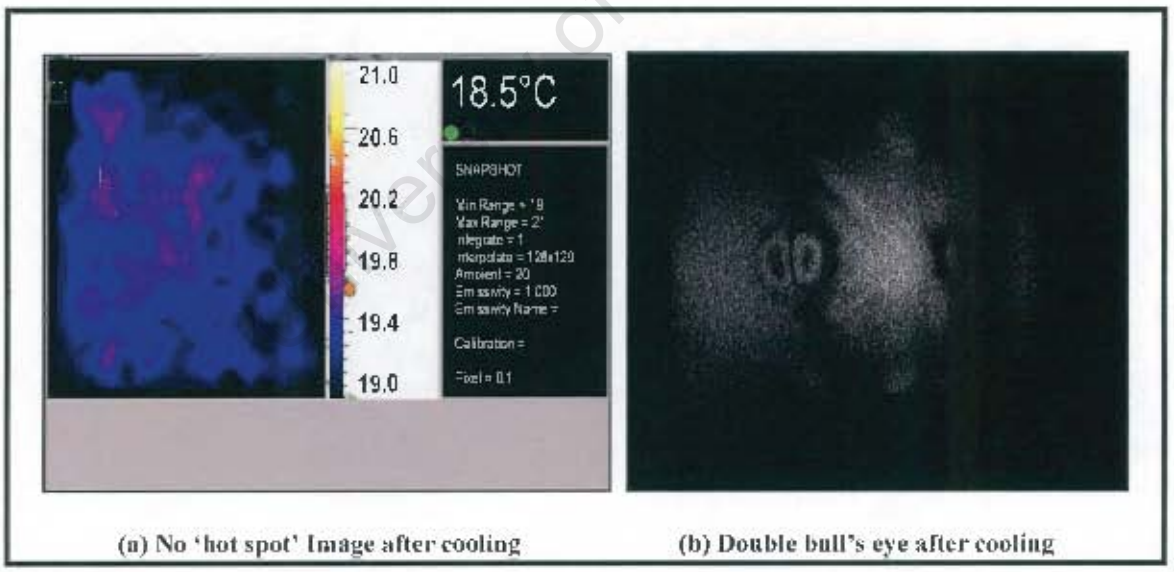

(a) No 'hot spot' Image after cooling (b) Double bull's eye after cooling

Figure 5. 42: (a) IRISYS system; (b) Shearographic system

Specimen: Helicopter blade with 9 defects, front heating for 10 sec

Typical results are shown in Figure 5.43 and Figure 5.44

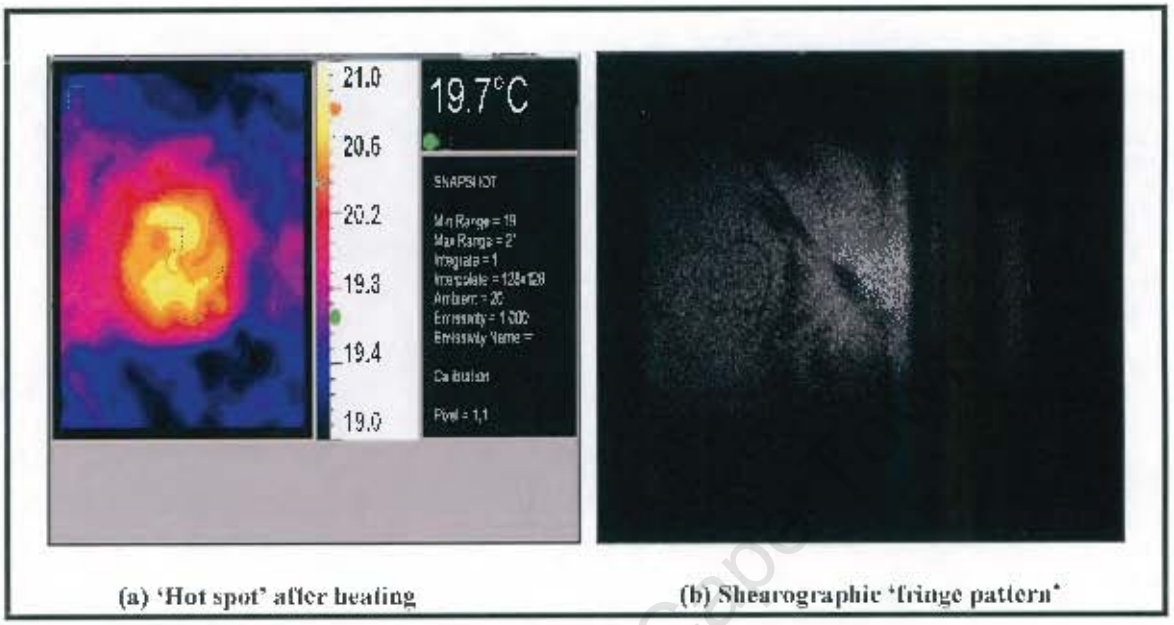

(a) 'Hot spot' after heating (b) Shearographic 'fringe pattern'

Figure 5.43: (a) IRISYS system; (b) Shearographic system

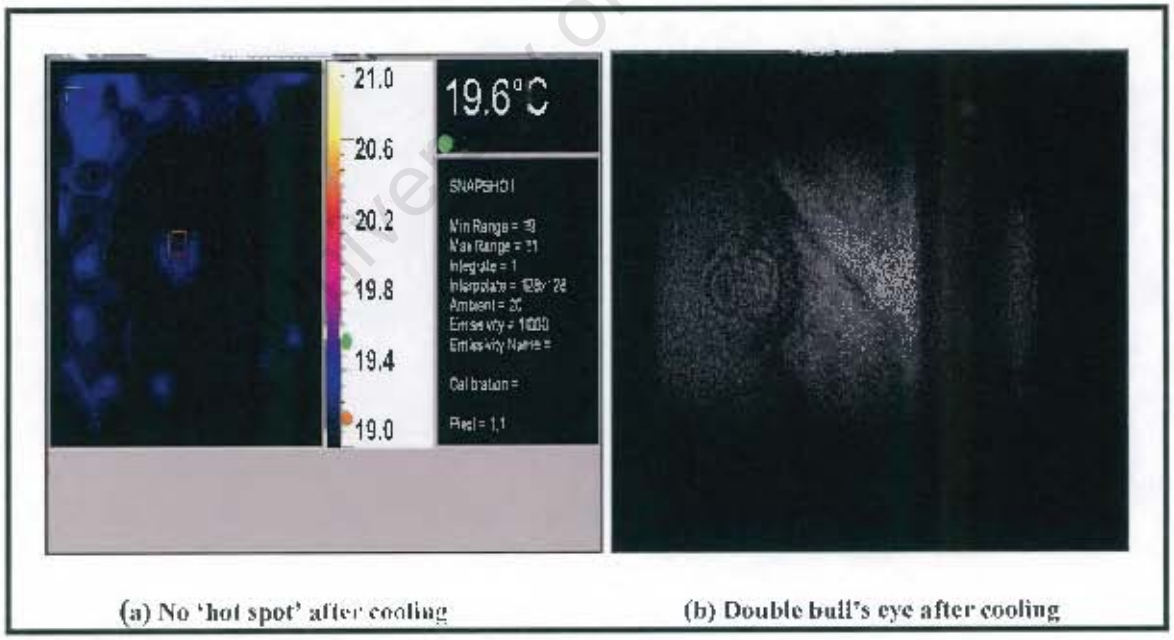

(a) No 'hot spot' after cooling (b) Double bull's eye after cooling

Figure 5. 44: (a) IRISYS system; (b) Shearographic system

Specimen: Helicopter blade with 9 defects, front heating for 15 sec

Typical results are shown in Figure 5.45 and Figure 5.46

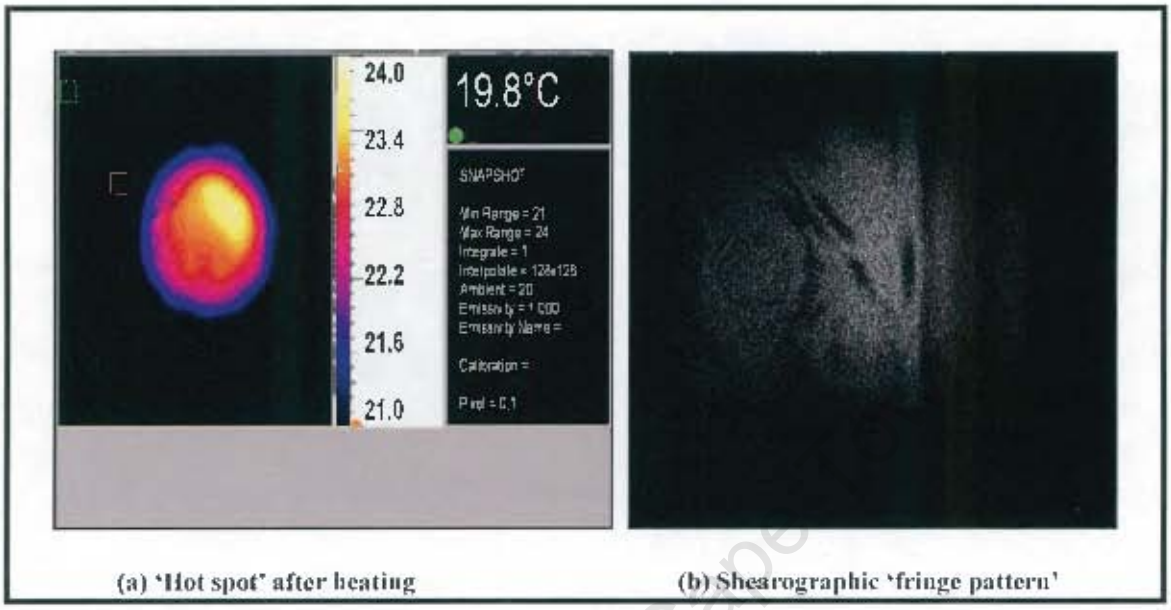

(a) 'Hot spot' after heating (b) Shearographic 'fringe pattern'

Figure 5.45: (a) IRISYS system; (b) Shearographic system

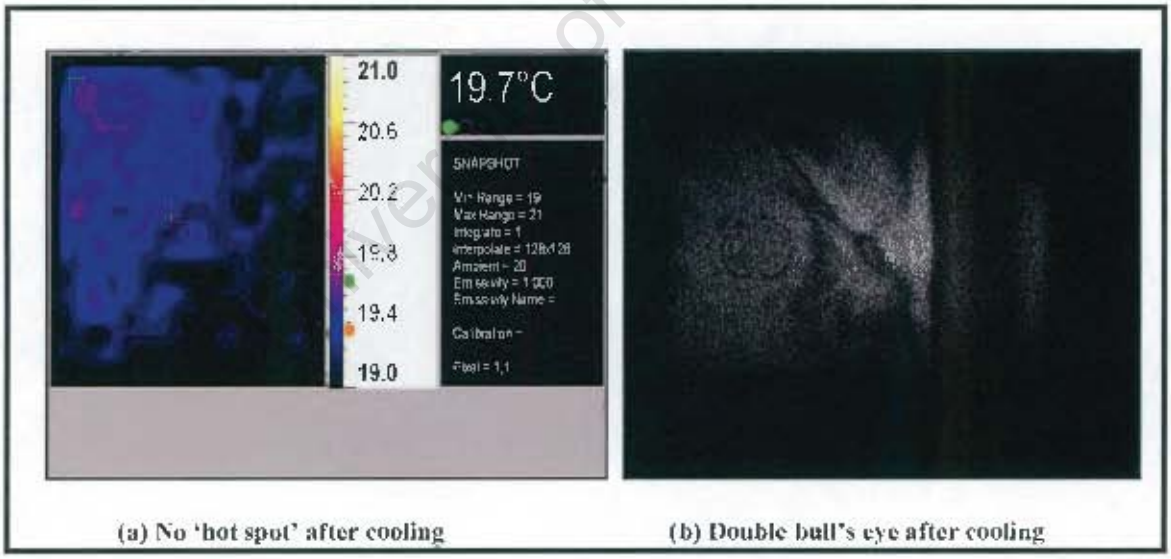

(a) No 'hot spot' after cooling (b) Double bull's eye after cooling

Figure 5.46: (a) IRISYS system; (b) Shearographic system

Specimen: Helicopter blade with 9 defects, far side heating for 5 sec

Typical results are shown in Figure 5.47 and Figure 5.48

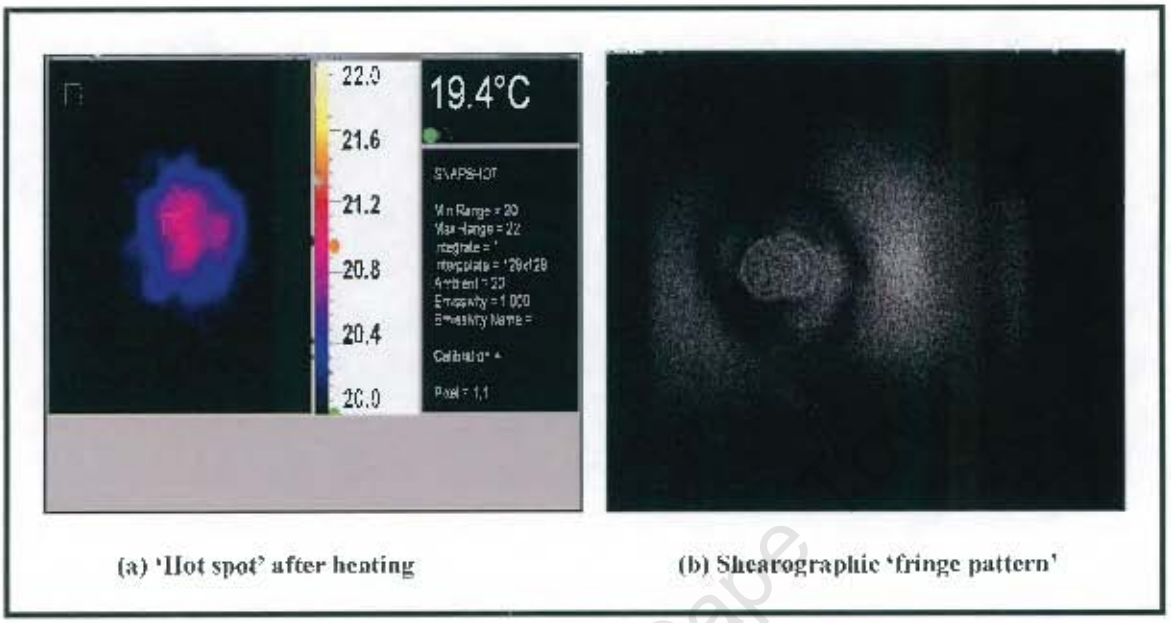

(a) 'Hot spot' after heating (b) Shearographic 'fringe pattern'

Figure 5. 47: (a) IRISYS system; (b) Shearographic system

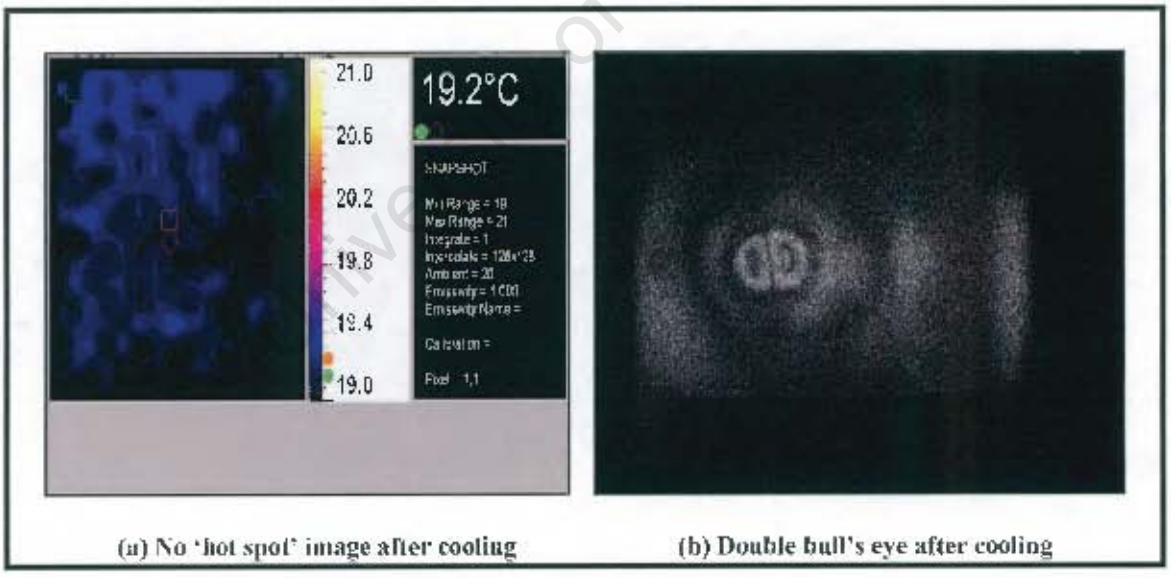

(a) No 'hot spot' image after cooling (b) Double bull's eye after cooling

Figure 5. 48: (a) IRISYS system; (b) Shearographic system

Specimen: Helicopter blade with 9 defects, far side heating for 10 sec

Typical results are shown in Figure 5.49 and Figure 5.50

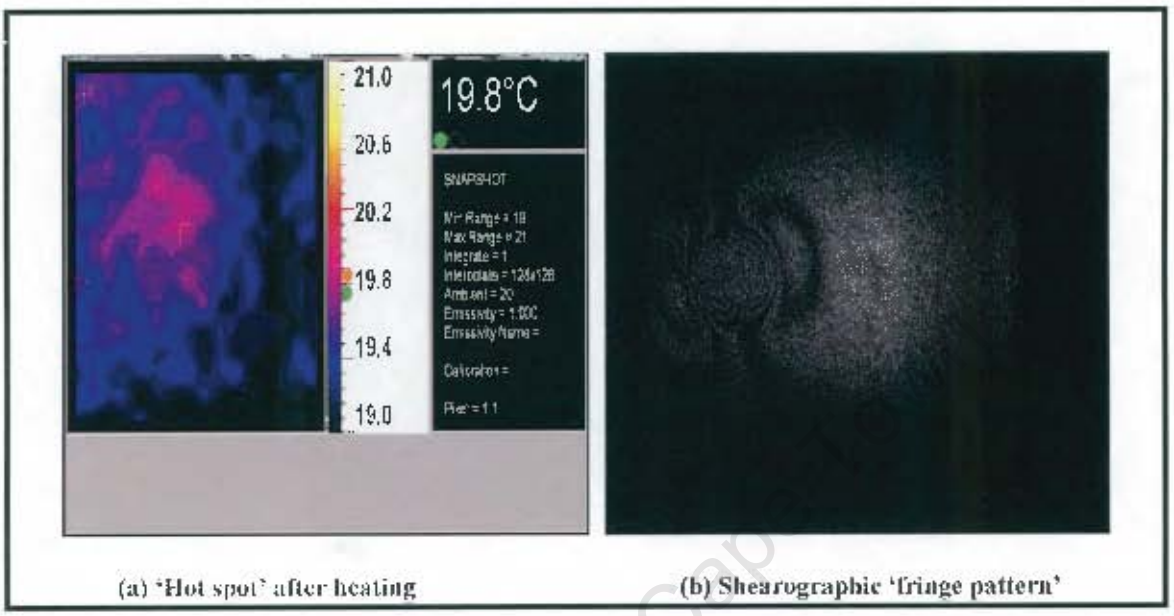

(a) 'Hot spot' after heating (b) Shearographic 'fringe pattern'

Figure 5.49 (a) IRISYS system; (b) Shearographic system

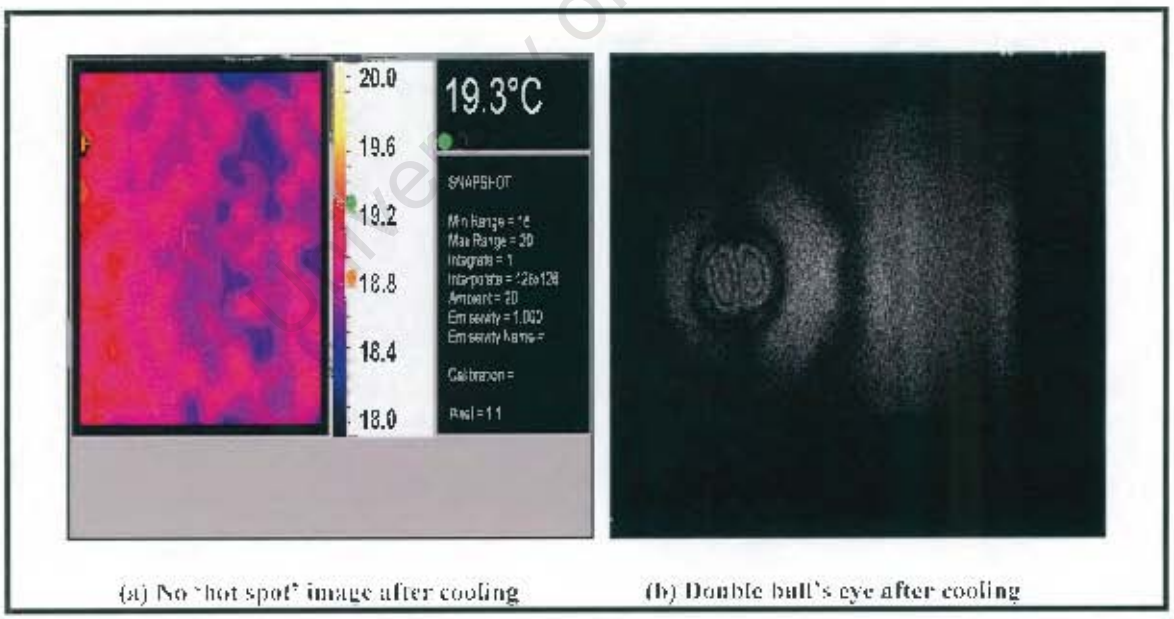

(a) No 'hot spot' image after cooling (b) Double bull's eye after cooling

Figure 5.50: (a) IRISYS system; (b) Shearographic system

Specimen: Helicopter blade with 9 defects, far side heating for 15 sec

Typical results are shown in Figure 5.51 and Figure 5.52

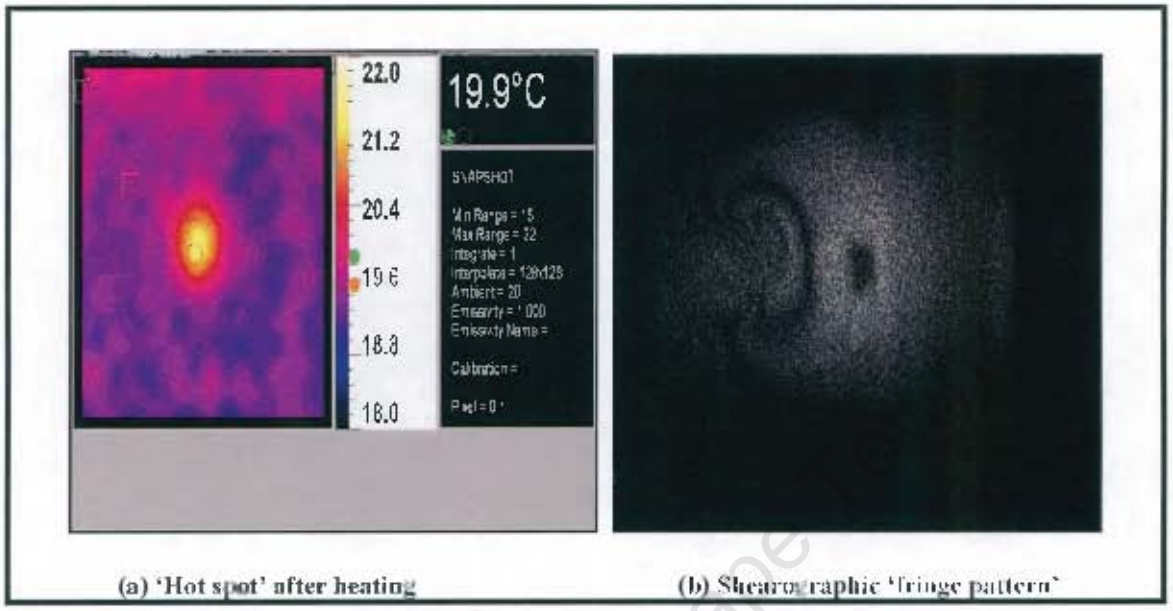

(a) 'Hot spot' after heating (b) Shearographic 'fringe pattern'

Figure 5.51: (a) IRISYS system; (b) Shearographic system

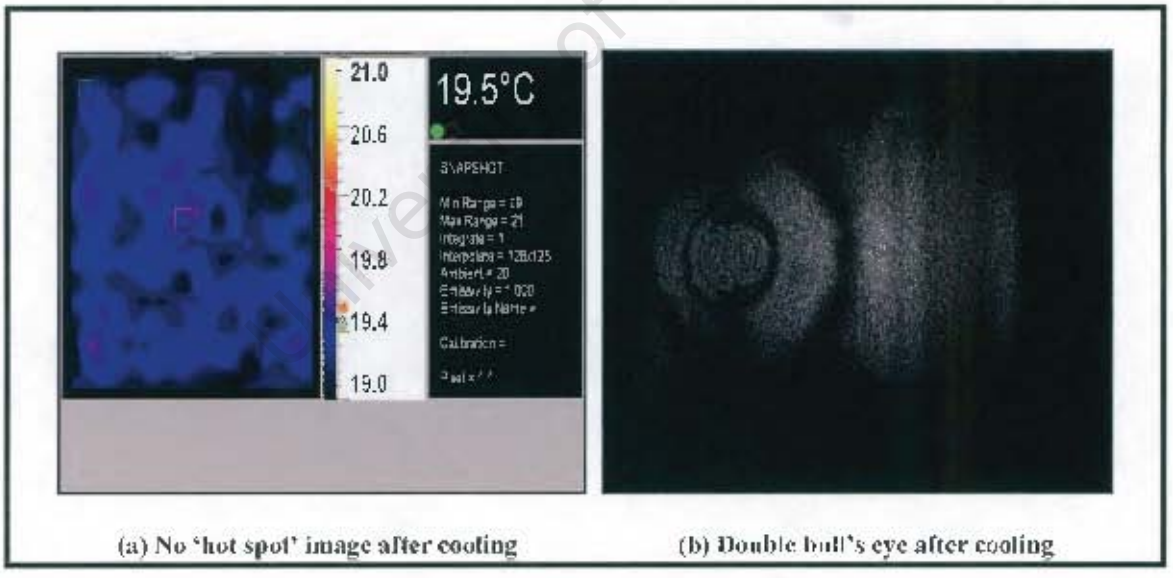

(a) No 'hot spot' image after cooling (b) Double bull's eye after cooling

Figure 5.52: (a) IRISYS system; (b) Shearographic system

5.1.3.6 Analysis of experiment no.5: IRT and Shearographic systems

The results presented in figures 5.17 to 5.52 above clearly demonstrates that both techniques, that is, IRT and shearography, detect and show readily the location of defects in the composite materials. Moreover, the IRT images were not only indicating the position of the defect or flaw, but produced data concerning the temperature of the region of the defect in relation to the cooler surrounding material.

The Shearographic system however, was exceptional in the display of the results. The system was not just as sensitive as IRT in responding to the radiant heat and readily displayed the image, but was also able to show the image much longer than the IRT system. This can be confirmed by the results presented above. In all the test results shown, Shearographic system showed the live fringes while IRT system had lost the 'hot spot'.

It should also be mentioned that, the amount of heating of the specimen has a direct effect on the number of fringes observed in the shearogram, and therefore flaws that are closer to the surface would reveal more fringes and those far away from the inspection surface would exhibit less fringes. The IRT system is characterized by a brighter colour at the 'hot spot' if more heat is applied. The distance at which the heat source is positioned, however, has also an influence on the outcome of the image produced.

Another interesting observation made is that both techniques were able to detect the BVID in the UAV specimen instantly. This certainly confirms the sensitivity of the techniques in defect detection of BVID in composite materials of this nature. The shearographic system nevertheless, was more sensitive in the detection of BVID in the UAV specimen. While IRT system had given up the 'hot spot', shearographic system showed the presence of the defect by a "kink' in the fringes (see circled spot). In all the images shown in figures 5.18, 5.20…5.28, there is a "kink" spot present which indicates the position of the defect.

Based on the observations made above, either of both techniques could be employed in the investigation of delaminations in composite materials and can complement one another for further evaluation. For example since shearography indicates surface strain in a given/chosen direction and the thermograms contain information regarding the surface temperature where the strain is exhibited, it could yield an evaluation of the surface thermal stresses. In this experiment, the Shearographic technique proved to be more sensitive than the IRT technique, that is, it continued to indicate the familiar double bull's eye long after the hot spot of the thermal imager had disappeared.

CONCLUSION

An introductory comparative study of IRT and Shearography in the detection of flaws in some aircraft composite materials has been introduced in this thesis. It is evident from the literature survey presented as well as the experimental technique performed in this work that; both techniques are capable of detecting flaws and with reasonable sensitivity. The techniques are easy to use and provide quick detection of flaws. It should however, be mentioned that the success of a NDT particularly in aircraft components depends largely on the proper choice of a testing technique. For a complex component such as a composite structure on the aircraft it will be imperative to verify the results from any NDT method used by the results of another measurement technique. The aim of optical techniques such as Digital shearography or IRT is not to merely replace conventional methods but to offer a complementary way, the potential to gather data rapidly and cost-effectively in a NDT inspection program.

The main focus of this work has been the feasibility of the quantification of defects in composite components using Digital shearography, an established imaging interface that allows real-time measurement of changes to a target surface. It offers fast detection of damage disbonds, porosity and delamination. It is thus considered as an essential tool for aircraft maintenance. It is easy to use and relies on a fairly simple interpretation of the fringe patterns. Shearogaphic results are not affected by surface conditions such as emissivity or paint, etc; therefore it requires no surface preparation.

Quantification of defects in composite materials with IRT should be possible through temperature indication above the flaw on the surface of the material.

It is not easy to define which optical method is the best because there is no "winning technique".

REFERENCES

[1]. "Non-Destructive Testing." (n.d.). http://www.hkpc.org/hkiemat/mastec03_notes/50.pdf.

[2]. Cecchini, A., 2005, "Damage Detection and Identification in Sandwich Composites using Neural Networks," MSc. Thesis, University of Puerto Rico.

[3]. Khan, A. U. Md., 1999, "Non-destructive Testing Applications in Commercial Aircraft Maintenance," *Proc. 7th European Conference on Non-destructive Testing,* Copenhagen, 26-29 June, Vol 4(6), http://www.ndt.net/article/ecndt98/aero/031/031.htm.

[4]. Venkatraman, B, Jayakumar T., Kalyanasundaram, P., and Raj, B., 2000, "NDE Methodologies for Examination of Tail Rotor Blades of Helicopters," *Proc.15th World Conference on Non-Destructive Testing,* Roma 15-21 October, http://www.ndt.net/article/wcndt00/toc/aero.htm

[5]. Riegert, G., Pfleiderer, K., Gerhard, H., Solodov, I., Busse, G., 2006, "Modern Methods of NDT for Inspection of Aerospace Structures," *Proc. 9th European Conference on Non-Destructive Testing,* Berlin, 25-29 September, *We.4.1.4,* http://www.ultrasonic.de/article/ecndt2006/doc/We.4.1.4.pdf

[6]. Nyman, T., 1999, "Fatigue and Residual Strength of Composite Aircraft Structures," LinkÖping, August, www.diva-portal.org/diva/getDocument?urn_nbn_se_kth_diva-2848-2_fulltext (1).pdf

[7] Shepard,S.M., 1997, "Introduction to Active Thermography for Non-Destructive Evaluation," *Anti-Corrosion Methods and Materials*, Volume 44, Number 4, pp 236-239, http://www.emeraldinsight.com/Insight/ViewContentServlet?Filename=Published/EmeraldFullTextArticle/Pdf/1280440402.pdf

[8]. Meola, C. and Carlomagno, G. M., 2004, "Recent Advances in the use of Infrared Thermography," *Measurement Science and Technology.* **15**, pp 27-58.

[9]. Wong, B.S., Tu, C.G., Bai,W., Tan, P.H., Low, B.S., and Tan,K.S.,(n.d) "Thermographic Evaluation of Defects in Composite Materials," http://www.ntu.edu.sg/mae/Research/programmes/Sensors/NDT/thermographybyBSWong.pdf

[10]. Gryzagoridis, J., and. Findeis, D., 2005, "Simultaneous Shearographic and Thermographic NDT of Aerospace Materials," www.ndt.uct.ac.za

[11]. Thomas, R.L., and Favro L.D, 1998, "Thermal Wave Imaging of Fluid Intrusion in Composites," http://www.eng.wayne.edu/legacy/imr/NASAFAADoD98.pdf

[12]. Guest Editorial, 2003, "Recent Developments in Digital Speckle Pattern Interferometry,"*Optics and Lasers in Engineering* 40, pp 439-445.

[13]. Hung, Y.Y., Ho H.P, 2005, "Shearography: An Optical measurement Technique and Application," *Materials Science and Engineering*, R 49 pp 61-87

[14]. Hung, Y.Y., 1989, "Shearography: A Novel and Practical Approach for Non-Destructive Testing," *Journal of non-destructive testing*, Vol. 8(2) pp 55-67

[15]. Findeis, D., and Gryzagoridis, J., 2004, "The Feasibility of Optical Interference-based NDE Methods to inspect Helicopter Rotor Blades," www.ndt.uct.ac.za

[16]. Krishnaswamy, S., 2000 "Optical Methods of Inspecting Composites (Holography and Shearography)," http://www.cqe.northwestern.edu/sk/SK-Papers/B4_optical_methods_composites_2000.pdf

[17]. Avdelidis, N.P., Almond, D.P, Marioli-Riga, Z.P., Dobbinson, B.C.,and Hawtin, 2005, "Pulsed Thermography: Philosophy qualitative and quantitative analysis on aircraft materials and applications," *Proc. 5th International*

workshop, Advances in Signal processing for NDE of materials, August Quebec city, Canada.

[18]. Clemente, C.I., 2005, "Quantitative Subsurface Defect Evaluation by Pulsed Phase Thermography," Depth Retrieval with phase, PhD Thesis, http://www.theses.ulaval.ca/2005/23016/23016.pdf

[19]. Maldague, X.(n.d), "Introduction to NDT by Active Infrared Thermography" http://www.gel.ulaval.ca/~maldagx/r_1221t.pdf

[20]. Avdelidis, N.P., Almond, D.P., Dobbinson, A., Hawtin, B.C., Ibarra-Castanedo C., and Maldague, X., 2004, "Aircraft Composites Assessment By Means of Transient Thermal NDT," Progress in Aerospace Sciences 40, pp 143-162.

[21]. Takeda,S., Aoki,Y., Ishikaw, T., Takeda, N., Kikukawa, H., 2007,"Structural Health Monitoring Of Composite Wing Structure During Durability Test," *Composite Structures* 79 pp 133-139.

[22]. Avdelidis N.P, Almond D.P, 2004, "Through Skin Imaging For Aircraft Assembly Using Pulsed Transient Thermography," *Journal of NDT&E International,* 37(5), pp. 353-359

[23]. Xiaoyan Han, L.D. Favro and Thomas R.L, 1998, "Thermal Wave NDI of Disbonds and Corrosion in Aircraft", http://www.eng.wayne.edu/legacy/imr/NASAFAADoD98.pdf

[24]. Capriotti, R., Dati E., Silvester, P., Trivisonno, G., 2000, "NDT Techniques for the Evaluation of Impact Damage On Aeronautical Structures," *Proc.15th World Conference on Non-Destructive Testing,* Roma 15-21 October, http://www.ndt.net/article/wcndt00/toc/aero.htm

[25]. Ibarra-Castanedo C.,Galmiche., Darabi, A., Pilla, M., Klein., Ziadi A., Vallerand S, Pelletier, J.F., Maldague, X., 2003,"Thermographic Nondestructive Evaluation,": *Overview of recent progress*. Quebec, Canada, http://vision.gel.ulaval.ca/~ibarrac/publications/Thermosense2003.pdf

[26]. Kaiser, H., Karbhari, V.M., 2002, "Quality and Monitoring of Structural Rehabilitation Measures," Part 2: Review and Assessment of Non-destructive Testing (NDT) Techniques, www.oregon.gov

[27]. Yang, L., Steinchen, W., Kupfer, G., Mäckel, P., and Vössin, 1998,"Vibration Analysis By Means of Digital Shearography," *Optics and Lasers in Engineering* 30, pp 199-212.

[28]. Laser Technology (UK) LTD (n.d), "An Advanced Nondestructive Testing Method that Throws a Whole new light on Inspection of Composite Material," www.laser.ndt.co.uk/laser-shearography

[29]. Steinchen, W., Kupfer, G., Mäckel, P., Vössing, F., 1999, "Determination of Strain Distribution by means of Digital Shearography," *Measurement* 26 pp 79-90.

[30] Kim, H. J., Park, Y.K., Park, J.H., and Woo, C.G., (n.d), "Development of the Integrated Measuring System of Strain Distribution and Defect using ESPI and Shearography," http://www.samsung.com/AboutSAMSUNG/ELECTRONICSGLOBAL/SocialCommitment/HumantechThesis/WinningPapers/downloads/work10/b3.pdf

[31]. Myles J. R., 1997, "Electronic Speckle Pattern Interferometry (ESPI) NDE of Cracks in Pressure Vessels with FEA Modeling," MSc, University of Cape Town

[32]. Huang, J.R, Ford, H.D, and Tatam, R.P., 1997, "Slope Measurement by two Wavelength Electronic Shearography,"*Optics and Lasers in Engineering* 27(3), pp 321- 333.

[33]. Zhang, J., 2006, "Studies on Digital Shearography for Testing of Aircraft Composite and Honeycomb Structures," *Proc. 9th European Conference on Non-Destructive Testing,*, Berlin, 25-29 September, Vol11 (11).

[34]. Yang, L.X., and Hung, Y.Y., 2004 "Digital Shearography for Nondestructive Evaluation and Application in Automotive and Aerospace Industries", http://www.ndt.net/article/wcndt2004/pdf/optical_techniques/534_yang.pdf

[35]. Hung, Y.Y., Luo, W.D., Lin, L., Shang, H.M., 2000, "Evaluating the Soundness of Bonding using Shearography," *Composite Structures* 50 pp 353-362

[36]. Findeis, D., and Gryzagoridis, J., 2004, "Inspecting Glassfibre Reinforced Plastic Piping using Portable ESPI and Shearography," www.ndt.uct.ac.za

[37]. Jones, R. and Wykes, C., 1989. *Holographic and Speckle Interferometry*, 2 nd ed., Cambridge University Press, Cambridge.

[38]. Hung, Y.Y., 1997, "Digital shearography Versus TV- holography for Nondestructive Evaluation," *Optics and Lasers in Engineering* volume 26, pp 421-436.

[39]. Kyung-Suk, K., Ki-Soo, K., Young-June, K., Seong-Kyun, C., 2003, "Analysis of an Internal Crack of Pressure Pipeline using ESPI and Shearography," *Optics &Laser Technology* 35, pp 639-643.

[40]. Svanbro, A., 2004, "Speckle Interferometry and Correlation Applied to Large Displacement Fields," Thesis. http://epubl.ltu.se/1402-1544/2004/05/index-en.html

[41]. Hung, Y.Y., 1999, "Applications of Digital Shearography for Testing of Composite Structures," *Composites:* Part B 30, pp 765-773.

[42]. Hung, Y.Y., and Wang J.Q., 1996, "Dual-beam Phase Shift Shearography for Measurement of In-plane Strains," *Optics and lasers in Engineering,* 24, pp 403-413.

[43]. Findeis, D., Gryzagoridis, J., Matlali, M., 2004, "Phase Stepping Shearography and Electronic Speckle Pattern Interferometry," www.uct.ac.za.

[44]. Hung, M.Y.Y., Long, K.W., and Wang J.Q., 1997, "Measurement of Residual Stress by Phase Shift Shearography", *Optics and Lasers in Engineering* 27, pp 61-73.

[45]. Angel, L., Tebaldi, M., and Henao, R., 1998, "Phased-Stepped Technique with an Electro-Optic Crystal in Digital Speckle Pattern Interferometry," *Optics and Communications,* 149, pp 235-238.

[46]. Maas, AD AM., Somers, PM., 1997, "Two-Dimensional Convolution Applied to Phase-Stepped Shearography", *Optics and Lasers* 26, pp 351-360.

[47]. Andhee, A., Gryzagoridis, J., and Findeis, D., 2005, "Comparison of Normal and Phase Stepping Shearographic NDE", www.uct.ac.za.

[48]. Rastogi, P.K., 2001, *Digital Speckle Pattern Interferometry and Related Techniques,* John Wiley and Sons, LTD.

[49]. Hubert, A., Aebischer, Waldner, S., 1999, "A Simple and Effective Method for Filtering Speckle-Interferometric Phase fringe Patterns," *Optics Communications* 162, pp 205-210.

[50]. Mayer, T., 2002, "Shearography Testing on Aerospace CFRP components," *Paper presented at the 8th European Conference on Non-Destructive Testing,* Barcelona, June, Vol. 8(2).

[51]. Findeis, D., and Gryzagoridis, J., 2004, "Portable Shearography and portable Electronic Speckle Pattern Interferometry," A presentation of their capabilities, www.uct.ac.za.

[52]. Pezzoni, R., 2000, "Laser-Shearography for Nondestructive Testing of Large Area Composite Helicopter Structures," *Proc.15th World Conference on Non-Destructive Testing,* Roma, 15-21 October.

[53]. Kalms, M., and Juepter, W., 2005, "Mobile shearography," NDT.net April Vol.10 No.4.
http://www.ndt.net/article/icem2004/papers/108/108.htm

[54]. Hung, Y.Y., 1996, "Shearography for Non-destructive Evaluation of Composite Structures", *Optics and Lasers in Engineering* 24, pp 161-182.

[55]. Toh, S., and Chau Fook-Siong., 1999, "Using shearography to find Flaws," http://www.memagazine.org/backissues/membersonly/february99/features/shearography/shearography.html.

[56]. Honlet, M., Ettemeyer, A., and Walz T., 1998, "Automated and Non-Destructive Inspection of Composite Helicopter Rotor Blades using Advanced Shearography," *NDT.net*-September Vol. 3 No. 9.

[57]. Sim, C.W., Chau F.S., Toh S.L., 1995, "Vibration Analysis and Non-Destructive Testing with Real-time Shearography", *Optics and Laser Technology,* Vol. 27 No. 1, pp 45-49.

[58]. Andersson, J., and Van B., 2000, "NDI on Bonded Sandwich Structures with Foam Cores and Stiff Skins- Shearography the Answer?" *Proc.15th World Conference on Non-Destructive Testing,* Roma, 15-21 October.

[59]. Capt. K. Dragon, Lt.Col. S. Klimaszewski, Maj. A. Leski, and M. Kurdelski, (n.d), "In-Service NDI of Aging Helicopters Main Rotor Blades used in Polish Armed Forces", 9th Joint FAA/DoD/NASA, Aging Aircraft Conference.

[60]. Sala, G., 2000, "Composite Degradation Due to Fluid Absorption," *Composites:* Part B 31, pp 357-373.

[61]. Ibekwe, S., Mensah, P.F., Li, G., Pang, S.S., and Michael, A.S., 2007, "Impact and Post Impact Response of Laminated Beams at Low Temperatures," *Composite Structures*, pp 12-17.

[62]. Galea, S.C., Shah, L.P., and Sanderson S., 1995, "The Effect of Multiple Damage in Composite Structures," A Theoretical Investigation, *Composite Structures* 32, pp 383-390.

[63]. Ganapathy, S., Tripathy, B., and Rao, K. P., 1995, "Damage and its Growth in Laminated Composite Circular /Rectangular Plates undergoing Large Deformations," *Composite Structures* 32, pp 367-373.

[64]. Kim, J.K., 2000, *Impact Behaviour of Fibre-Reinforced Composite Materials and Structures: Recent Developments in Impact Damage Assessment of Fibre Composites*, S.R Reid and G. Zhou,"eds", Woodhead Publishing Limited, Cambridge, PP 33.

[65]. Clark, G., 2005, "Failure in Military Aircraft," *Engineering Failure Analysis* 12, pp 755-771.

[66]. Hancox, N.L., 2000, *Impact Behaviour of Fiber Reinforced Composite materials and Structures*: An overview of the impact behaviour of fibre-reinforced composites, S.R Reid and G.zhou, "eds," Woodhead Publishing Limited, Cambridge, pp1-32.

[67]. Richardson, M.O.W., and Wisheart, M.J., 1996, "Review of low-velocity Impact Properties of Composite Materials," *Composites Part A* 27A, pp 1123-1131.

[68]. Olsson, R., 2000, "Mass Criterion for Wave Controlled Impact Response of Composite Plates," *Composites: Part A* 31, pp 879-887,

[69]. Abrate, S. 1998, *Impact on composite Structures,* Cambridge University Press, Cambridge, UK, Chap. 4.

[70]. Kim, J.K., and Yu, T.X., 1998, "Impact Response and Dynamic Failure of Composites and Laminate Materials," Part 1: Impact Damage and Ballistic Impact, *Key Engineering Materials* Volumes 141-143, Part 1: pp 128.

[71]. Olsson, R., 2001, "Analytical Prediction of large Mass Impact Damage in Composite Laminates," *Composites: Part A* 32, 1207-1215.

[72]. Valentino,M.,Bonavolonta, Peluso, G., and Pepe, G.P., 2006, "Real-time Monitoring of Fatigue Damage in Carbon Fiber Reinforced Polymers for Aeronautical Applications using HTS Squid Magnetometer," *Proc. 7 th European Conference on Applied Superconductivity: Journal of Physics, Conference Series 43, pp 1231-1234.*

[73]. Islam, A.S., and Craig, K.C., 1994, "Damage Detection in Composite Structures using Piezoelectric Materials," *Smart Material Structure.* 3, pp 318-328.

[74]. Chian-Fong Yein and Thomas Cassin, "Progressive Failure Analysis of Thin Walled Composites tubes under low Energy Impact" (n.d). http://www.materials-sciences.com/papers/impact.pdf.

[75]. Morais, W.A.de., Monteiro, S.N., and d'Almeida, J.R.M., 2005, "Effect of the Laminate Thickness on the Composite Strength to Repeated low energy Impact. *Composite Structures,* 70, pp 223-228.

[76]. "IRISYS IRI-1011 Imager," 2003, *article,* published on *Engineering talk,* October.
http://www.entherm.com/Irisys/IRISYS%20Thermal%20Imager.htm

[77]. "Thermal imaging breaks budget barrier,"2003, article published on *Engineering talk*, October,
http://www.engineeringtalk.com/news/iri/iri101.html

[78]. "IRISYS Universal Thermal Imager", 2007, Type IRI 1011 *User Manual* IPU 40060 Issue 7, pp 1-28,
http://www.entherm.com/Irisys/IRISYS%20Thermal%20Imager.htm

APPENDICES

Appendix A

A1 Glossary of terms

A1.1 JAS 39 Gripen

The Saab JAS 39 "Gripen" is a fighter aircraft manufactured by the Swedish aerospace company Saab. The designation 'JAS' stands for Jackt (Air-to-Air), Attack (air-to-surface), and Spanning (Reconnaissance), indicating that the Gripen is a multirole aircraft that can fulfill different types of military missions.

A1.2 Canard (French for duck)

In aeronautics, canard is an airframe configuration of fixed-wing aircraft in which the tail plane is ahead of the main lifting surfaces, rather than behind them as in conventional aircraft, or when there is an additional small set of wings in front of the main lifting surface.

A1.3 C-130 Hercules

The C-130 Hercules is a four engine turboprop cargo aircraft and the main tactical air lifter for many military forces worldwide. It is manufactured by Lockheed Company.

A1.4 Boeing 747(or B747)

The B 747, four engine aircraft, commonly nicknamed the "Jumbo Jet," is a long-haul, wide body commercial airliner manufactured by Boeing. Known for its impressive size, it is among the world's most recognizable aircraft and can accommodate a range of 416 to 524 passengers depending on the class of layout used. The B747-400, the latest version in service, flies at high-subsonic speeds of mach 0.85(567mph or 913 km /h),

A1.5 Boeing 787 (B787)

The Boeing 787 Dream liner is an American mid-sized, wide body, twin engine Jet airliner currently in production by Boeing's Commercial Airplanes division and scheduled to enter service in May 2008. It will carry 210 and 310 passengers depending on variant and seating configuration. Boeing has stated that it will be more fuel-efficient

than earlier Boeing airliners. It will also be the first major airliner to use composite material for most of its construction. Of course there are other aircrafts already using composite materials, but for B787, composite material will constitute about 50 %.

A1.6 Airbus A380

The Airbus A380 is a double-deck four engine airliner manufactured by EADS (Airbus S.A.S). It is the largest passenger airliner in the world. It provides seating for 525 people in standard three-class configuration or up to 853 people in full economy class configuration. The A380-800, the passenger model, is the largest passenger airliner in the world, superseding the Boeing 747. The A380-800F, the freighter model, is designed as one of the largest freight aircraft, with a listed payload capacity exceeded only by the "Antonov An-225". The A380-800 has a design range of 15,200 km, sufficient to fly from New York to Hong Kong non stop and the cruising speed of mach 0.85 (about 900km/h at cruise altitude.)

A1.7 F-22 Advanced tactical fighter

The F-22 is a fifth generation fighter aircraft which uses fourth generation Stealth technology.

A1.8 C-141

The C-141 star lifter was a military strategic air lifter in service with the United States Air force (USAF).

A1.9 F-15

The F-15, is an all weather strike fighter aircraft.

A1.10 Cowling

A removable cover or housing placed over or around an aircraft component or section, especially an engine.

A1.11 Flaps, leading edge

Hinged section of the underside of the leading edge, which, when extended, reduces air flow separation over the top of the wing. Leading edge flaps are hinged at the leading edge of the airfoil.

A1.12 Stabilizer

This is a fixed horizontal tail surface that serves to maintain stability around the lateral axis of an aircraft.

A1.13 Vertical fin

This is sometimes referred to as vertical stabilizer or fin. It is fixed to provide directional stability. The trailing edge is hinged to form the rudder.

A1.14 Rudder

The rudder is the flight-control surface that controls aircraft movement about its vertical axis. It is constructed very much like other flight-control surfaces, with spars, ribs, and skin, and is mounted on the vertical fin

A1.15 Spoilers

Spoilers are also called lift dampers, and these are control surfaces used to reduce, or "spoil," the lift on a wing. Spoilers are located on the upper surface of the wings.